Numerical Investigation of the Effects of Continuum Breakdown on Hypersonic Vehicle Surface Properties

by

Timothy Dean Holman

A dissertation submitted in partial fulfillment
of the requirements for the degree of
Doctor of Philosophy
(Aerospace Engineering)
in The University of Michigan
2010

Doctoral Committee:

Professor Iain D. Boyd, Chairperson
Professor Kenneth G. Powell
Associate Professor Hong G. Im
Michael J. Wright, NASA ARC

For my father,
who inspired my love of aerospace.

ACKNOWLEDGEMENTS

The work presented in this document represents many years of hard work and study. This work would not have been possible without the support of many people throughout my life.

First, I would like to thank my advisor, Dr. Iain Boyd, for providing support and guidance during my time as a graduate student at the University of Michigan. I first meet Dr. Boyd as an undergraduate student in a Hypersonic Aerothermodynamics course at the University of Michigan. I later decided that I wanted to stay in the field of hypersonics and study with Dr. Boyd. In short, thanks for providing all of the academic and technical support over the past five years, I greatly appreciated it.

I would like to acknowledge and thank the members of my dissertation committee for their willingness to serve and for reviewing and providing helpful feedback on my research, which helped improve the final version. I would also like to thank the members of my dissertation committee for attending my pre-defense presentation and providing valuable feedback which helped guide my research over the past year.

I would like to thank Dr. David Hash and Dr. Michael Wright for giving me the opportunity to work at NASA Ames Research Center. I would also like to thank them for talking the GSRP people into letting me leave Ames for a summer, who would have thought that would be such a big ordeal. I would also like to thank Dr. Wood for giving me the opportunity to work on the Space Shuttle Orbiter at NASA Largely Research Center. It was a great honor to work on one of the great

engineering feats on this era. Also, I would like to thank Dr. Camberos for providing the opportunity to work at Air Force Research Lab at Wright-Patterson Air Force base. Working at these facilities has provided valuable help on my research with the added benefit of getting to work with some of the top individuals in the my field.

I would like to acknowledge and thank my colleagues in the Nonequilibrium Gas and Plasma Dynamics Laboratory. It was great to be a part of a lab were there was always someone willing and able to help out when a problem was encountered. The members of this lab also provided much needed distractions from the grind of graduate research; from the afternoon trips to Pierpont to fantastic christmas parties. Thanks for the great memories.

There are a few people from NGPDL that I would like to give a special thanks to. Thanks to Dr. Jon Burt for provided much needed help understanding DSMC and MONACO. Thanks to Dr. Andrew Lofthouse for the help in getting me started with my research and running LeMANS. Last, but not least, thanks to Tim "that other Tim" Deschenes for answering all of my questions over the last few years.

Finally, I would like to thank my parents, if it were not for your constant support I would never have made it this far. Thanks for everything.

TABLE OF CONTENTS

LIST OF FIGURES

LIST OF TABLES

LIST OF NOMENCLATURE

Constants

k_{BOLTZ}	Boltzmann Constant [1.38×10^{-23} J/K]
N_A	Avogadro's Number [6.022×10^{26}]
$\mathbf{R}$	Universal Gas Constant [8.314 J/K·mol]

Acronyms

CFD	Computational Fluid Dynamics
DSMC	Direct Simulation Monte Carlo
VHS	Variable Hard Sphere
VFD	Vibrationally Favored Dissociation

Latin Symbols

a	Modified Arrhenius Rate Constant
$\bar{c}$	Mean Speed [m/s]
B	Garcia's Breakdown Parameter
$\mathbf{c}$	Particle Velocity Vector $\mathbf{c}(c_x, c_y, c_z)$ [m/s]
$\mathbf{C}$	Thermal Velocity Vector $\mathbf{C}(C_x, C_y, C_z)$ [m/s]
$c_{v,p}$	Specific Heat [J/kg·K]
C_p	Pressure Coefficient
C_τ	Shear Coefficient
C_q	Heat Flux Coefficient
D	Integrated Drag [N], Diffusion Coefficient, Dissociation Potential [J/kg]
d	Molecular Diameter [m]
E	Energy per Unit Volume [J/m^3], x-direction Flux Vector
e	Specific Energy per Unit Volume [J/m$^3 \cdot$ kg]
F	External Force [N], y-direction Flux Vector
f	Velocity Distribution Function f ($\mathbf{r}$, $\mathbf{c}$, t)
f_B	Maxwellian (or equilibrium) Velocity Distribution Function
f_G	Anisotropic Gaussian Distribution Function
G	z-direction Flux Vector
$\mathbf{g}$	Relative Velocity Vector [m/s]
h	Enthalpy [J/kg]
$\mathbf{J}$	Diffusion Flux Vector $\mathbf{J}(J_x, J_y, J_z)$ [kg/$m^2 \cdot s^2$]

k	Reaction Rate
K_e	Equilibrium Constant
Kn_∞	Global Knudsen Number
Kn	Knudsen Number
Kn_{GLL}	Gradient Length Local Knudsen Number
L	Characteristic Length [m]
Le	Lewis Number
m	Mass [kg]
m^*	Reduced Mass [kg]
M	Mach Number, Molecular Mass [kg/kmol]
N	Number of Particles
n	Number Density [m^{-3}]
$\mathbf{V}$	Bulk (Average) Velocity Vector $\mathbf{V}$(u,v,w) [m/s]
Q	Conserved Variable Vector
$\mathbf{q}$	Heat Transfer Rate $\mathbf{q}(q_x, q_y, q_z)$ [W/m^2]
p	Pressure [Pa]
P	Average Probability, Bird's Breakdown Parameter
$\mathbf{r}$	Position Vector $\mathbf{r}$(x,y,z) [m]
R_{gas}	Specific Gas Constant [J/K·kg]
S	Source Term Vector
T	Temperature [K]
X	Mole Fraction
Y	Mass Fraction
Z	Collision Number

Greek Symbols

α	Fraction of Dissociation Potential
$\Delta^{(i)}$	Gupta-Yos Coefficients
ε	Activation Energy [J]
λ	Mean Free Path [m]
μ	Viscosity [Pa·s]
κ	Thermal Conductivity [W/m·K]
ν	Mean Collision Rate [1/s], BGK Characteristic Relaxation Time [s], Chapman-Enskog Term
η	Modified Arrhenius Temperature Power
Γ	Chapman-Enskog Distribution
γ	Ratio of Specific Heats
ρ	Density [kg/m^3]
Φ	Tiwari's Breakdown Parameter
ϕ	Instantaneous Probability, VFD Constant, Surface Angle [Deg]
σ	Collision Cross Section [m^2], Accommodation Coefficient
$\sigma d\Omega$	Differential Cross Section
$\sigma^2\Omega^{(1,1)}$	Diffusion Collision Integral [m^2]

$\sigma^2 \Omega^{(2,2)}$	Viscosity Collision Integral $[m^2]$
τ	Shear Stress Tensor[Pa], Relaxation Time [s]
τ_c	Mean Collision Time [s]
ω	VHS Temperature Exponent
$\dot{\omega}$	Navier-Stokes Source Terms
ξ	Chapman-Enskog Parameter
ζ	Internal Degrees of Freedom

Subscripts

b	Backward
cont	Continuum
f	Forward
LT	Landau-Teller
p	Park
part	Particle
r	Rotation
ref	Reference Value
s	Slip Value
tr	Translation-Rotation
v	Vibration, Viscous
ve	Vibration-Electron-Electronic
w	Wall Value
∞	Free Stream
0	Stagnation Point

Superscripts

$\wedge$	Normalized

CHAPTER I

Introduction

1.1 Motivation

With a renewed desire to send humans back to the Moon and beyond, there is a need for accurate studies of the flow behavior over hypersonic vehicles to precisely determine how they will perform when entering an atmosphere. The imminent ending of the Space Shuttle program has led to a greater interest in the design of the future hypersonic vehicles for reentering Earth's atmosphere. There has also been a growing interest in the entry of other planetary atmospheres, such as Mars.

To be able to design a hypersonic vehicle, it is important to understand how various physical phenomena affect the surface conditions such as heat flux, pressure and shear stress. These surface conditions determine the aerodynamic and thermodynamic performance of a reentry vehicle. Hence, these properties are important to the design of the thermal protection system of a reentry vehicle. The thermal protection system shields the vehicle from the extreme conditions encountered during hypersonic reentry.

A hypersonic vehicle crosses many regimes from rarefied to continuum due to the change in density with altitude during the course of its trajectory through a planet's atmosphere. It is difficult and expensive to reproduce these varied flow conditions

in ground based experiments and flight tests, so there is a need for computational models that can be utilized for design and development of hypersonic vehicles. Computationally simulating the environment experienced during a hypersonic flight is an important step in the design process of a hypersonic vehicle. Experimental tests are still required, but computational work can limit their need in the design process making it cheaper and more efficient. Hence, there is a greater need for the development of accurate computational methods for the design of hypersonic vehicles.

1.2 Hypersonic Reentry Flows

A hypersonic vehicle that is entering an atmosphere will go through many different flow regimes due to the change in atmospheric density with altitude. The flow can be characterized by the Knudsen number as given in Eq. (1.1).

$$Kn = \frac{\lambda}{L} \tag{1.1}$$

where λ is the mean free path and L is a characteristic length scale. A hypersonic vehicle will travel through several regimes; starting with the free molecular regime when entering an atmosphere, where there are so few intermolecular collisions that they are ignored. As the vehicle descends, it will enter the rarefied gas regime, where intermolecular collisions are present but the gas is still very diffuse. Finally, the flow will enter the continuum regime, where the gas is now dense enough to be thought of as a continuum rather than in a particle view. In between the rarefied gas and continuum flow regimes is the transitional regime.

These regimes are typically characterized by Knudsen number, as shown in Fig. 1.1. This figure gives the four regimes and indicates the numerical methods that are accurate for each regime. The Boltzmann equation is valid for all flow regimes, from
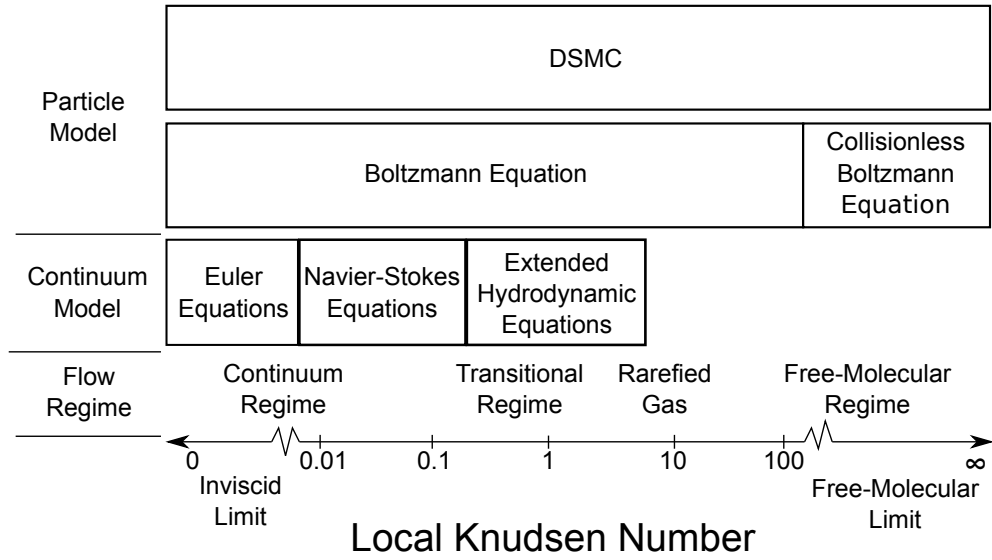
Figure 1.1: The Knudsen number limits for each method

continuum to free molecular flow. The Navier-Stokes equations are valid in the continuum regime, below the generally accepted, but often argued, limit of a Knudsen number of 0.01. The extended hydrodynamic equations can be utilized into the transitional regime, but these methods have not been developed as much and it is not clear how far into the transitional regime they can be utilized. The DSMC method, which has been shown to converge to solutions of the Boltzmann equation[1], can also be utilized over all flow regimes.

At lower altitudes where the density is high and the Knudsen number is low, flows should be simulated using traditional computational fluid dynamics (CFD) techniques by numerically solving the Navier-Stokes equations. However, when the Knudsen number becomes larger, the continuum assumption in the Navier-Stokes equations starts to breakdown. This is due to the fact that these equations are derived from kinetic theory based on the assumption of small perturbations from an equilibrium velocity distribution function[2]; therefore CFD only works in near equilibrium flows.

At low Knudsen numbers, the no-slip boundary conditions hold. At higher Knudsen numbers, there are insufficient collisions near the wall and the flow is not able to equilibrate with the wall, hence the no-slip condition is invalidated. The use of slip boundary conditions in the CFD method can extend the validity of this approach further into the transitional flow regime.

At higher altitudes, in the rarefied flow regime, only a non-continuum technique can be used, such as the direct simulation Monte Carlo (DSMC) method[3]. DSMC is a Monte Carlo particle method for simulating nonequilibrium gas flows. DSMC is required for accurate flow analysis of hypersonic rarefied flows where the continuum flow equations are invalid, and can be utilized in any dilute gas flow. Unfortunately, DSMC is about an order of magnitude more expensive than traditional CFD methods and becomes prohibitively expensive at low Knudsen numbers. Note that even if the global flow behaves as a continuum, there may still be parts of the flow that locally act as a rarefied flow, if the local length scale is very small or the local density is low. For example, a hypersonic blunt body can create a locally rarefied flow in the shock, the boundary layer and the wake of the body. As a result, neither CFD nor DSMC can provide a complete computational model across all regimes of a hypersonic vehicle.

One solution to this problem of continuum breakdown, is a hybrid code that utilizes CFD and DSMC methods to accurately and efficiently simulate a hypersonic flow. This hybrid code can solve the Navier-Stokes equations when the flow is considered to be a continuum, but can switch to a DSMC method when the flow is considered rarefied such as in a shock wave[4]. This process involves some way of finding when the physics of the simulation provided by the CFD method deviates from physical results; this is performed with the continuum breakdown parameter.

1.3   Review of Related Work

Since DSMC was introduced, there have been several studies comparing CFD techniques with the DSMC method. One of the earliest studies conducted compared DSMC and the viscous shock layer (VSL) methods for typical hypersonic reentry conditions found near the nose region of the Space Shuttle Orbiter[5]. The viscous shock layer method included velocity slip and temperature jump boundary conditions. These simulations were performed in a flow of 5-species reacting air at a velocity of 7.5 km/s with free stream Knudsen numbers ranging from 0.028 to 22.73. The results of the simulations were also compared to flight data from STS-2 and STS-3. They found that the two methods compared well with the flight data at lower altitudes, and got progressively worse with increasing altitude. This study also concluded that velocity slip and temperature jump boundary conditions should be utilized in continuum methods at free stream Knudsen numbers of 0.03 or greater.

Lumpkin et al.[6] conducted a study comparing DSMC and CFD techniques on a two dimensional 70 degree blunted wedge in Mach 29 flow of a monatomic gas with free stream Knudsen numbers of 0.0162, 0.0486 and 0.146. The study found that low density was not a sufficient condition for failure of the Navier-Stokes equations, and suggests that strong gradients can also lead to failure. It was observed that the Navier-Stokes equations can be utilized to compute the flow about a blunt hypersonic vehicle for Knudsen numbers up to 0.01. The Navier-Stokes equations can still be employed for Knudsen numbers up to 0.05, but the authors suggest caution when interpreting results as some flow phenomena can be inaccurate.

Moss et al.[7] compared DSMC and CFD methods over a 70 degree blunted cone, with and without a sting attached, in a Mach 20 flow of reacting and non-reacting

nitrogen. In this study, the Navier-Stokes equations were solved with and without slip boundary conditions. The study investigated the comparison of DSMC and CFD methods at free stream Knudsen numbers of 0.032, 0.011 and 0.001. The study found that the use of slip boundary conditions would, in general, improve the agreement with DSMC. It was also found that there were significant differences between the two methods at a Knudsen number of 0.032, which differs from the results of Lumpkin et al.[6]. Even at the lowest Knudsen number of 0.001, there were differences in the heat flux on the sting that were as large as a factor of two.

Olynick et al.[8] compared DSMC and CFD methods to simulate the flow about the Fire II vehicle at a velocity of 11.4 km/s in a flow of 5-species reacting air at free stream Knudsen numbers of 0.0025 and 0.01. This study utilized separate translational, rotational and vibrational temperatures in the CFD method. This study also attempted to ensure the thermal relaxation rates were the same in both of the methods. Velocity slip and temperature jump were also included in the CFD computations. The two methods were found to agree well in areas where the local Knudsen number is less than 0.1, even with chemical and thermal nonequilibrium. However, problems were seen in the presence of chemical and thermal nonequilibrium when trace species were present.

Boyd et al.[9] compared DSMC and CFD with flight data from the Stardust reentry vehicle at a free stream Knudsen number of 0.005 with a velocity of 12.6 km/s in a flow of reacting air. This study included the effects of dissociation and ionization. It was found that even though the free stream Knudsen number was in the continuum regime, there were enormous differences between CFD and DSMC for the most basic flow field properties.

A previous study by Lofthouse et al. looked at the effect of continuum breakdown

on the surface properties of a 12 inch diameter, two dimensional cylinder in a Mach 10 flow of argon at free stream Knudsen numbers from 0.002 to 0.25[10]. This study found that as the Knudsen number increased, the level of agreement between CFD and DSMC diverged. A more recent study by Lofthouse et al. examined the effects of velocity slip and temperature jump at the surface of a two dimensional, 12 inch diameter cylinder in Mach 10 and 25 flow of argon for the same free stream Knudsen numbers[11]. In this study it was found that the higher velocity did not increase the differences between CFD and DSMC. It was also observed that velocity slip and temperature jump boundary conditions improved the agreement between the two numerical methods. Another study by Lofthouse et al. investigated Mach 10 and 25 nitrogen flow over a two dimensional cylinder[12]. This study was again conducted over a range of Knudsen numbers, 0.002 to 0.25. Two more studies by Lofthouse et al.[13, 14] compared CFD and DSMC for flow of nitrogen over a wedge and a flat plate, respectively.

There has been ample research conducted comparing DSMC and CFD methods, and indeed this is still an active area of research. However, most of these comparisons have been over a narrow range of Knudsen numbers and include complicated models for thermal and chemical nonequilibrium. The work performed by Lofthouse et al. started with basic comparisons and added complexity. This work continues this trend, as discussed in the next section.

1.4 Scope of Current Work

The purpose of this work is to accurately characterize the effects of continuum breakdown on hypersonic aerothermodynamics. This has to be performed by starting out with simple simulations and then adding complexity to determine individual

effects on continuum breakdown. The work performed by Lofthouse et al.[15] began this effort by characterizing breakdown over a two dimensional cylinder and wedge in flows of argon and nitrogen. The first part of this study extends this to a flow of nitrogen over a 12 inch sphere for Mach 10, 25 and 45 flow to be able to consider a geometry that is more representative of reentry vehicles. This study also includes a higher velocity where vibrational nonequilibrium is expected to be more important. This study then continues on to examine the effects of continuum breakdown in Mach 25 flows of reacting nitrogen and air over a 12 inch diameter sphere in flow regimes from continuum to rarefied gas. This will add the complexity of thermal and chemical nonequilibrium.

While the main focus of this work has been on characterizing the effect of continuum breakdown, a secondary focus has been on investigating and improving the physical models within both numerical techniques to ensure they give similar physical solutions to the flow being simulated. The research conducted on the physical models are enumerated below:

1. Investigate physical models for transport properties in both CFD and DSMC methods

2. Improve the thermal relaxation models in both techniques

   - Include a separate rotational energy equation in the CFD method
   - Modify the vibrational relaxation model in the DSMC procedure

3. Investigate and improve the chemical rates utilized in both methods

   - Utilize the rotational temperature in a three-temperature model for rate calculations in the CFD procedure

- Modify the preferential dissociation model in the CFD method

- Include and evaluate a chemical equilibrium model in the DSMC technique

While this research is not concerned with the development of a hybrid technique, the research conducted in this study can be applied to a CFD-DSMC hybrid method.

An outline of this dissertation is as follows. Chapter II gives a description of the governing equations utilized to simulate hypersonic gas flows, from the Boltzmann equation to the Navier-Stokes equations. Then, a description of the numerical methods of simulating hypersonic flows is given. The Boltzmann equation can be numerically solved, but the direct simulation Monte Carlo technique can be utilized more efficiently to emulate the Boltzmann equation. The Navier-Stokes equations can be solved employing computational fluid dynamics techniques. A discussion on the strengths and weaknesses of both of these numerical methods is included. Finally, descriptions of the numerical codes LeMANS and MONACO are provided, along with the capabilities of both codes.

Chapter III gives a description of the various physical models utilized in CFD and DSMC for the simulation of hypersonic flows. A goal of this research has been focused on investigating physical models within both numerical methods to ensure the two methods give similar physical solutions to the flow being simulated. It is important in this study to assure the differences seen in the results are from the underlying assumptions of the two methods, and not from the physical models being utilized. This chapter focuses on changes to the physical models required to ensure consistency in both methods, from transport properties and thermal relaxation in CFD, to equilibrium chemistry in DSMC.

Chapter IV discusses the effects of continuum breakdown over a hypersonic sphere. This chapter will examine diatomic gases, such as nitrogen, adding the

complexity of thermal nonequilibrium. The temperatures present in these cases are high enough for dissociation to occur. However, only thermal nonequilibrium effects are included in this chapter. This chapter investigates the new rotational nonequilibrium capability of the CFD method. It also gives a more detailed look at the slip boundary conditions, comparing DSMC and CFD with and without slip boundary conditions. The final portion of this chapter compares the axisymmetic sphere case to a two dimensional cylinder case.

Chapter V continues to explore the effects of continuum breakdown on the surface properties of a 12 inch sphere in a Mach 25 flow of reacting nitrogen and reacting air. Previous work has focused on single species gas simulations, so this chapter will present results with the added complexity of multiple species. Since there are multiple species now being simulated, reacting flow can also be considered.

Chapter VI discusses the trends seen in the results by examining the stagnation pressure coefficient, the stagnation heat flux coefficient, and the drag coefficient for all cases presented in this thesis. This is performed to be able to more easily discern the fundamental differences seen in CFD and DSMC over the whole range of Mach and Knudsen numbers presented in this work.

Chapter VII gives conclusions drawn from the results obtained, and future work is proposed.

1.4.1 Unique Contributions

Even though there have been prior studies comparing the DSMC and CFD methods, this research makes several unique contributions to the field.

1. This is a numerical study that starts off with basic simulations and slowly increases the complexity. Many published studies compare with experiments or

flight tests and therefore contain complicated thermal and chemical nonequilibrium models. This study continues the work of Lofthouse et al., and as a result does not have to start with the most basic simulations and can instead build off of work previously performed. First, the complexity of a sphere is added to consider a geometry that is more representative of real flight vehicle. This is performed to quantify the effects of running a simulation as axisymmetric, as opposed to two dimensional, on continuum breakdown and the surface properties.

2. This work is also conducted over a wide range of flow regimes and Mach numbers. This work considers a range of flow regimes from continuum to a rarefied gas to be able to understand the effects of the degree of rarefaction on continuum breakdown and the surface properties. Unlike previous work, this study considers three Mach numbers, including Mach 45 where vibrational nonequilibrium is expected to be more important than at the lower velocities. This is performed to be able to quantify the effects of Mach number on continuum breakdown and the surface properties. No other study has compared the DSMC and CFD methods at a Mach number of 45 over a range of flow regimes from continuum to a rarefied gas.

3. A separate rotational energy equation is included into the CFD method and it is evaluated by comparing to the DSMC method. The addition of a rotational energy equation into the CFD method improves the simulation of thermal nonequilibrium, which is a common phenomena in hypersonic flows. It also helps to make truer comparisons to the DSMC method, which already employs a variable rotational energy exchange probability and therefore simulates a

separate rotational temperature. It is also important for a hybrid code where thermal nonequilibrium is important in the determination of the location of boundaries between the CFD and DSMC techniques.

4. This study evaluates the physical models in both numerical techniques to be able to ensure they give the same physical solutions. This includes modifying the transport properties, thermal relaxation, preferential dissociation and including a three-temperature model in the CFD method. The vibrational relaxation model was modified and a chemical equilibrium model was included in the DSMC technique.

5. Finally, this study adds the complexity of gas mixtures and reacting flow to be able to study the effects of these processes on continuum breakdown and the surface properties. This study is conducted over a wide range of flow regimes, which has never been done before for comparisons between the CFD and DSMC methods with reacting flow. This is performed for both reacting nitrogen and reacting air in a Mach 25 flow. The addition of gas mixtures and reacting flow makes these simulations more representative of real hypersonic flows.

CHAPTER II

Simulation of Hypersonic Flows

2.1   Introduction

This chapters gives a description of the basic governing equations utilized to simulate gas flows, from the Boltzmann equation to the Navier-Stokes equations. The basic numerical methods of simulating hypersonic flows are then discussed. The Boltzmann equation can be numerically solved, but the direct simulation Monte Carlo technique can be utilized to emulate the Boltzmann equation. The Navier-Stokes equations can be solved employing computational fluid dynamics techniques. The strengths and weaknesses of both of these numerical methods are discussed in further detail. A short discussion on hybrid methods is also included. Finally, a discussion of the numerical codes LeMANS and MONACO is included, along with a description of the capabilities of both codes.

2.2   Governing Equations of Gas Flow

In this section, the governing equations utilized for the simulation of gas flows are described. First, the Boltzmann equation is described, then an explanation of how the conservation equations are derived from the Boltzmann equation is provided. The Chapman-Enskog expansion is discussed along with a description of how the

Navier-Stokes equations are derived. A brief discussion of higher-order methods is also included in this section.

2.2.1 Boltzmann Equation

The Boltzmann equation describes the evolution of the velocity distribution function (VDF) through phase space. Phase space is a combination of physical space and velocity space. The velocity distribution function, f, represents the probability that a particle at a given spatial location will have a certain velocity at a given point in time. Therefore, f is a function of seven variables; position $\mathbf{r}\,(x, y, z)$, velocity $\mathbf{c}\,(c_x, c_y, c_z)$ and time. From the Boltzmann equation, there are three processes that affect the evolution of the VDF in time; the convection of particles across physical space due to particle velocity, the convection of particles across velocity space due to an external force and intermolecular collisions scattering particles in and out of phase space, as shown in Eq. (2.1). It should be noted that the external force is neglected in this work.

$$\frac{\partial}{\partial t}\left[nf\left(c_i\right)\right] + c_j\frac{\partial}{\partial x_j}\left[nf\left(c_i\right)\right] + \frac{\partial}{\partial c_j}\left[F_j nf\left(c_i\right)\right] = \left\{\frac{\partial}{\partial t}\left[nf\left(c_i\right)\right]\right\}_{coll} \qquad (2.1)$$

where c_i is the velocity of the ith particle, F is an external force, n is the number density, f is the velocity distribution function and the collision term on the right hand side is given by Eq (2.2) for binary collisions.

$$\left\{\frac{\partial}{\partial t}\left[nf\left(c_i\right)\right]\right\}_{coll} = \int_{-\infty}^{\infty}\int_{0}^{4\pi} n^2\left[f\left(c_i'\right) f\left(z_i'\right) - f\left(c_i\right) f\left(z_i\right)\right] g\sigma d\Omega dz_i \qquad (2.2)$$

where g is the relative velocity between two colliding particles, $\sigma d\Omega$ is the differential collision cross-section of the colliding particles and c_i' is the post collision velocity of

a particle with initial velocity of c_i. The total effect of collisions on the VDF is found by integrating over particles of all velocities and all collision cross-sections.

The Boltzmann equation is valid for all flow regimes, from continuum to rarefied. However, the collision term has been derived under the assumption of binary collisions, limiting it to dilute fluids. Analytical solution of the Boltzmann equation is limited to simple collision-less flows. For more complicated collisional flows, a numerical solution of the Boltzmann equation is required.

Numerical solution of the Boltzmann equation is computationally intensive due to its high dimensionality and complicated collision integral. It requires not only physical space discretization, but also velocity space discretization. This requires at least a six dimensional mesh for a simulation. If internal energy modes are desired, which is the case for hypersonic flows, they must be discretized as well creating further dimensions. There is then a problem with how to discretize the velocity and internal energy space, to determine how many levels are required for efficient and accurate solution to the Boltzmann equation in a hypersonic flow. This is not well known, but there is research beginning to address this issue in shock waves[16] and hypersonic blunt body flows[17].

The numerical expense of a Boltzmann solver can be reduced by approximating the collision term with an algebraic expression utilizing the Bhatnagar-Gross-Krook (BGK) method[18], as given in Eq. (2.3). This method can be employed in a Boltzmann solver to replace the collision term on the right hand side. This allows the Boltzmann equation to be solved in a more numerically efficient manner using standard computational fluid dynamic techniques.

$$\left\{\frac{\partial}{\partial t}\left[nf\left(c_i\right)\right]\right\}_{coll} = \nu n\left(f_B - f\right) \tag{2.3}$$

where ν is a characteristic relaxation time, n is the number density and f_B is the Maxwellian distribution. This model is a linearized simplification of the complicated, highly nonlinear, collision term in the Boltzmann equation. The physics of the collision term are ignored in favor of a model where the distribution function decays towards an equilibrium distribution. Holway[19] has proposed the ellipsoidal statistical BGK (ES-BGK) method to obtain better agreement with the Boltzmann equation, as given in Eq. (2.4).

$$\left\{ \frac{\partial}{\partial t} \left[nf(c_i) \right] \right\}_{coll} = \nu n \left(f_G - f \right) \tag{2.4}$$

where f_G is an anisotropic gaussian distribution function. This model corrects for the nonphysical constraint in the BGK model of unity Prandtl number. The BGK model can also be utilized in hybrid methods, which are discussed briefly in a later section.

The Boltzmann equations can be utilized in any flow regime, but are numerically expensive and complicated to solve.

2.2.2 Moments of the Boltzmann Equation

Instead of trying to solve the Boltzmann equation, which is difficult and numerically costly, it can be employed to derive the conservation equations. The conservation equations can be found by taking the zeroth, first and second order moments of the Boltzmann equation. The zeroth, first and second order moments correspond to the mass, momentum and energy conservation equations. Taking a moment requires multiplying the distribution function f by a quantity Q and integrating over all velocity space, as shown in Eq. (2.5).

$$\langle Q \rangle = \int_{-\infty}^{\infty} Q\left(c_i\right) f\left(c_i\right) dc_i \tag{2.5}$$

where c_i is the particle velocity, and Q is a function of velocity. When Q takes the form of c_i^n, then $\langle Q \rangle$ is known as the nth moment of the distribution function. The process of taking moments eliminates the velocity dependence on Q and gives the average value. Taking the moments of the Boltzmann equation results in Maxwell's equation of change, as shown in Eq. (2.6).

$$\frac{\partial}{\partial t}\left[n\langle Q \rangle\right] + \frac{\partial}{\partial x_j}\left[n\langle c_j Q \rangle\right] + nF_j \frac{\partial}{\partial c_j}\left[\langle Q \rangle\right] = \Delta\left[Q\right] \tag{2.6}$$

where the external force is ignored in this work and the term on the right hand of the equation is due to collisions. The collision term is zero if the value of Q is chosen to be three of the five collisional invariants[20], $Q = \{m, m\mathbf{c}, \frac{mc^2}{2}\}$.

Utilizing the above mentioned Q values in Maxwell's equation of change gives the conservation equations for mass (2.7), momentum (2.8) and energy (2.9).

$$\frac{\partial}{\partial t}\left[\rho\right] + \frac{\partial}{\partial x_k}\left[\rho\left\langle c_k \right\rangle\right] = 0 \tag{2.7}$$

$$\frac{\partial}{\partial t}\left[\rho\left\langle c_k \right\rangle\right] + \frac{\partial}{\partial x_k}\left[\rho\left\langle c_k c_i \right\rangle\right] = 0 \tag{2.8}$$

$$\frac{\partial}{\partial t}\left[\rho\left\langle \frac{c^2}{2} \right\rangle\right] + \frac{\partial}{\partial x_k}\left[\rho\left\langle c_k \frac{c^2}{2} \right\rangle\right] = 0 \tag{2.9}$$

The conservation equations become the well known Euler equations if the distribution function used to find the moments is the Boltzmann equilibrium, or Maxwellian, distribution[4]. The Maxwellian distribution, Eq. (2.10), is found by setting the collision term in the Boltzmann equation to zero.

$$f_B\left(c_i\right)dc_i = \left(\frac{m}{2\pi k_{BOLTZ}T}\right)^{\frac{3}{2}}\exp\left[-\frac{m}{2k_{BOLTZ}T}\left(c_i - \langle c_i\rangle\right)^2\right]dc_i \qquad (2.10)$$

where C_i is the thermal velocity, that is found by subtracting the average velocity from the particles actual velocity, $|c_i - \langle c_i\rangle|$. The Euler equations are valid for equilibrium flow simulations. For flows where there is nonequilibrium present, at higher Knudsen numbers, a more detailed set of equations that takes into account a departure from equilibrium is required.

2.2.3 Chapman-Enskog Expansion

The Chapman-Enskog expansion[2] introduces perturbations into a Maxwellian distribution, as shown in Eq. (2.11).

$$\hat{f} = \hat{f}_B\left(1 + \xi\phi_1 + \xi^2\phi_2 + \ldots\right) \qquad (2.11)$$

where $\hat{f}$ is the non-dimensional velocity distribution function in terms of the parameter ξ. Taking only the first term of the Chapman-Enskog expansion, the Euler equations are obtained, as mentioned in the previous section. If two terms are kept, the Navier-Stokes equations are found, and if three terms are kept, the Burnett equations are found[21]. The Chapman-Enskog expansion for two terms[22] is given in Eq. (2.12).

$$\begin{aligned}
\Gamma = (1 + \xi\phi_1) = 1 + &\left(\hat{q}_x\hat{C}_x + \hat{q}_y\hat{C}_y + \hat{q}_z\hat{C}_z\right)\left(\frac{2}{5}\hat{C}^2 - 1\right) \\
&- 2\left(\hat{\tau}_{x,y}\hat{C}_x\hat{C}_y + \hat{\tau}_{x,z}\hat{C}_x\hat{C}_z + \hat{\tau}_{y,z}\hat{C}_y\hat{C}_z\right) \\
&- \hat{\tau}_{x,x}\left(\hat{C}_x^2 - \hat{C}_z^2\right) - \hat{\tau}_{y,y}\left(\hat{C}_y^2 - \hat{C}_z^2\right) \qquad (2.12)
\end{aligned}$$

where $\hat{C}$ is the velocity normalized by the thermal velocity, $\hat{q}$ is the normalized heat flux, and $\hat{\tau}$ is the normalized shear stress. This two-term Chapman-Enskog distribution function can be employed to derive the Navier-Stokes equations.

2.2.4 Navier-Stokes Equations

The Navier-Stokes equations can be derived by utilizing the Champan-Enskog velocity distribution in the Boltzmann moment equation. Since the Navier-Stokes equations are derived on the assumption of small perturbations from equilibrium, it is therefore only valid in near equilibrium flows. The Navier-Stokes equations for a single species gas with no body forces and a single temperature can be written as,

$$\frac{\partial \rho}{\partial t} + \frac{\partial}{\partial x_i}[\rho u_i] = 0 \tag{2.13}$$

$$\frac{\partial}{\partial t}[\rho u_i] + \frac{\partial}{\partial x_i}[\rho u_i u_j + p - \tau_{ij}] = 0 \tag{2.14}$$

$$\frac{\partial}{\partial t}[\rho e] + \frac{\partial}{\partial x_i}[\rho u_i e + p u_i - \tau_{ij} u_i + q_i] = 0 \tag{2.15}$$

where τ_{ij} is the shear stress tensor, q_i is the heat flux vector, e is the total specific energy and u_i is the average velocity. It should be noted that the Euler equations can be recovered if τ_{ij} and q_i are equal to zero. The shear stress and heat flux arise from translational nonequilibrium in the flow[2] and are given as,

$$\tau_{ij} = \mu \left(\frac{\partial u_i}{\partial x_j} + \frac{\partial u_j}{\partial x_i} \right) - \frac{2}{3}\mu \frac{\partial u_i}{\partial x_i}\delta_{ij} + \mu_B \frac{\partial u_i}{\partial x_i}\delta_{ij} \tag{2.16}$$

$$q_i = -\kappa \frac{\partial T}{\partial x_i} \tag{2.17}$$

where κ is the coefficient of thermal conductivity, μ is the coefficient of viscosity, and μ_B is the bulk coefficient of viscosity. The thermal conductivity and viscosity are discussed in more detail in Chapter III. The thermal conductivity and viscosity come about due to translational nonequilibrium, while the bulk viscosity comes about due to rotational nonequilibrium[2, 23]. As a result, the bulk viscosity is zero in a monatomic gas, and is normally ignored in diatomic gases, according to Stokes' hypothesis. The above equations for τ_{ij} and q_i are given in terms of the macroscopic properties. Using the Chapman-Enskog distribution, the shear stress and heat flux can be found in terms of the moments of the velocity distribution function,

$$\tau_{ij} = \rho \langle C_i C_j \rangle - \rho \left\langle \frac{C^2}{3} \right\rangle \delta_{ij} \tag{2.18}$$

$$q_i = \rho \left\langle \frac{C_i C^2}{2} \right\rangle \tag{2.19}$$

A final closure equation is still required to be able to solve the Navier-Stokes equations. Usually an equation of state is utilized, such as the perfect gas equation of state given in Eq. (2.20).

$$p = \rho R_{gas} T \tag{2.20}$$

where R_{gas} is the specific gas constant.

The Navier-Stokes equations are typically utilized to simulate gas flows in the continuum regime, the customary limit is a Knudsen number of 0.01. The Navier-Stokes equations account for the transfer of energy and momentum caused by translational nonequilibrium. The equations are closed using shear stress, transfer of momentum, and heat flux, transfer of energy, which assumes linear functions of macroscopic flow

gradients. In nonequilibrium flow, these gradients can occur over a few mean free paths making the linear assumption invalid. The transfer of energy and momentum is carried by particles, which may involve a nonlinear process. This is captured by the Boltzmann equation, but is lost in the derivation of the Navier-Stokes equations. Therefore, the Navier-Stokes equations are only valid in the continuum regime. However, they can be extended into the transition regime by use of slip boundary conditions, as discussed in Chapter III.

2.2.5 Extended Hydrodynamic Equations

If more terms are retained in the Chapman-Enskog expansion, then more information can be derived from the Boltzmann equation. If the first three terms are kept, the Burnett equations can be derived, and if the first four terms are retained, the super Burnett equations are found. These equations can give a more accurate description of nonequilibrium flow, although there is research that suggests that the Burnett equations cannot be utilized where the Navier-Stokes equations have already failed[24]. There are some additional issues with higher moment equations, including numerical stability and a failure to satisfy the second law of thermodynamics[25].

There are also higher moment methods, such as Grad's 13 moment method. It has been shown that Grad's 13 moment equations give the same results as the Chapman-Enskog expansion[26]. The Boltzmann moment equation always contains a higher order moment, for example the first order moment equation contains a second order moment. The Navier-Stokes equations are closed through the use of the shear stress and heat flux. In higher order moment methods, the higher order moments are related back to lower order moments in order to close the equation set. There are many other higher order methods, after all there is no limit on the number

of moments of the Boltzmann equation that can be taken. While these systems of equations are valid in higher Knudsen number flows, there are several issues[15] that make them impractical for use with hypersonic flows.

2.3 Numerical Methods

The previous section discussed various fundamental equations utilized to model gas flows, most notably the Boltzmann equation and the Navier-Stokes equations. In this section, two numerical methods that are utilized to compute hypersonic flows are discussed.

2.3.1 Direct Simulation Monte Carlo

Numerically solving the full Boltzmann equation can become computationally intensive due to the multi-dimensional nature of the equation and the complicated collision integral. A probabilistic particle method can be used to simulate the physical processes in the Boltzmann equation instead of trying to numerically solve it. The direct simulation Monte Carlo (DSMC) method[3] is a probabilistic particle method that simulates the particles moving through a flow domain, colliding with other particles and surfaces. In DSMC, each simulated particle represents a large number of real particles. Every simulated particle has a velocity, internal energy and a specific location. The collisions between particles is dealt with in a probabilistic manner. It has been shown that this process converges to the Boltzmann equation as the number of particles goes to infinity[1].

In the DSMC method, the collisions are uncoupled from the particle motion, meaning the DMSC method has two basic steps. First, the particles are moved, without collisions, along their velocity vectors for a time step. Boundary conditions, such as collisions with the wall and particles entering/leaving the computational

domain, are also applied in this step. In the second step, particle pairs are randomly chosen within the same cell to collide. It has been found that the post collision scattering angle is insignificant to the final result, therefore it is chosen at random. The post collision velocities are found using the particle trajectories and utilizing conservation of momentum and energy, assuming elastic collisions. To determine the exchange of internal energy, the Larsen-Borgnakke[27] model is utilized to calculate inelastic collisions.

A simulation is started with a computational grid and particles are set with a Maxwellian distribution. The two step process is repeated until a steady-state is established. Once a steady-state is reached, the molecular particle properties are sampled over many time steps in order to reduce the scatter in the macroscopic properties of each cell. The fluxes of momentum and energy from particles at the surface is also sampled over many time steps to determine the shear stress, pressure and heat flux at the surface. Particles are randomly scattered after a collision with the surface and a new post collision velocity is sampled from a Maxwellian distribution with zero bulk velocity and based on the specified surface temperature.

The probability P of a collision between two simulated particles over a time interval Δt is equal to the ratio of the volume swept out by the total collision cross-section, σ_T, moving at a relative speed, g, between them to the volume of the cell[3],

$$P = W \sigma_T g \Delta t / V_{cell} \qquad (2.21)$$

where W is the number of real gas particles represented by simulated particles, and V_{cell} is the volume of the cell. This probability is utilized in the DSMC method to locally determine the number of collision pairs selected in each cell per time step. Bird's no-time-counter (NTC) scheme[3] is utilized to select collision pairs. With the

number of collisions required per cell, particle collision pairs are randomly selected within each cell, a probability of collision evaluated for each pair, and elastic or inelastic collisions are performed for each pair selected for collision.

It should be noted that there are several limitations to the above DSMC procedure. The time step must be smaller than the mean collision time in order for the collision and movement subroutines to be separated. Typically, the time step needs to be about a third of the mean collision time. If a constant time step is utilized, the DSMC time step is limited by the smallest mean collision time in the simulation. When the time step is set to be too large it leads to "bad" collisions, where the probability of colliding is greater than one. It is best to keep "bad" collisions to less then 1% of the total number of collisions. Since the colliding pairs are chosen at random within a cell, the cell must be smaller than the local mean free path. Otherwise, particles more than a mean free path apart can be chosen for collision. This is physically incorrect, and will introduce numerical diffusion. However, this is only true in the direction of the maximum gradient, so cell stretching in the direction perpendicular to the maximum gradient is acceptable and is briefly discussed later in this chapter. In order to obtain statistically meaningful macroscopic results, there must be a sufficient number of particles per cell. In general, 20 particles per cell is sufficient. When dealing with reacting flows it is recommended to have to 20 particles of each species per cell to get proper sampling of all species. In reacting flows, when trace species are present, there can be cells that contain only a few particles which can cause problems with calculating the correct collision rates and properly sampling for the macroscopic properties. This means that trace species might not be undergoing collisions allowing particles to move to areas where they physically should not be. As the Knudsen number decreases, the number of cells required to obtain a phys-

ically accurate solution increases, which increases the number of required particles causing the numerical cost of the simulation to increase. Even though the DSMC method is numerically expensive, a full Boltzmann solver is an order of magnitude more expensive while giving comparable results[28].

The BGK method can be applied to a Boltzmann equation as well as the DSMC method[29, 30]. Instead of having the normal DSMC collision procedure, the BGK method is utilized to update the velocity distribution function. The post-collision velocities of particle pairs are then sampled from the BGK distribution[31]. The BGK method can be utilized well in DSMC in near equilibrium flow regimes. The ES-BGK method is better suited for higher Knudsen number flows, up to the transitional flow regime. Utilizing the BGK method, or ES-BGK method, reduces the cost by eliminating the numerically expensive collision procedure. However, this is only accurate at lower Knudsen numbers.

The DSMC method is appropriate for all gas flows, from the continuum regime to a rarefied gas. It is only limited by the computational expense at lower Knudsen number conditions.

2.3.2 Computational Fluid Dynamics

The Navier-Stokes equations can be solved numerically using traditional computational fluid dynamics (CFD) techniques. These same CFD techniques can be utilized to solve the higher order methods as well, but in this study CFD refers specifically to numerically solving the Navier-Stokes equations. Typically, in hypersonic flows, finite-volume[32] methods are utilized for CFD, however there is a growing interest in finite-element methods.

Assuming a two temperature model, a coupled translational-rotational temper-

ature and a coupled vibrational-electronic-electron temperature, the finite-volume, three dimensional conservative form of the Navier-Stokes equations can be written as[33],

$$\frac{\partial Q}{\partial t} + \frac{\partial \left(E - E_v \right)}{\partial x} + \frac{\partial \left(F - F_v \right)}{\partial y} + \frac{\partial \left(G - G_v \right)}{\partial z} = S_{cv} \tag{2.22}$$

where Q is the conserved variable vector and S_{cv} is the source term vector, both are given in Eq. (2.23).

$$Q = \left\{ \begin{array}{c} \rho_1 \\ \vdots \\ \rho_s \\ \rho u \\ \rho v \\ \rho w \\ \rho e \\ \rho e_v \end{array} \right\} \quad and \quad S_{cv} = \left\{ \begin{array}{c} \dot{\omega}_1 \\ \vdots \\ \dot{\omega}_s \\ 0 \\ 0 \\ 0 \\ 0 \\ \dot{\omega}_v \end{array} \right\} \tag{2.23}$$

where ρ_i is the density of each species, u v and w are the bulk velocities in each direction, e and e_v are specific total energy and specific vibrational energy, respectively. The source term handles changes in species concentration due to chemical reaction, $\dot{\omega}_i$, and changes in vibrational energy due to thermal relaxation, modeled with the Landua-Teller model, and chemical reactions, $\dot{\omega}_v$. The vibrational energy source term is discussed in more detail in Chapter III.

The inviscid flux vector in the x-direction, E, and the viscous flux vector in the x-direction, E_v, are given in Eq. (2.24).

$$
E = \left\{ \begin{array}{c} \rho_1 u \\ \vdots \\ \rho_s u \\ \rho u^2 + p \\ \rho uv \\ \rho uw \\ (\rho e + p) u \\ \rho e_v u \end{array} \right\} \quad and \quad E_v = \left\{ \begin{array}{c} -J_{x,1} \\ \vdots \\ -J_{x,s} \\ \tau_{xx} \\ \tau_{xy} \\ \tau_{xz} \\ \tau_{xx} u + \tau_{xy} v + \tau_{xz} w - (q_{tr,x} + q_{ve,x}) - \sum (J_{x,s} h_s) \\ -q_{ve,x} - \sum (J_{x,s} e_{ve,s}) \end{array} \right\}
$$

$$(2.24)$$

where h_i is the species enthalpy, $J_{x,i}$ is the species diffusion flux in the x-direction, τ is the stress tensor and q is the heat flux vector, which were discussed earlier in section 2.2.4. The inviscid and viscous flux vectors in the y- and z-directions are similar.

Solving the Navier-Stokes equations using CFD methods is a numerically efficient and accurate approach to model hypersonic gas flows in the continuum regime. The computational cost of a CFD simulation is a function of the number of computational cells required. The Navier-Stokes equations will give inaccurate solutions at higher Knudsen numbers, due to breakdown of the assumption of perturbation from equilibrium. This is known as continuum breakdown.

2.3.3 Hybrid Methods

One solution to the problem of continuum breakdown is a hybrid code that utilizes CFD and DSMC methods to accurately and efficiently simulate a hypersonic flow.

A hybrid code can solve the Navier-Stokes equations when the flow is considered to be in the continuum regime, and it can switch to a DSMC method when the flow is considered rarefied such as in a shock wave[4]. This process involves some way of determining when the physics of the simulation provided by the CFD method deviates from physical results; this is performed with the continuum breakdown parameter, which is discussed in more detail in the next section.

It should be noted that there are several different hybrid methods available, not just limited to a CFD-DSMC hybrid method. The idea of a hybrid is to use a more accurate but numerically expensive method, such as DSMC or a Boltzmann solver, in areas of nonequilibrium and then use a numerically less expensive method, such as BGK or CFD, in areas of near-continuum flow. This approach will give accurate results in the nonequilibrium regions while saving the numerical expense of having to run DSMC or a Boltzmann solver over the whole flow domain.

There has been work on a unified solver where the full Boltzmann equation is solved in areas of nonequilibrium and in the continuum regime the collision integral in the Boltzmann equation is replaced by a "Maxwellization" of the distribution function[34], which sounds similar to a Boltzmann-BGK hybrid method. There are also hybrid Boltzmann-CFD solvers; Le Tallec et al.[35] utilized the Navier-Stokes equations in the continuum areas. There are also all particle hybrid methods. Recently, Burt et al.[28] proposed a low-diffusion equilibrium particle method, where particles are convected along streamlines within continuum regions, which effectively reduces the numerical diffusion. The upside to all particle methods is the ease of information transfer between nonequilibrium and continuum regions. There is currently research being conducted on the development of various different hybrid methods to be able to accurately and efficiently simulate multi-scale gas flows.

While this thesis is not concerned with the development of a hybrid technique, the research conducted in this study can be applied to a CFD-DSMC hybrid method.

Continuum Breakdown Parameter

A hybrid CFD-DSMC method needs a way of determining when the flow is in the continuum regime; this is achieved with a continuum breakdown parameter. This continuum breakdown parameter will notify the code that the CFD method can no longer be employed and that DSMC needs to be utilized to correctly simulate the flow field. Bird[36] has proposed a continuum breakdown parameter, P, as given in Eq. (2.25)

$$P = \frac{1}{\nu}\left|\frac{D(\ln\rho)}{Dt}\right| = M\sqrt{\frac{\pi\gamma}{8}}\frac{\gamma}{\rho}\left|\frac{dp}{ds}\right| \qquad (2.25)$$

where M is the local Mach number and s is the distance along a streamline. Bird found that a value of P over 0.05 provides an indication of continuum breakdown. This parameter predicts breakdown well in expansion flows but has problems when the Mach number is small. Since P is directly proportional to the Mach number, it will tend to zero as the Mach number goes to zero regardless of the amount of breakdown in the flow. Boyd, et al.[37] suggested the use of the maximum gradient length local Knudsen number as a continuum breakdown parameter given in Eq. (2.26).

$$Kn_{GLL} = \frac{\lambda}{Q}\left|\frac{dQ}{dl}\right| \qquad (2.26)$$

where the derivative is taken in the direction of maximum gradient, and Q is a variable of interest such as density, temperature or pressure. It has been found that a value of Kn_{GLL} above 0.05 indicates continuum breakdown has occurred. Camberos

et al.[38] recommended the use of entropy production rate as a continuum breakdown parameter. There have been several other breakdown parameters proposed: Tiwari suggested a breakdown parameter[39],

$$||\Phi|| = \frac{1}{\rho RT} \left(\frac{2}{5} \frac{|q^2|}{RT} + \frac{1}{2} ||\tau||_E^2 \right)^{\frac{1}{2}} \tag{2.27}$$

where ρ is the density, R is the gas constant, T is the temperature, $||\tau||_E^2$ is the Euclidian norm of the stress tensor, and q is the heat flux vector. Also, Garcia et al.[40] has suggested the use of the B parameter,

$$B = max \left\{ |\hat{\tau}_{ij}|, |\hat{q}_i| \right\} \tag{2.28}$$

where $\hat{\tau}_{ij}$ is the normalized stress tensor, and $\hat{q}_i$ is the normalized heat flux vector. This study utilizes the gradient length local Knudsen number as the breakdown parameter.

2.4 Computational Codes

The previous sections have outlined the governing equations and numerical methods utilized to simulate gas flows. The following sections summarize the numerical codes, LeMANS and MONACO, that are utilized in this study to perform the CFD and DSMC simulations, respectively. A discussion of mesh refinement for both methods is also included in this section.

2.4.1 MONACO

The DSMC simulations are performed using MONACO[41], a code developed at the University of Michigan by Boyd et al. MONACO utilizes DSMC to accurately simulate rarefied gas flows around hypersonic vehicles. MONACO is a paral-

lel, unstructured, 2D/3D DSMC code, and it includes variable vibrational[42] and rotational[43] energy exchange models. MONACO can use either the variable hard sphere(VHS) or variable soft sphere(VSS) collision models[3]; the VHS model is employed in this study. The cell size of the final mesh needs to be of the order of the local mean free path, and the time step needs to be smaller than the local mean collision time. To obtain accurate results from a DSMC simulation, at least twenty particles per cell is suggested[3], and this is achieved in every simulation for this study.

2.4.2   LeMANS

The CFD simulations are performed by solving the Navier-Stokes equations by use of the code LeMANS, developed at the University of Michigan for the simulation of hypersonic reacting flows[44, 45]. LeMANS is a parallel, unstructured 2D/3D, finite-volume CFD code. LeMANS has the ability to simulate gases in chemical and thermal nonequilibrium. LeMANS employs a modified Steger-Warming Flux Vector Splitting scheme[46] to discretize the numerical fluxes between cells, which has low dissipation and is appropriate near boundary layers. A point implicit method is employed for the time march, but after a few hundred iterations is switched to a line implicit method for faster convergence. Even though LeMANS can handle unstructured meshes, all the simulations performed for this study are carried out using structured meshes.

2.4.3   Mesh Refinement

The final mesh used for each DSMC simulation is adapted by hand from previous simulations such that the cell size is of the same order as the mean free path. For this study, a hybrid mesh is utilized with cell stretching. A hybrid mesh is one where

both a structured and an unstructured grid is utilized. In this case, a structured grid is employed along the fore body surface while an unstructured mesh is used everywhere else in the flow field as shown in Fig. 2.1. For the structured grid, cell stretching is employed. This means the cell widths are adapted to be on the order of a mean free path while the cell heights are stretched larger than the mean free path. The amount of cell stretching varies depending on the global Knudsen number. The grid shown in Fig. 2.1 has cells stretched by a factor of 8 near the stagnation point. The amount of cell stretching decreases farther away from the stagnation point, and eventually the cells are no longer stretched. This procedure creates a larger cell volume so more particles can populate the cells near the stagnation point. This is important in axisymmetric simulations where it is difficult to obtain an appropriate number of particles per cell[47]. Cell stretching does not affect the simulation results because the primary flow gradients along the stagnation line are aligned with the cell widths, which are small enough to properly simulate the flow. Figure 2.1(d) shows the unstructured mesh on top of a structured mesh near the stagnation point. From this figure it can be seen that the stretched cells give a much larger area than unstructured cells thus allowing more particles to populate the area near the stagnation point.

The final mesh for CFD simulations is adapted by hand to align to the shock as well as possible. Since the location of the shock is not known *a priori*, the first step performed is a simulation on a large, coarse mesh to be able to ascertain the approximate location of the shock. The second grid made is adapted to align with the shock by moving the boundary. The approximate shock location is given by the maximum gradient length local Knudsen number. Once the mesh is aligned with the shock, a grid independence study is performed to determine the final mesh density

(a) Full Grid

(b) Fore Body

(c) Stagnation Point

(d) Hybrid and Unstructured Mesh
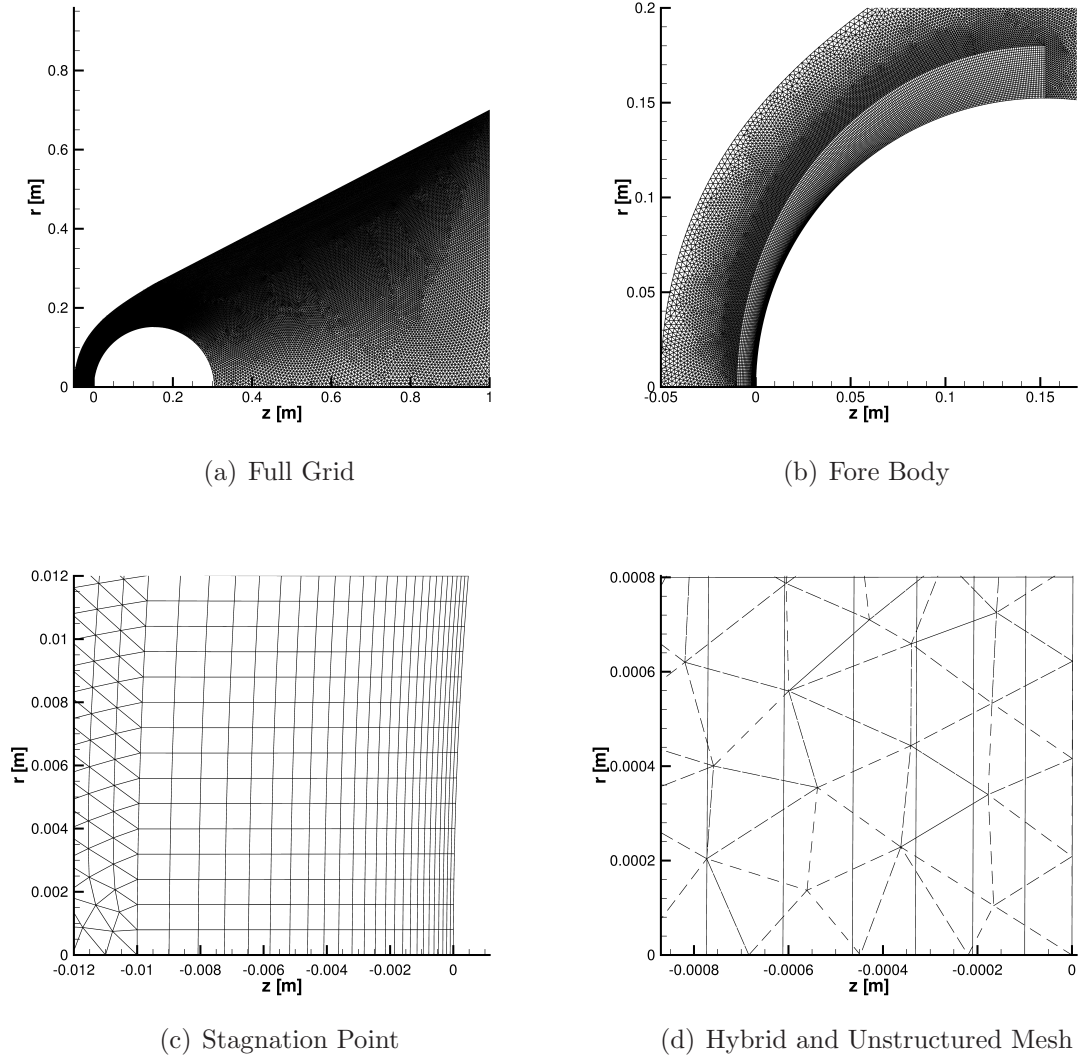
Figure 2.1: The final tailored grid for the Mach 10 global Knudsen number 0.01 case for DSMC, all other DSMC grids are similar

utilized for every case. In some cases, the global Knudsen number is high enough that any solution achieved is considered grid independent. Figure 2.2 gives the final tailored grid for all four global Knudsen numbers in a Mach 25 flow of nitrogen. It is interesting to note that the grid density is much higher in DSMC than for CFD at $Kn_\infty = 0.002$, as seen in Fig. 2.2(a). As the global Knudsen number grows, the grid density for DSMC decreases dramatically. At a global Knudsen number of 0.25, the CFD mesh has a higher grid density than DSMC, as seen in Fig. 2.2(d). It can be observed that in all cases, the grid for DSMC covers a larger area. This is due to the DSMC method predicting the shock to be thicker than the CFD method. It should be noted that the DSMC grids are also adapted to align with the shock. This eliminates as many cells in the free stream as possible, decreasing the numerical cost.
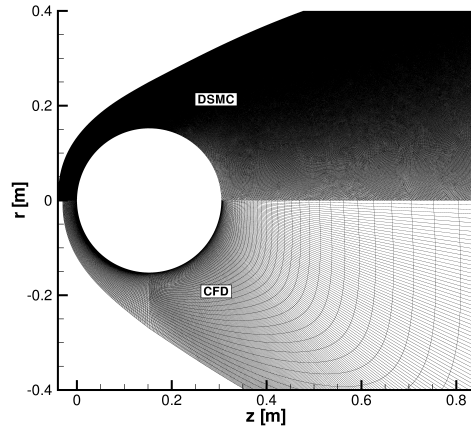
(a) $Kn_\infty = 0.002$
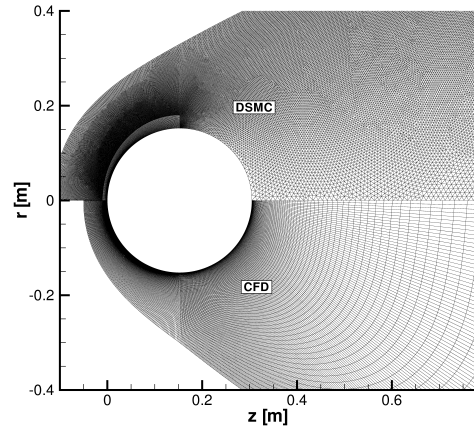
(b) $Kn_\infty = 0.01$
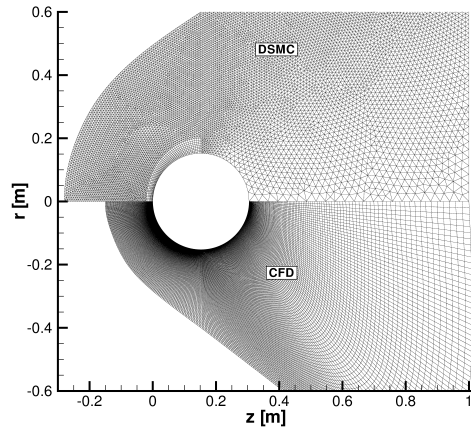
(c) $Kn_\infty = 0.05$
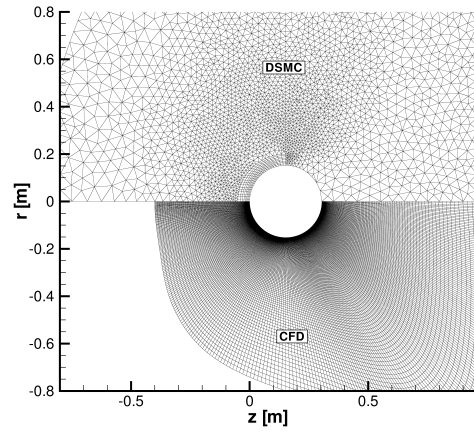
(d) $Kn_\infty = 0.25$

Figure 2.2: The final tailored grids for the Mach 25 cases at various global Knudsen numbers for DSMC and CFD

CHAPTER III

Physical Models for Hypersonic Flow

3.1 Introduction

From the previous chapter it is clear that the DSMC method and the CFD method are fundamentally different in their approaches to simulating gas flows. Even though the two methods are different, they should provide similar physical solutions in regimes where they are valid. One goal of this research is focused on investigating physical models within both codes to ensure the two methods give similar physical solutions to the flow being simulated. It is important to this study to assure the differences seen in the results are from the underlying assumptions of the two methods and not from the physical models being utilized. This research focuses on changes to the physical models required to ensure consistency in both methods, from transport properties and thermal relaxation in CFD, to equilibrium chemistry in DSMC. The following sections discuss in more detail the changes made in the physical models in both techniques.

In a hybrid code that utilizes both CFD and DSMC methods, it is of critical importance that the physical models are consistent across interfaces in the flow field. For that reason, all the physical models discussed here can also be employed in a CFD-DSMC hybrid code.

3.2 Transport Properties

In an effort to make the CFD and DSMC methods compare as well as possible, the first physical model investigated is the transport properties in CFD. There is no equivalent physical model for the transport properties in DSMC, because it is a particle method. However, the variable hard sphere (VHS) model in DSMC is made to better match the coefficient of viscosity by allowing the collision cross sections to vary with the relative velocity[3].

In areas of nonequilibrium, such as shock-layers, accurate models of transport of mass, momentum and energy are required to obtain an accurate CFD solution of a hypersonic flow field. Whenever the flow is nonequilibrium, there will be nonuniform spatial distributions, or gradients, of macroscopic properties, such as density, which will give rise to transport within the gas due to molecular motion, in this case transport of mass. A gradient in the velocity of a viscous gas will result in the transport of momentum, and a temperature gradient will give rise to the transport of energy. The results of the molecular processes for the transfer of mass, momentum and energy are the macroscopic phenomena of diffusion, viscosity and heat conduction[2]. The transport properties are also important in the boundary layer where variations in velocity and temperature lead to the shear stress and heat flux acting on the body.

In this work, there are simulations of single and multi-species flows. As a result, a mixing rule for the transport properties has to be utilized for the multi-species flows. There are two different models in the CFD method to calculate the transport properties of gas mixtures. The first utilizes Wilke's mixing rule[48], using Blottner's curve fits for viscosity and Eucken's relation for thermal conductivity. The second utilizes Gupta's mixing rule[49], employing collision cross section data. Wilke's mixing rule

is acceptable for temperatures less than 10,000 K; for high speed and high temperature flows, Gupta's mixing rule is the recommended method[50]. Both models are discussed in more detail below.

3.2.1 Wilke's Mixing Rule

In this model, the mixture coefficients of viscosity and thermal conductivity are found using the species coefficients, as given in Eq. (3.1):

$$\mu = \sum_s \frac{X_s \mu_s}{\phi_s} \qquad \kappa = \sum_s \frac{X_s \kappa_s}{\phi_s} \tag{3.1}$$

where X_s is the species mole fraction, μ_s is the species coefficient of viscosity, κ_s is the species coefficient of thermal conductivity for each energy mode, and ϕ_s is a dimensionless constant for each species.

The coefficient of viscosity for each species is originally calculated using Blottner's curve fit, as given in Eq (3.2).

$$\mu_s = 0.1 \exp\left[(A_s \ln T + B_s) \ln T + C_s\right] \tag{3.2}$$

where A, B and C are constants for each species. While this model works well for low temperature flows (less than 10,000 K), there is no way to make sure that this model agrees with the DSMC method at all simulated conditions.

In this study, the variable hard sphere (VHS) model[3] is utilized in the DSMC method. In order to ensure that the transport properties are the same in both CFD and DSMC, LeMANS is modified to use the same viscosity model as the VHS method[51] as given in Eqs. (3.3) and (3.4).

$$\mu_s = \mu_{ref,s} \left(\frac{T}{T_{ref,s}}\right)^\omega \tag{3.3}$$

$$\mu_{ref,s} = \frac{15\sqrt{\pi m k_{BOLTZ} T_{ref,s}}}{2\pi d_{ref,s}^2 (5 - 2\omega_s)(7 - 2\omega_s)} \tag{3.4}$$

where the variable hard sphere parameters are those used in the DSMC simulations, for nitrogen ω is 0.75 with a reference diameter and temperature of 4.17×10^{-10} m and 273 K, respectively.

The coefficient of thermal conductivity for each internal energy mode is given by Eucken's relation[2],

$$\kappa_{t,s} = \frac{5}{2}\mu_s C v_{t,s} \qquad \kappa_{r,s} = \mu_s C v_{r,s} \qquad \kappa_{v,s} = \mu_s C v_{v,s} \tag{3.5}$$

where c_v is the specific heat at constant volume for each internal energy mode.

The mass diffusion coefficient for each species is replaced by a single coefficient of diffusion using the mixture coefficients of viscosity and thermal conductivity,

$$D = \frac{Le\kappa_{t,r}}{\rho C p_{t,r}} \tag{3.6}$$

where the coefficient of thermal conductivity is the sum of the translational and rotational mode conductivities, c_p is the mixture translational-rotational specific heat at constant pressure, and Le is the Lewis number. The Lewis number is assumed to be a constant in this model. This model is accurate for velocities below 10 km/s[52].

Utilizing the VHS coefficient of viscosity and the coefficient of thermal conductivity from Eucken's relation in LeMANS ensures equivalent treatment for the transport properties in both methods for single species simulations. Given the limit of this model for multi-species flows, a more accurate model is required.

3.2.2 Gupta's Mixing Rule

The use of the VHS coefficient of viscosity in Wilke's mixing rule works well in near equilibrium flows at velocities less than 10 km/s. For multi-species flows, especially when chemical reactions are involved, there is a greater need to try to match the collision-cross sections both methods are utilizing.

For high temperature flows, it is suggested[50, 53] to utilize Gupta's mixing rule[49]. Gupta's mixing rule calculates the transport properties from an approximation to the first-order Chapman-Enskog expression utilizing the collision cross sections. The coefficient of viscosity[53] is calculated using Eq. (3.7).

$$\mu = \sum_s \left(\frac{X_s}{\sum_r \frac{X_r}{M_s} \Delta_{sr}^{(2)}} \right) \tag{3.7}$$

where X_s is the species mole fraction, M_s is the species molecular mass and $\Delta_{sr}^{(2)}$ is a collision term or Gupta-Yos coefficient.

The translational coefficient of thermal conductivity[50] is given by

$$\kappa_t = \frac{15}{4} k_{BOLTZ} \sum_s \left(\frac{X_s}{\sum_r \alpha_{sr} X_r \Delta_{sr}^{(2)}} \right) \tag{3.8}$$

where α_{sr} is given by Eq. (3.9).

$$\alpha_{sr} = 1 + \frac{\left(1 - \frac{M_s}{M_r}\right)\left(0.45 - 2.54\frac{M_s}{M_r}\right)}{\left(1 + \frac{M_s}{M_r}\right)^2} \tag{3.9}$$

The internal energy coefficient of thermal conductivity is given by

$$\kappa_{int} = \sum_s \left(\frac{X_s C p_{s,int}}{\sum_r X_r \Delta_{sr}^{(1)}} \right) \tag{3.10}$$

where c_p is the specific heat at constant pressure for a given internal energy mode

and $\Delta_{sr}^{(1)}$ is another collision term. This equation works for both rotational and vibrational energy modes. The collision terms are defined as

$$\Delta sr^{(1)} = \frac{8}{3}\sqrt{\frac{2m^*}{\pi k_{BOLTZ}T}}\pi\sigma^2\Omega_{sr}^{(1,1)} \tag{3.11}$$

$$\Delta sr^{(2)} = \frac{16}{5}\sqrt{\frac{2m^*}{\pi k_{BOLTZ}T}}\pi\sigma^2\Omega_{sr}^{(2,2)} \tag{3.12}$$

where m^* is the reduced mass, $\sigma^2\Omega_{sr}^{(1,1)}$ is the diffusion collision integral and $\sigma^2\Omega_{sr}^{(2,2)}$ is the viscosity collision integral. The collision integrals utilized in this study can be found in reference[54]. In order to ensure that the transport properties are being handled in the same way in both the DSMC and CFD methods, the viscosity collision integral is utilized to find new VHS parameters for DSMC. A linear regression is performed on the log of the viscosity collision integral verses log of the temperature to calculate the new VHS ω values. The new VHS parameters for all species concerned in this study are given in Appendix A.4

Not only is Gupta's mixing rule more accurate than Wilke's mixing rule, it is also just as numerically efficient[50]. For this reason, Gupta's mixing rule is utilized in multi-species flows for this study. Utilizing the new VHS ω values in DSMC and the collision integrals in Gupta's mixing rule in LeMANS ensures equivalent treatment for the transport properties in both methods for multi-species flows.

3.3   Slip Boundary Conditions

At low Knudsen numbers, the no-slip boundary conditions hold. At higher Knudsen numbers, there are insufficient collisions near the wall and the flow is not able to equilibrate with the wall, hence the no-slip condition is invalidated. The simplest slip boundary condition was introduced by Maxwell[55] for a flat plate. This

slip boundary condition related the slip velocity at the wall to the gradient of the velocity normal to the wall as shown in Eq. (3.13):

$$U_s = A \left(\frac{2 - \sigma}{\sigma} \right) \lambda \frac{\partial u_x}{\partial n} \bigg|_{n=0} \tag{3.13}$$

where U_s is the slip velocity, λ is the mean free path, n is the coordinate normal to the wall, u_x is the velocity tangent to the wall, A is a constant and σ is a momentum accommodation coefficient that varies depending on the surface properties. Maxwell also proposed a temperature jump[56] at the wall as given in Eq. (3.14).

$$T_0 - T_w = \frac{2 - \sigma_T}{\sigma_T} \lambda_T \frac{\partial T}{\partial n} \bigg|_{n=0} \tag{3.14}$$

where $T_0 - T_w$ is the temperature jump, σ_T is a thermal accommodation coefficient and λ_T is an equivalent thermal mean free path. For this study, when utilizing Maxwell's boundary condition, the values of A and both σ values are set to 1 for a fully diffuse thermally accommodating wall. The mean free paths utilized in Maxwell's slip boundary conditions[56] are given in Eq. (3.15)

$$\lambda = \frac{2\mu}{\rho \bar{c}} \qquad \lambda_T = \frac{4}{(\gamma + 1)} \frac{\kappa}{\rho \bar{c} c_v} \tag{3.15}$$

where ρ is the density, $\bar{c}$ is the mean speed, μ is the viscosity, κ is the thermal conductivity and c_p is the specific heat at constant pressure.

The second slip boundary condition utilized for this study is a modification of Maxwell's slip boundary condition. Gökçen[57] found that Maxwell's slip boundary conditions did not agree with free molecular flow at high Knudsen number. Gökçen proposed the general slip boundary conditions; his model specifies the accommodation coefficient as given in Eq. (3.16).

$$\sigma_a \left(a_\lambda - a_w \right) = 2\lambda_a \frac{\partial a}{\partial n} \bigg|_{n=0} \tag{3.16}$$

where a can be either velocity or temperature.

In CFD, the Navier-Stokes equations assume that the shear stress is linearly related to the velocity gradient. At high Knudsen numbers, this linear assumption is incorrect in the Knudsen layer[58], one or two mean free paths away from the surface. This problem is remedied by modifying the viscosity in the Knudsen layer as proposed by Lockerby[55, 59] and shown in Eq. (3.17).

$$\mu = \frac{\mu}{\Psi} \qquad \Psi \left(\frac{n}{\lambda} \right) = 1 + \frac{7}{10} \left(1 + \frac{n}{\lambda} \right)^{-3} \tag{3.17}$$

where n is the distance from the wall and λ is the mean free path. The third boundary condition used is Lockerby's slip boundary condition, which still utilizes Maxwell's slip with the A constant set to $\sqrt{\frac{2}{\pi}}$ and the σ values set to 1 for a fully diffuse thermally accommodating wall. Figure 3.1 gives the velocity slip and temperature jump from CFD and DSMC for a Mach 10 sphere in a flow of nitrogen. From the first figure it can be seen that Lockerby's slip boundary condition gives the best agreement for slip velocity up to 120 degrees on the sphere, but Gökçen's model gives better agreement with DSMC over the aft of the sphere. From Fig. 3.1 (b) it can be seen that there is not one model that compares well with DSMC, but all are better than the no-slip boundary condition.

For more information on slip boundary conditions, please see References [11, 60].

3.4   Thermal Relaxation

In thermal nonequilibrium, the rotational or vibrational temperatures are not equal to the translational temperature. The rotational and vibrational temperatures

(a) Slip Velocity
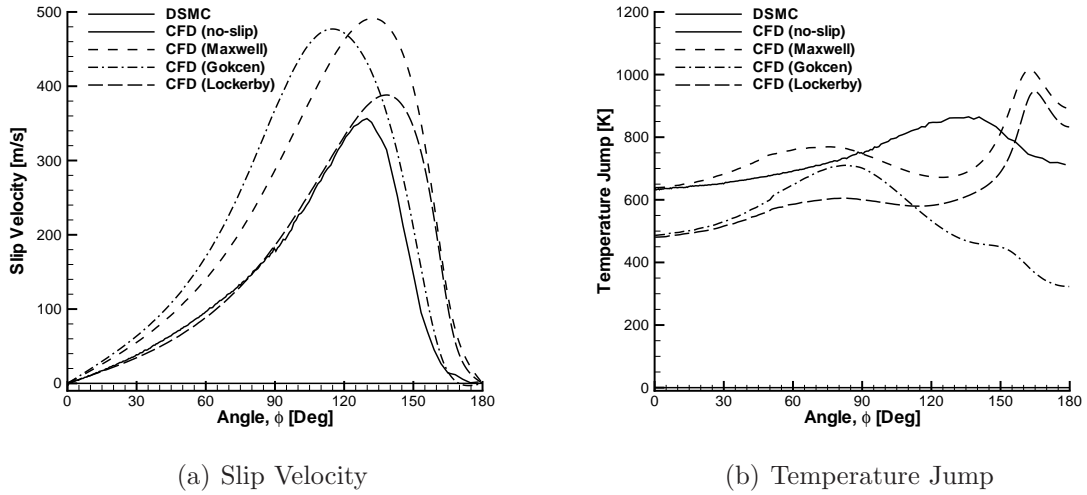
(b) Temperature Jump

Figure 3.1: $Kn_\infty = 0.01$, Slip velocity and temperature jump profiles along the surface of a sphere at Mach 10

are driven towards equilibrium through molecular collisions. The thermal relaxation process can take anywhere from a few collisions, for rotational relaxation, to thousands of collisions, for vibrational relaxation. Thermal nonequilibrium occurs when the relaxation time of the gas is longer than the flow residence time, the time it takes the gas to move past a flow feature, such as a gradient in the temperature or velocity. This can happen when the resident time is short, such as in a shock, or the relaxation time is long, such as in the wake where there are few collisions. In hypersonic flows, thermal nonequilibrium is a common phenomenon. In order to simulate hypersonic flows, the thermal relaxation of a gas needs to be modeled properly. The following sections discuss rotational and vibrational thermal relaxation in both the DSMC and CFD methods.

3.4.1 Rotational Nonequilibrium

Even though LeMANS is capable of modeling thermal nonequilibrium it does so with a two temperature model involving a coupled translational-rotational tem-

perature and a coupled vibrational-electron-electronic temperature. DSMC employs a variable rotational energy exchange probability[61] and therefore simulates rotational relaxation. Since this study is concerned with comparisons between DSMC and CFD for simulations that involve significant amounts of nonequilibrium flow, it is important that the CFD code also has a separate rotational temperature to be able to match DSMC. Not only is it important to include rotational nonequilibrium for comparisons between CFD and DSMC, it is also beneficial to have a separate rotational energy equation that can provide more accurate results in hypersonic flows where thermal nonequilibrium is common. The rotational energy equation per unit volume is given by Eq. (3.18)

$$\frac{\partial E_r}{\partial t} + \nabla \cdot (E_r \vec{u}) = -\nabla \cdot (\vec{q_r}) - \nabla \cdot \sum_s (\rho_s e_{rs} \vec{u}_{ds}) + \dot{w}_r \qquad (3.18)$$

where q_r is the rotational heat flux given by Fourier's law, u_{ds} is the species diffusion given by Fick's law, and $\dot{w}_r$ is a source term given by Eq. (3.19).

$$\dot{w}_r = \sum_s \left(Q_{rs}^{t-r} + \dot{w}_s e_{rs} \right) \qquad (3.19)$$

Equation (3.19) is composed of two parts, the first being the rotational energy relaxation given in Eq. (3.20) and the second part is the gain and loss of rotational energy due to chemical reactions, which is discussed in more detail in section 3.5.3.

$$Q_{rs}^{t-r} = \rho_s \frac{e_{rs}^* - e_{rs}}{Z_{rs} \tau_c} \qquad (3.20)$$

The rotational energy relaxation is modeled using a Landau-Teller model, where e_{rs}^* is the rotational energy evaluated at the translational temperature, Z_{rs} and τ_c together give the rotational relaxation time. Z_{rs} is the rotational collision number

given in Eq. (3.21) derived by Parker[62]. τ_c is the mean collision time from the VHS model. Equation (3.22) gives the mean collision frequency, given by Bird[3], which is the inverse of the mean collision time,

$$Z_{rs} = \frac{Z_{rs}^{\infty}}{1 + \frac{\pi^{\frac{3}{2}}}{2}\left(\frac{T_s^*}{T}\right)^{\frac{1}{2}} + \left(\frac{\pi^2}{4} + \pi\right)\left(\frac{T_s^*}{T}\right)} \tag{3.21}$$

$$\nu_s = \sum_i \left(n_i (d_{ref})_i^2 \left(\frac{8\pi k_{BOLTZ}(T_{ref})_i}{m_i^*}\right)^{\frac{1}{2}} \left(\frac{T}{(T_{ref})_i}\right)^{1-\omega_i}\right) \tag{3.22}$$

where Z_{rs}^{∞} and T^* are constants for a given species, and the VHS parameters are the same ones used in DSMC and the CFD viscosity model given in section 3.2.1. The values of the Z_{rs}^{∞} and T^* constants for each species are given in Appendix A.1

A heat bath of nitrogen is simulated to compare the rotational relaxation process in DSMC, CFD and from theory. The theory comes from a simple numerical integration of the rotational energy relaxation equation as given in Eq. (3.20). The heat bath is started with a translational temperature of 15,000 K while rotational temperature is started at 10,000 K. There is very good agreement between DSMC and CFD as compared to theory, as seen in Fig. 3.2.

From this heat bath test case it is clear that CFD with a separate rotational energy equation is in very good agreement with the DSMC method, ensuring that rotational relaxation is handled in the same manner in both the CFD and DSMC methods.

3.4.2 Vibrational Relaxation

There are two models for the exchange of vibrational and translational energy in DSMC, the first is a phenomenological model as described by Boyd[63]. The probability of an inelastic collision where vibrational energy is exchanged with transla-
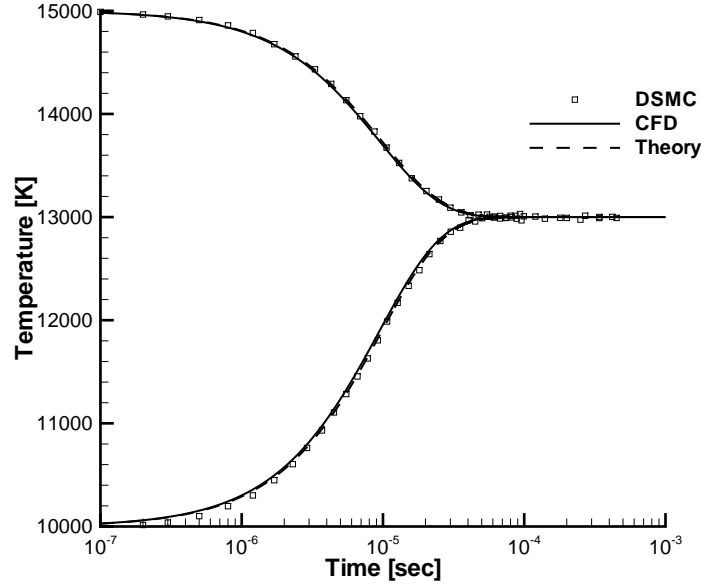
Figure 3.2: Comparison of rotational relaxation as predicted by DSMC and CFD in nitrogen; the solid line is translational temperature and the dashed line is rotational temperature

tional energy is proportional to the inverse of the vibrational relaxation time. This probability is the average over the instantaneous probabilities as shown in Eq. (3.23)

$$P = \frac{1}{\tau_v \nu} = \int_0^\infty \phi(g) f(g) \, dg \qquad (3.23)$$

where $\phi(g)$ is the instantaneous probability for a given relative velocity and $f(g)$ is the relative velocity distribution function.

To approximate the vibrational relaxation time, a Landau-Teller model is utilized with correlated experimental data from Millikan and White[64], as expressed in Eq. (3.24).

$$\tau_{LT} = \frac{1}{p} exp\left[A\left(T^{-\frac{1}{3}} - B\right) - 18.42\right] \qquad (3.24)$$

where the pressure is in atm. For this study, the values of A and B come from

Park[65] for both DSMC and CFD. To be able to utilize the above model, a modified Landau-Teller form is found, as shown in Eq. (3.25)

$$\phi_{LT} = \frac{1}{Z_0} g^\alpha \exp\left(\frac{-g^*}{g}\right) \tag{3.25}$$

where the constants are found to satisfy Eq. (3.23). Unfortunately this integral cannot be evaluated analytically so the method of steepest descent is employed. For high temperatures, which are often encountered in hypersonic flows, a correction proposed by Park[66] is used as shown in Eq. (3.26).

$$\tau_P = \frac{1}{n\bar{c}\sigma} \tag{3.26}$$

where σ is the collision cross section, $\bar{c}$ is the mean thermal speed and n is the number density. An instantaneous probability for Park's correction can be derived in a similar manner as done for the Landau-Teller model. The total vibrational relaxation time is the sum of the Landau-Teller and Park relaxation times. The total instantaneous probability is given by Eq. (3.27).

$$\phi(g) = \frac{\phi_{LT}\phi_P}{\phi_{LT} + \phi_P} \tag{3.27}$$

A factor was proposed by Lumpkin et al. to correct the DSMC relaxation time[67]. Although this was done for rotational relaxation, it must also be applied to vibrational relaxation, as shown in Eq. (3.28).

$$\tau_{part} = \frac{\tau_{cont}}{1 + \frac{\zeta}{4-2\omega}} \tag{3.28}$$

When the instantaneous probability is integrated over all collisions, it should match the average probability calculated from theory; however, it was found in a

previous study[68] that they do not match. It is thought that the probabilities do not match due to the method of steepest descent required to find the instantaneous probability. It has been found that the probability can better correspond with theory by multiplying by a simple factor that is dependent on the maximum temperature[12]. Table 3.1 gives the probablity from DSMC along with that calculated from theory[68]. It also gives the factor that should be used at a given maximum temperature. For this study, the maximum temperatures for the Mach 10 and 25 cases are approximately 5,000 K and 25,000 K, respectively. The corresponding factors in Table 3.1 are utilized in the DSMC simulations. For the Mach 45 case the maximum temperature is approximately 90,000 K, which is off the table. However, the factor tends to unity as the temperature climbs; so a factor of one is used for the Mach 45 case.

Table 3.1: Vibrational probabilities for $N_2 - N_2$ collisions in DSMC compared to theory

Temperature [K]	DSMC	Theory	Factor
5,000	1.57×10^{-4}	1.24×10^{-4}	0.79
10,000	1.71×10^{-3}	2.44×10^{-3}	1.43
25,000	9.00×10^{-3}	1.23×10^{-3}	1.70
30,000	1.08×10^{-2}	1.72×10^{-2}	1.59
40,000	1.38×10^{-2}	1.95×10^{-2}	1.41
50,000	1.61×10^{-2}	2.10×10^{-2}	1.30

Unfortunately, this method does not work for multiple species, and in fact was only employed for N_2-N_2 vibrational relaxation[12, 69]. For multiple species, a more elegant solution has been included in the DSMC method to be able to obtain the proper vibrational relaxation rate. The problem of having to calculate the instantaneous probability for every collision can be avoided by simply calculating the vibrational relaxation time for each collision class for each cell as discussed by Deschenes

et al.[70]. The probability for each collision class and each cell can then be calculated using Eq. (3.23). The vibrational relaxation time can be calculated by using the Milliken-White model, Eq.(3.24), and Park, Eq. (3.26). A factor proposed by Gimelshein et al.[71] is needed to be able to utilize this relaxation time in a particle simulation as shown in Eq. (3.29)

$$\tau_{part} = \frac{\tau_{cont}}{1 + \frac{0.5\,\zeta^2 exp\left(\frac{\theta_v}{T}\right)}{4-2\omega}} \tag{3.29}$$

This equation can be employed as long as the vibrational temperature is less than the translational temperature, which is the case for hypersonic flows. Note that it also works if the vibrational temperature is slightly greater than the translational temperature, which is the case in expansion flows such as in the wake.

This model in DSMC was shown by Deschenes et al. to match the vibrational relaxation in CFD for nitrogen[70]. Since this model has only been tested with one species, a heat bath of 5 species air is run with the cell based model and the phenomenological model in DSMC and compared to CFD. The heat bath is started with a translational temperature of 15,000 K while rotational and vibrational temperatures are started at 10,000 K. From the results of this test, which are displayed in Fig. 3.3, it can be seen that the cell based method is in better agreement with CFD than the variable vibration probability.

The changes made to the CFD method, a separate rotational energy equation, and the DSMC method, cell based vibrational relaxation model, ensure that thermal relaxation is dealt with in a similar way in both techniques. In this way the, differences seen between the two codes are not caused by the thermal relaxation models in the two methods.
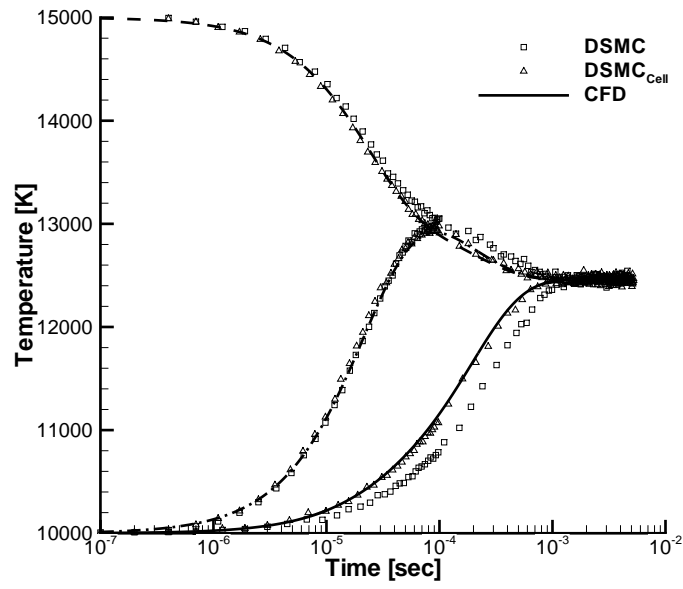
Figure 3.3: Comparison of thermal relaxation process as predicted by DSMC and CFD in 5 species air; the dashed line is translational temperature, the dot-dash line is rotational temperature and the solid line is vibrational temperature

3.5 Chemistry Models

In hypersonic flows, it is common to have reacting flow around the reentry vehicle. Part of this study is concerned with simulations of a reentry flow in 5-species reacting air. So, it is important to make sure that the reaction rates calculated in the CFD and DSMC methods are evaluated in a similar manner. This is done to ensure the differences seen between the two codes are not due to different reaction rates. The following sections highlight differences in how chemical reacting flow is handled in the two methods and what is done to make both numerical methods behave in a similar manner.

3.5.1 Chemical Equilibrium

One of the major differences between the CFD and DSMC methods is how chemical equilibrium is handled. So, the first step is making sure the forward and backward reaction rates, and hence the equilibrium constant, are all calculated in a similar manner. First, one needs to understand what happens in the DSMC method.

In the DSMC method, a collision pair is selected and the probability of reaction is compared to a random number. If the probability is greater than the random number then a reaction occurs. Once a reaction occurs, a Borgnakke-Larsen model is applied to be able to distribute the energy to the available energy modes. There are two models available in MONACO for chemistry; the total collision energy (TCE) model and the vibrationally favored dissociation (VFD) model[72]. The VFD model is employed in the DSMC method for this study, and a qualitatively similar model is used in the CFD method, as discussed in more detail in a later section. For both the TCE and VFD models, the reaction rate, forward or backward, must be specified in modified Arrhenius form. The probability of reaction is found by integration of the

equilibrium Boltzmann distribution function as shown in Eq. (3.30).

$$k_f(T) = a_f T^{\eta_f} \exp\left(\frac{-\varepsilon_f}{k_{BOLTZ}T}\right) =$$
$$\langle\sigma g\rangle \int_{\varepsilon_f}^{\infty} P_c(\varepsilon_c) \int_{\varepsilon_v=0}^{\infty} P_v(\varepsilon_v) f_B(\varepsilon_v) f_B(\varepsilon_c - \varepsilon_v)\, d\varepsilon_v\, d\varepsilon_c \quad (3.30)$$

where f_B is the equilibrium Boltzmann distribution for energy. Since the reaction rate has the modified Arrhenius form, the reaction probability for the VFD model is found to be

$$P_{VFD} = A \left(\frac{\varepsilon_v}{\varepsilon_c}\right)^{\phi} \frac{(\varepsilon_c - \varepsilon_f)^{\psi}}{(\varepsilon_c)^{\chi}} \quad (3.31)$$

where A is a complicated constant not reproduced here, ϕ is a constant dependent upon the species[73], $\psi = \eta + 0.5 + \zeta$ and $\chi = 1 + \zeta - \omega$. If ϕ is set to zero, the total collision energy model is recovered from the VFD model.

In order to have backward reactions in the VFD model, the rate coefficient must be in the modified Arrhenius form. The backward rates are calculated using the forward rates and the equilibrium constant, as shown in Eq. (3.32).

$$k_b(T) = \frac{k_f(T)}{K_e(T)} = a_b T^{\eta_b} \exp\left(\frac{-\varepsilon_b}{k_{BOLTZ}T}\right) \quad (3.32)$$

Typically in the DSMC method, the backward rates are fit to a modified Arrhenius form over a specified temperature range[74]. This can cause problems if a simulation goes outside this temperature range and all the fits need to be re-done. With the growth of interest in hybrid methods, it is necessary for the DSMC method to match the CFD method; it is also important for this study. It is common in the CFD method to use a line fit proposed by Park[66] to find the equilibrium constant, as

given in Eq. (3.33). This equilibrium constant is then applied to find the backward reaction rate.

$$K_e(T) = \left[A_1 \left(\frac{T}{10000} \right) + A_2 + A_3 \ln \left(\frac{10000}{T} \right) + \right.$$
$$\left. A_4 \left(\frac{10000}{T} \right) + A_5 \left(\frac{10000}{T} \right)^2 \right] \quad (3.33)$$

The constants, A_i, are weakly dependent on the number density as given by Park[66]. The constants are found using an interpolation method if the number density is within the range of the data. If the number density falls outside of that range, the constants at the highest or lowest points are used accordingly. For DSMC, instead of performing a fit over a limited temperature range, it would be desirable to evaluate the equilibrium constant, and then calculate the backwards reaction rates. This can be done by a method suggested by Boyd[72], that utilizes the equilibrium constant and maintains the modified Arrhenius form required by the DSMC chemistry model. The backward reaction rate is found by taking the forward reaction rate, Eq. (3.30), and substituting into Eq. (3.32), since $\eta_b = \eta_f$ one can solve for the backward rate constant as shown in Eq. (3.34).

$$a_b = \frac{a_f}{K_e(T)} \exp \left(\frac{-\varepsilon_f}{k_{BOLTZ} T} \right) \quad (3.34)$$

This can now be substituted into the modified Arrhenius form and the probability for the backwards reaction can be found in the same way as described for the forward reaction. In this method, the forward and backward reaction rates are calculated in a similar manner, despite the vast differences in the way the chemical reactions are handled in the two numerical methods.

3.5.2 Three-Temperature Model

In the previous section, the methods for calculating the forward and backward rates were given, and these rates are utilized in both CFD and DSMC methods. The temperature that is utilized in the CFD calculations is Park's two-temperature model[66], given in Eq. (3.35).

$$T_P = T_{tr}^a T_{ve}^b \tag{3.35}$$

where a and b are constants that must sum to 1, T_{tr} is the the translation-rotational temperature and T_{ve} is the vibrational-electron-electronic temperature. The reaction rates are affected by the level of nonequilibrium present in the flow; the two-temperature model is attempting to include the affects of nonequilibrium. By including the vibrational temperature, this model aims to account for the fact that vibrationally excited particles are more likely to dissociate. Values for a and b can vary, but there are two typical sets used: $a = b = 0.5$ or $a = 0.7$ and $b = 0.3$. Usually, a varies between 0.5 and 0.7[75], however these numbers vary wildly with a as low as 0.3[9].

For the backward reaction rate, and hence the equilibrium constant, the temperature utilized is the translation-rotational temperature, therefore $a = 1$ while $b = 0$. This is the same for exchange reactions. The temperature utilized for impact ionization reaction rates is the vibrational-electron-electronic temperature, or $a = 0$ while $b = 1$.

Since there is now a separate rotational temperature, see section 3.4.1, it has to be included in the evaluation of the reaction rates. There can be rotational thermal nonequilibrium, therefore the temperature employed in the rate calculation is now

composed of three temperatures. The need for a so called three-temperature model is now being recognized as a necessity in chemistry modeling by Park[75]. In this work, a phenomenological temperature model is created based on the two-temperature model,

$$T_P = T_t^a T_r^b T_{ve}^c \qquad (3.36)$$

where the a, b and c values again must sum to 1, T_t is the translational temperature, T_r is the rotational temperature and T_{ve} is the vibrational-electron-electronic temperature. Since this is a phenomenological model, there is no way of finding new constants. There has been research on finding the reaction rates that work best with the two-temperature model[76, 65, 77]. This work cannot produce reaction rates that best match this temperature model, so a method of employing the degrees of freedom is devised. Starting with the typical values from the two-temperature model of 0.5 for both a and b, the same emphasis on the vibrational temperature is retained, so c is kept at 0.5. The remaining 0.5 is split over translational and rotational temperatures by the number of degrees of freedom, doing a simple calculation the value of a is set to 0.3 and b is set to 0.2.

For the backwards and exchange reactions, the same method is utilized. The temperature utilized for these reactions is the translational temperature,as a result c and b is set to 0. As a result, the value for a is set to 1.0. Utilizing this model puts a higher emphasis on molecules with higher vibrational and rotational temperatures, allowing the CFD method to include nonequilibrium effects on the reaction rates. It should be noted that when the flow is in rotational equilibrium, this phenomenological three-temperature model reduces to the two-temperature model. All the values for the three-temperature model utilized in this study are given in Appendix A.2.

3.5.3 Preferential Dissociation

In a further attempt to have the CFD method behave more like the DSMC method with the VFD model, a preferential dissociation model is also included in the CFD method. Without the preferential model it is assumed that the molecules are destroyed or created at the average vibrational energy of the cell. In the preferential model, it is assumed that the molecules are destroyed or created at a higher vibrational energy. This preferential dissociation model is implemented in the source term for the vibrational energy equation, the source term is given in Eq. (3.37).

$$S = \dot{\omega}_s \left(\alpha_s D_s \right) \tag{3.37}$$

where D_s is the dissociation potential for a given species, $\dot{\omega}_s$ is the species conservation source term and α_s is the fraction of the dissociation potential that is due to vibrational energy. The α_s value is usually set to 0.3. While this model is typically only applied to vibrational preferential dissociation, in this work it is also applied to rotational preferential dissociation. To be able to have the preferential dissociation model in the CFD method match the DSMC method with the VFD model, data from the DSMC method is utilized to find new α_s values. The amount of rotational and vibrational energy lost per reaction is found in the DSMC method. The α_s values found using the DSMC method are given in Fig. 3.4.

From this figure it can be seen that at lower temperatures, between 10,000 and 15,000 K, the α_s is around 0.3, making the original assumption fairly accurate. However, the values grow higher as the temperature rises. In the figure, line fits to the DSMC data are also given. These line fits are given in Eqs. (3.38 - 3.40).

(a) Rotational   (b) Vibrational
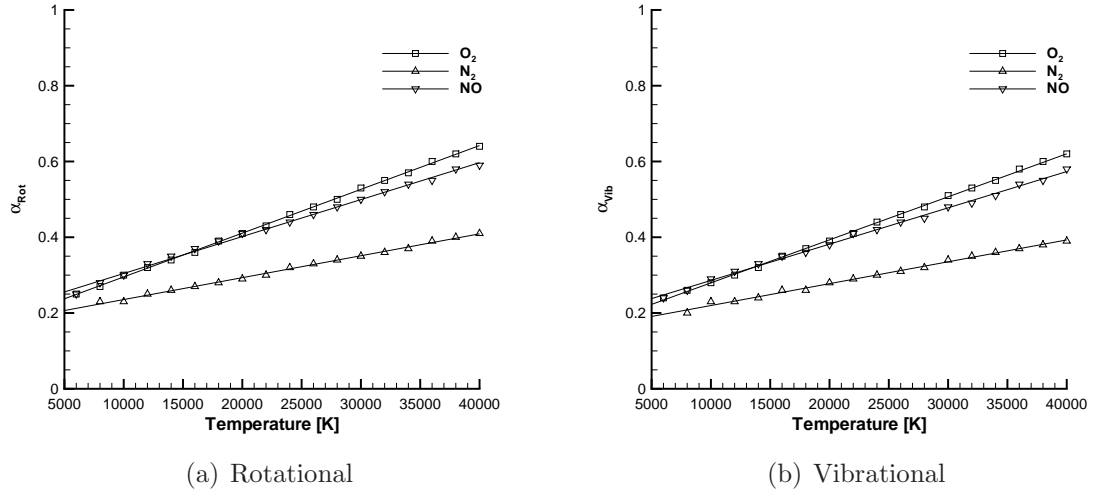
Figure 3.4: Preferential Dissociation Parameter α as a Function of Temperature; symbols are data from DSMC method and lines represent the line fits utilized

$$\alpha_{r,N_2} = 5.784 \times 10^{-6}T + 0.178 \quad \alpha_{v,N_2} = 5.772 \times 10^{-6}T + 0.162 \tag{3.38}$$

$$\alpha_{r,O_2} = 1.156 \times 10^{-5}T + 0.179 \quad \alpha_{v,O_2} = 1.136 \times 10^{-5}T + 0.166 \tag{3.39}$$

$$\alpha_{r,NO} = 9.752 \times 10^{-6}T + 0.207 \quad \alpha_{v,NO} = 9.582 \times 10^{-5}T + 0.190 \tag{3.40}$$

These equations are implemented into the CFD method to better match the VFD model in the DSMC method. These modifications to both numerical methods are meant to ensure that the differences seen in the results are not caused by differences in the chemistry models. In order to make this assertion, these models need to be tested.

To test these models, a heat bath simulation is performed. It should be noted that the reaction rates utilized in this study can be found in references[78, 79], they

(a) Species Mole Fractions

(b) Temperatures
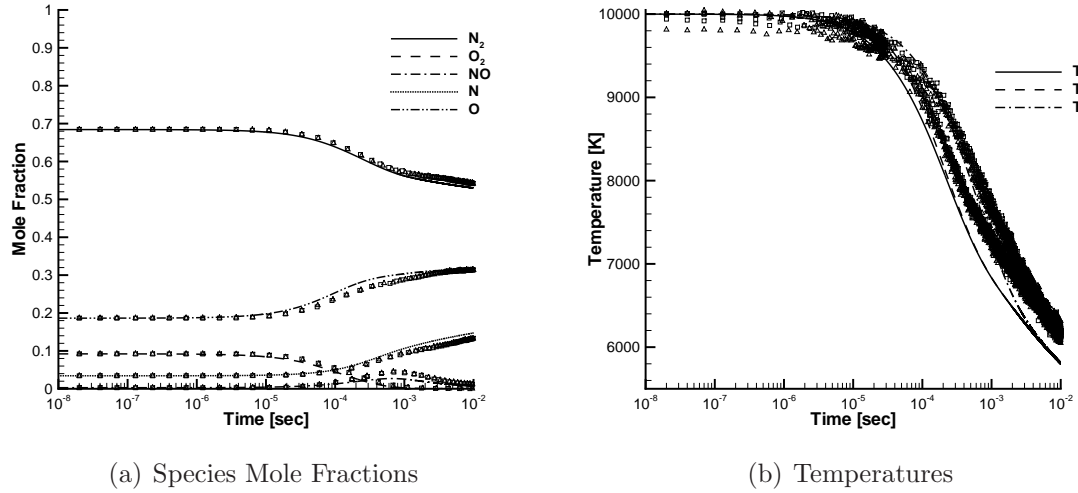
Figure 3.5: Comparison of Chemical Reaction Process as Predicted by DSMC and CFD in Air; Triangles Represent DSMC with Park's Equilibrium, Squares Represent DSMC and Lines Represent CFD

are also given in Appendix A.3. The test case is with air starting at a temperature of 15,000 K. The results of these test cases are given in Fig. 3.5.

The figure gives the mole fraction and temperature profiles over time for DSMC, the original model and the new equilibrium model, and CFD. From the first figure it can be seen that both DSMC models compare very well with each other and CFD for a 5 species air model. The largest difference is observed to occur in nitric oxide, where the peak difference is approximately 10 percent between CFD and DSMC. The temperature profiles from the air heat bath test case are given in Fig. 3.5(b). From this figure it is seen that the two methods predict similar temperature profiles, the maximum error is approximately 10 percent between CFD and DSMC. It should be noted that there is less than 1 percent difference between the two DSMC implementations.

From the profiles of mole fraction and temperature it is clear there are still differences between CFD and DSMC. Even though this is a heat bath test case there is still

(a) Vibration   (b) Rotation
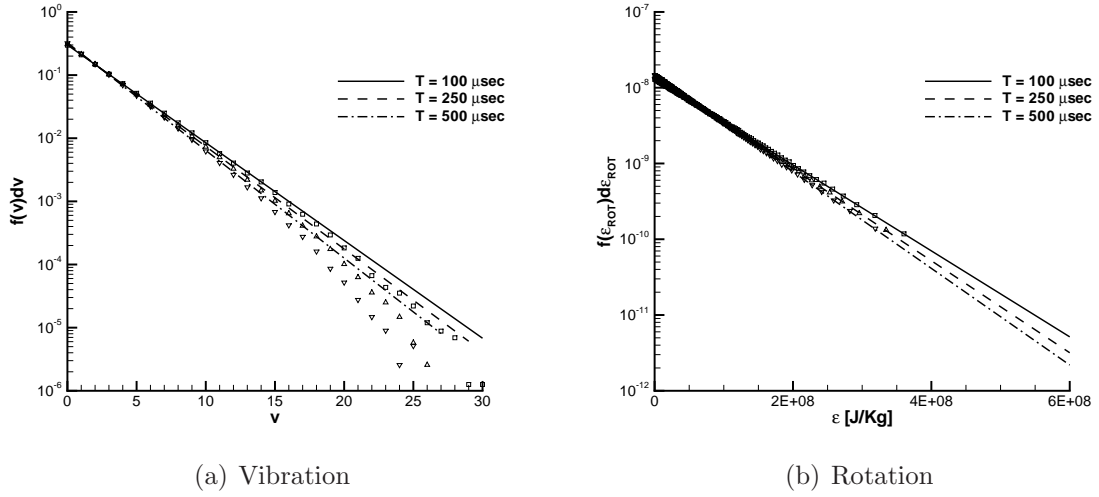
Figure 3.6: Vibrational and Rotational Probability Distribution Functions; Symbols Represent Particle Data while Lines Represent Equilibrium Boltzmann's Distribution

significant vibrational nonequilibrium as can be seen in Fig. 3.6(a), this figure gives the distribution function along with an equilibrium Boltzmann distribution. The vibrational nonequilibrium is caused by chemical reactions depleting higher vibrational energy states faster than vibrational relaxation can equilibrate the vibrational distribution. Notice that the same behavior is not true for rotational energy, because rotational relaxation is faster than chemical reactions. Since the vibrational distribution function has a direct impact on the reaction rates, see Eq. (3.30), this nonequilibrium is the cause of the differences seen in the previous heat bath results. Since the CFD method is not able to simulate this vibrational nonequilibrium it will not be able to match the reaction rates calculated in the DSMC methods. A discussion of how this affects the surface properties on a hypersonic vehicle is included in Chapter V.

CHAPTER IV

Analysis of Non-Reacting Nitrogen Flow

4.1   Introduction

This chapter discusses the effects of continuum breakdown over a blunt hypersonic configuration, a 12 inch sphere. Since previous studies have looked at monatomic gases, such as argon, this study will examine diatomic gases, such as nitrogen. This adds the complexity of thermal nonequilibrium. The temperatures present in these cases are high enough for dissociation to occur. However, only thermal nonequilibrium effects are included in this study. Chemistry effects are considered in the next chapter.

This study examines the continuum breakdown phenomenon in flows of nitrogen
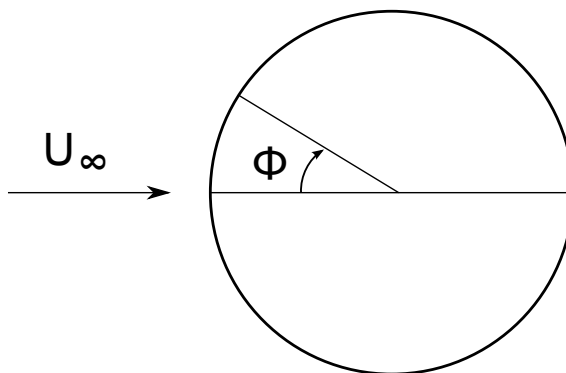
Figure 4.1: Sphere geometry definition

over a 12 inch diameter sphere, as shown in Fig 4.1, at Mach numbers of 10, 25 and 45. The free stream temperature is 200 K giving free stream velocities of 2,884 m/s, 7,209 m/s and 12,976 m/s for the three different Mach numbers. The surface of the sphere has fixed temperatures of 500 K, 1,500 K and 2,500 K for the Mach 10, 25 and 45 cases, respectively. The density of the free stream is varied to change the global Knudsen number of the flow as given in Table 4.1. The Knudsen number is calculated using the sphere diameter as the characteristic length and the hard sphere model to calculate the mean free path,

$$\lambda = \frac{1}{\sqrt{2}\pi d^2 n} \tag{4.1}$$

where d is the diameter of the molecule and n is the number density. From Table 4.1 it is seen that the global Knudsen number varies from 0.002 to 0.25; giving a range of flow regimes from continuum to rarefied gas flow.

Table 4.1: Simulated nitrogen flow regimes

Kn_∞	Mass Density (kg/m^3)	Number Density $(particles/m^3)$	Mean Free Path (m)
0.002	9.875×10^{-5}	2.124×10^{21}	6.096×10^{-4}
0.01	1.975×10^{-5}	4.247×10^{20}	3.048×10^{-3}
0.05	3.949×10^{-6}	8.494×10^{19}	1.524×10^{-2}
0.25	7.899×10^{-7}	1.699×10^{19}	7.620×10^{-2}

The simulations are performed using two different computational methods. First, the Navier-Stokes equations are numerically solved using the LeMANS CFD code. A grid convergence study is conducted on all cases to determine the final grid for each case. Second, the DSMC solutions are provided by the MONACO code. All DSMC meshes are adapted by hand so that the cell size in the final mesh is of the order of

a mean free path.

The results that are presented for the surface aerothermodynamic properties are given as non-dimensionalized coefficients which are defined by Eqs. (4.2 - 4.4).

$$C_p = \frac{p - p_\infty}{\frac{1}{2}\rho_\infty U_\infty^2} \tag{4.2}$$

$$C_\tau = \frac{\tau}{\frac{1}{2}\rho_\infty U_\infty^2} \tag{4.3}$$

$$C_q = \frac{q}{\frac{1}{2}\rho_\infty U_\infty^3} \tag{4.4}$$

where ∞ indicates free stream conditions. The surface aerothermodynamic properties are plotted against the surface angle ϕ, which is measured from the stagnation point, as shown in Fig 4.1. For each case, the CFD results are presented with and without slip boundary conditions. As discussed in Chapter III, there are several slip boundary condition models in the CFD method; for this study, the Göçken slip boundary condition model is employed. Along with the other surface properties, the gradient length local Knudsen number is also provided on the right axis. This gives the ability to determine where continuum breakdown is occurring on the surface and highlights the effects breakdown has on surface properties.

This chapter also contains a discussion of results from the rotational energy equation included in the CFD method, to determine the accuracy of the rotational relaxation model. A comparison is made of the results from the sphere and cylinder simulations, to determine the effects of running simulations axisymmetrically as compared to the two dimensional case.

4.2 Rotational Nonequilibrium

To test the validity of the CFD rotational energy model, the temperature profiles from CFD and DSMC along the stagnation stream line are compared in Fig. 4.2 for several different flow conditions. Also included in these figures is the maximum gradient length local Knudsen number based on the DSMC simulation. This will give an idea of the amount of breakdown in the flow, but also gives a good approximate location of the shock. For the Mach 10 Knudsen number 0.002 case, the shock is very clearly defined by Kn_{GLL}, and it can be seen that the translational temperature, shown as solid lines, predicted by DSMC starts increasing further upstream due to the fact that the shock predicted by DSMC is thicker, as expected. However, the translational temperature from CFD quickly matches the temperature from DSMC although it does not capture the peak. It can be seen that there is rotational nonequilibrium behind the shock for both DSMC and CFD, but both rotational temperatures, shown as dashed lines, nearly overlap each other along the stagnation streamline. For the Mach 10 Knudsen number 0.01 case, the shock is not as clearly defined and Kn_{GLL} is greater than the 0.05 limit from the shock all the way to the wall, indicating continuum breakdown has occurred. In this case, the difference in the shock thickness is much more noticeable. There is rotational nonequilibrium behind the shock for both CFD and DSMC, and again the difference in shock thickness leads to a difference in the rotational temperatures. However, the rotational temperature predicted by CFD catches and overshoots the DSMC rotational temperature post shock and eventually all temperatures equilibrate. This discrepancy can be explained by the fact that the flow is in nonequilibrium following the shock, which is verified by looking at probability distribution functions at various

points along the stagnation streamline. At the point where the CFD temperatures overshoot the DSMC temperatures there is still a bimodal distribution indicating that the flow is nonequilibrium. The distribution functions for the Mach 10 case are not included here, but in the discussion regarding the Mach 25 case, distribution functions are included.

Figures 4.2(c) and (d) give the temperature profiles for Mach 25 and 45 at a global Knudsen number of 0.01. At these higher Mach numbers, the simulations now include vibrational as well as rotational nonequilibrium. The Mach 25 case is similar to the Mach 10 case in that there is breakdown in the flow from the front of the shock all the way to the wall of the sphere. The difference in the shock thickness is again visible in the temperature profiles for DSMC and CFD. The vibrational temperature, shown as dotted lines, and the rotational temperature as predicted by CFD both overshoot their DSMC counterparts. However, all temperatures for both DSMC and CFD fall back into equilibrium at approximately the same point. For the Mach 45 case, the slight over prediction by CFD for all the temperatures still exists, but again all three temperatures reach equilibrium at the same point. Since the Mach number is so high in this case, the point at which equilibrium is reached is pushed close to the wall of the sphere.

4.2.1 Comparison of Probability Distribution Functions

The differences seen in the above cases can be explained by nonequilibrium in the flow. Particle data is extracted from the Mach 25, global Knudsen number 0.01, DSMC simulation at four different locations: in front of the shock, in the shock, right behind the shock and the point where CFD overshoots the DSMC rotational and vibrational temperatures. From the particle data, the probability distribution
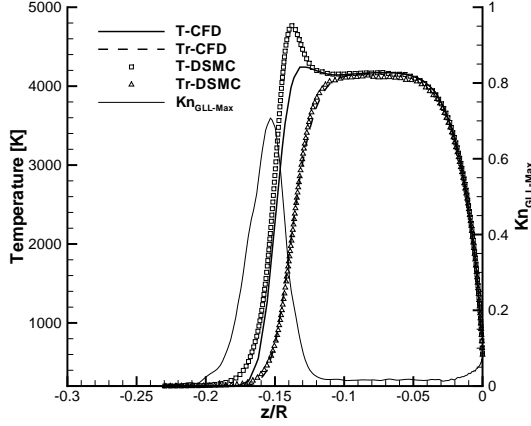
(a) Mach 10, $Kn_\infty = 0.002$
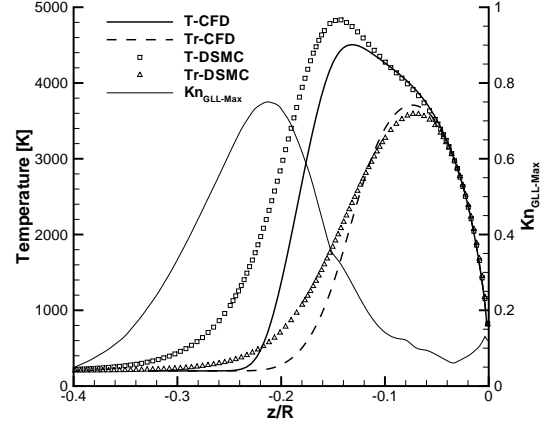
(b) Mach 10, $Kn_\infty = 0.01$
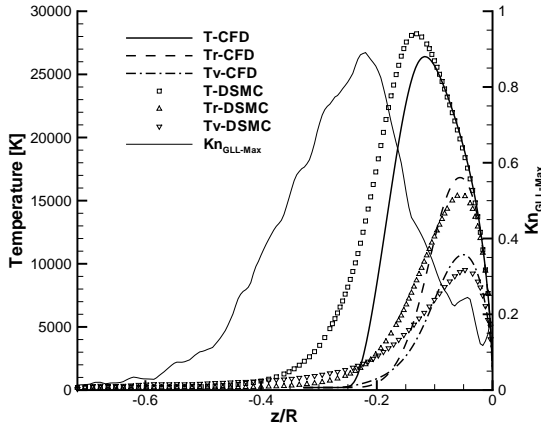
(c) Mach 25, $Kn_\infty = 0.01$
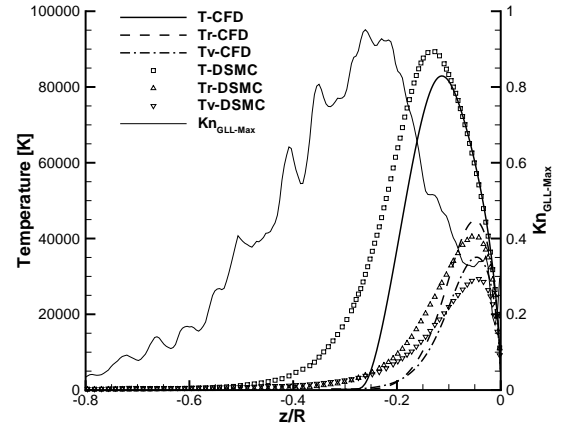
(d) Mach 45, $Kn_\infty = 0.01$

Figure 4.2: Temperature profiles along the stagnation streamline. The maximum Kn_{GLL} is plotted on the right axis. Flow is from left to right; distance is normalized by the radius of the sphere.

functions can be found. The probability distribution functions are computed by placing particles in bins; usually this is accomplished by specifying how many bins are desired and then sorting the particles into the bins. In this study, a different approach is utilized, where the number of particles per bin is specified and the width of the bin is variable[80]. The probability is the number of particles in the bin over the width of the bin and normalized by the total number of particles, as given in Eq (4.5)

$$f\left(x\right)dx = \frac{1}{n}\frac{No.\,of\,X_i\,in\,same\,bin\,as\,x}{Width\,of\,bin\,containing\,x}\,dx \tag{4.5}$$

where n is the total number of particles, the numerator is the number of particles in the bin, and the denominator is the width of the bin.

To make comparisons to CFD, the particle velocity distributions are compared to the Chapman-Enskog distribution, discussed in chapter II. To find the Chapman-Enskog distribution for a given direction, the integral over the two remaining directions must be performed. For instance, if one wants the Chapman-Enskog distribution in the x-direction, the integral over all space in the y- and z-directions must be performed. This processes can be easily accomplished using standard integrals [2], and the result for the x- direction is given in Eq. (4.6).

$$\Gamma_x = 1 + \frac{2}{5}\hat{q}_x\left(\hat{C}_x^3 + \hat{C}_x\right) - \hat{q}_x\hat{C}_x + \hat{\tau}_{x,x}\left(\frac{1}{2} - \hat{C}_x^2\right) \tag{4.6}$$

It is the same for the y-direction, substituting in variables for the y-direction. The z-direction of the Chapman-Enskog distribution is slightly different from the others. The distribution in the z-direction is given in Eq. (4.7).

$$\Gamma_z = 1 + \frac{2}{5}\hat{q}_z\left(\hat{C}_z^3 + \hat{C}_z\right) - \hat{q}_z\hat{C}_z + \left(\hat{C}_z^2 - \frac{1}{2}\right)(\hat{\tau}_{x,x} + \hat{\tau}_{y,y}) \qquad (4.7)$$

where $\hat{q}$ is the normalized heat transfer, $\hat{C}$ is the normalized thermal velocity and $\hat{\tau}$ is the normalized shear stress. The thermal velocity is normalized by the most probable speed, $(2k_{BOLTZ}T/m)^{0.5}$. The normalized heat transfer and shear stress can be found from moments of the particle data[22], as given in Eq. (4.8).

$$\hat{\tau}_{i,j} = \frac{2}{3}\overline{\hat{C}^2}\delta_{i,j} - 2\overline{\hat{C}_i\hat{C}_j} \qquad \hat{q} = 2\overline{\hat{C}_i\hat{C}_j} \qquad (4.8)$$

The velocity probability distribution functions for the particle data and for Chapman-Enskog are given in Fig. 4.3. It should be noted that the y and z velocity probability distribution functions are exactly the same, so only the z component is shown. This is due to the data coming from near the axis in an axisymmetric simulation. The first plot, Fig. 4.3(a), gives the velocity probability distribution functions in the free stream where the flow is expected to be in equilibrium. It can be seen that there is good agreement between the particle data and Maxwellian distribution. Figure 4.3(b) gives the velocity probability distribution function in the shock where two peaks can be observed. The higher peak contains the particles that have equilibrated to the post-shock condition and the lower peak contains the particles at the pre-shock condition. This is not a surprising observation given that the flow is in the shock, where nonequilibrium is expected. The third plot, Fig. 4.3(c), gives the velocity probability distribution function shortly after the shock. Not surprisingly, the distribution shows a double peak, proving the existence of the expected nonequilibrium flow. The fourth plot, Fig. 4.3(d), shows the velocity probability distribution function agreeing well with the Chapman-Enskog distribution. This indicates the flow is actually in equilibrium at this point. This raises the question as to what has caused the tem-

perature overshoots that are seen in the rotational and vibrational temperatures. To find the answer to this question, the distribution function of the rotational energy is inspected at the same four points in the flow.

There is not a Chapman-Enskog distribution for internal energy, so the Boltzmann distribution is utilized instead. The Boltzmann distribution[2] for all internal energies is given below:

$$\frac{N_j^*}{N} = \frac{g_j \, exp\left(-\frac{e_j}{K_{BOLTZ}T}\right)}{Q} \tag{4.9}$$

where e_j is an internal energy, T is the temperature associated with the internal energy, g_j is the degeneracy and Q is the partition function of that internal energy. This can be utilized to obtain the Boltzmann distribution for either rotational or vibrational energy. It should be noted that the rotational energy utilizes a continuos version of the Boltzmann distribution, given by Lumpkin et al.[67].

The rotational energy probability distribution functions are given in Fig. 4.4 for all four locations. The first plot, Fig. 4.4(a), gives the probability distribution function in front of the shock, confirming that the rotational energy is in equilibrium. Figure 4.4(b) gives the rotational energy probability distribution function in the shock where thermal nonequilibrium is expected. It is clear from the rotational energy probability distribution function that there is nonequilibrium. The distribution has a clear kink which is caused by particles being at two different rotational energy conditions, some equilibrated to the post-shock condition and others that are still at the pre-shock condition. In the third plot, Fig 4.4(c), the dual rotational energy distribution can still be clearly seen, signifying that there is still nonequilibrium. The fourth plot, Fig 4.4(d), still shows a visible kink, although in this case it is much less noticeable than at the previous two points. This small kink is produced by particles
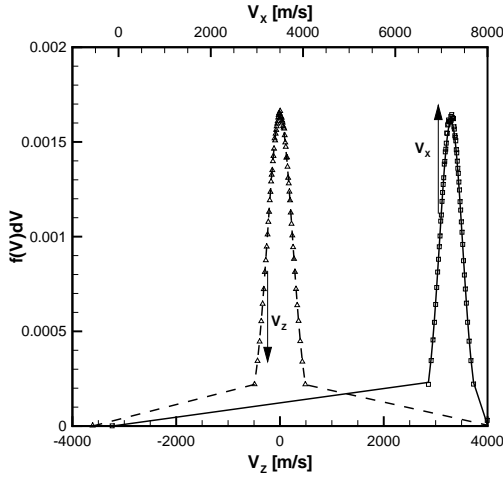
(a) $z/R = -0.60$
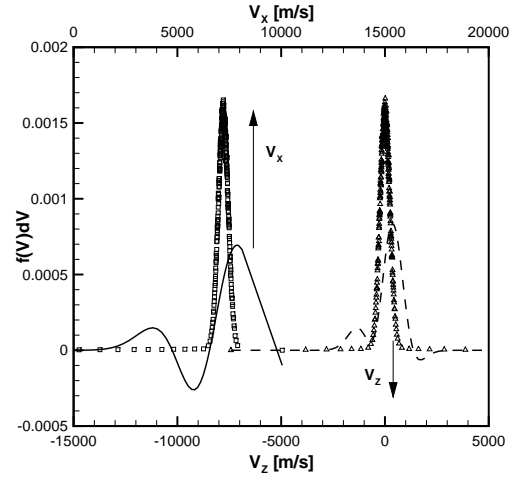
(b) $z/R = -0.30$
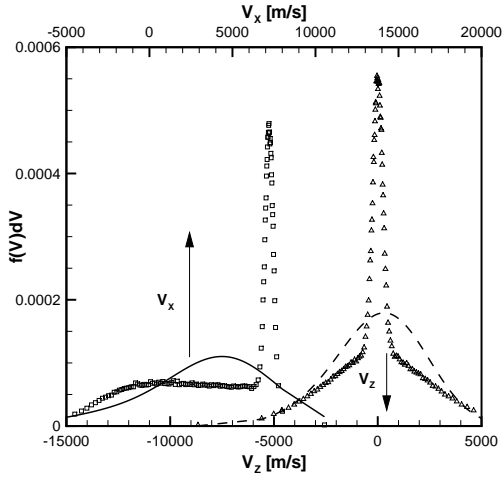
(c) $z/R = -0.15$
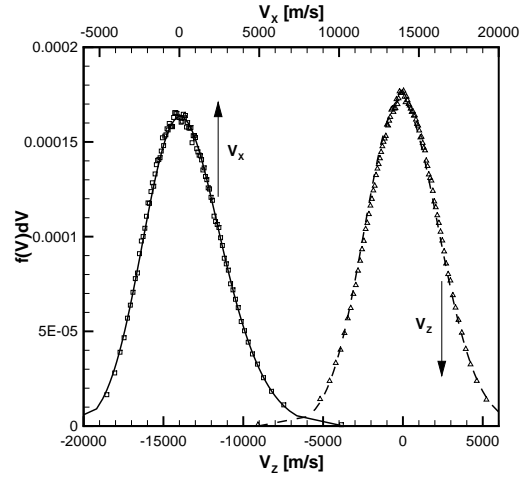
(d) $z/R = -0.05$

Figure 4.3: Velocity probability distribution functions along the stagnation stream line at four points, symbols represent particle data while lines represent Chapman-Enskog distribution

that have equilibrated with the wall. This can be seen by the good agreement with the Boltzmann distribution at the wall temperature, given as a dashed line. So, the thermal nonequilibrium seen at this point is located inside the thermal boundary layer. The CFD method is not able to capture this thermal nonequilibrium, which causes the rotational temperature to over estimate the DSMC prediction. These cases show that CFD, with a separate rotational energy, and DSMC match well, with differences appearing due to nonequilibrium conditions present in the flow.

4.3 Slip Boundary Conditions

As discussed previously in section 3.3, there are three slip boundary conditions implemented in the CFD method. In this study, to make it simpler only one slip boundary condition is desired.

A test case at Mach 10 and a Knudsen number of 0.01 in a flow of nitrogen is run using both DSMC and CFD with all three slip boundary conditions and the no-slip boundary condition. The results depicting the surface heat flux and shear stress coefficients are given in Fig. 4.5. From these figures it is observed that all slip boundary conditions improve the agreement with DSMC, but on closer inspection the Gökçen slip boundary condition provides better agreement with DSMC. The Gökçen slip boundary condition prediction of heat flux gives better agreement with DSMC in the wake, and is the only slip model to exactly capture the peak shear stress. For these reasons, the Gökçen slip model is chosen for the rest of this study, and will hence forth be referred to as the slip boundary condition.

From the previous figures it is seen that slip boundary conditions implemented in a CFD method improves the agreement of predicted surface properties with DSMC, but it is also important to understand the effects it has on other aspects of the CFD
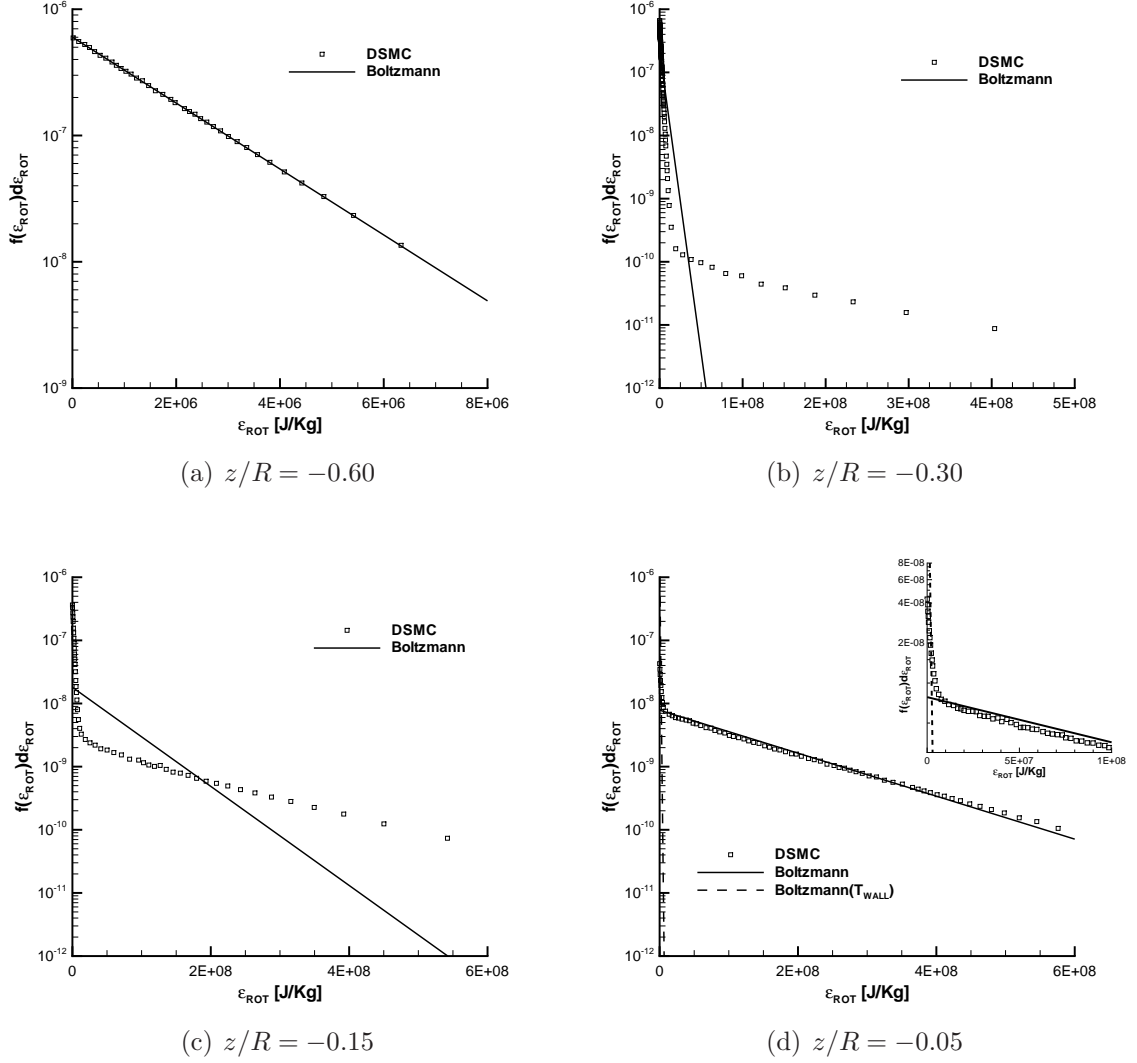
Figure 4.4: Rotational energy probability distribution functions along the stagnation stream line at four points, symbols represent particle data while lines represent Boltzmann distribution

(a) Coefficient of Heat Flux

(b) Coefficient of Shear Stress
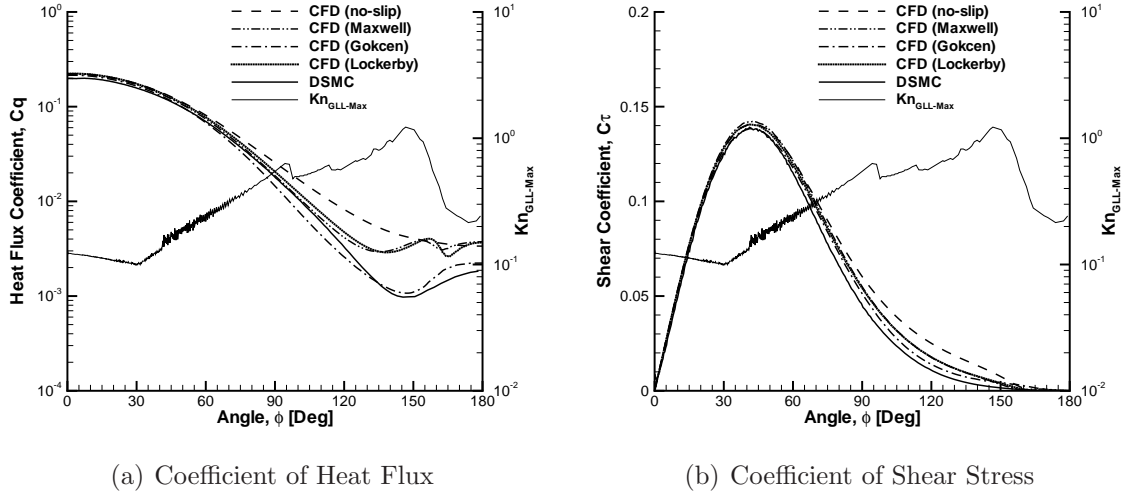
Figure 4.5: $Kn_\infty = 0.01$, surface heat flux and surface shear stress on a sphere in a Mach 10 flow of nitrogen

solution. The convergence of the L2 normal is given in Fig. 4.6 with and without slip. From Fig. 4.6(a) it can be seen that utilizing slip boundary conditions does increase the number of iterations to reach a fully converged solution by approximately 4000 iterations, for this case. Figure 4.6(b) depicts the convergence when the slip boundary condition is started from a previously fully converged solution. It can be observed that there is a spike then the solution quickly re-converges. Running simulations with slip boundary conditions does increase the numerical expense of the simulation. The reason the slip boundary condition takes longer to converge is due to the fact that the slip boundary conditions are handled explicitly in an implicit solver. It is expected that if the slip boundary conditions were dealt with in a implicit manner, there would be no difference with the required number of iterations to reach a converged solution. It should be noted that slip boundary conditions do not affect the robustness of the CFD code, the Courant-Friedrichs-Lewy (CFL) number does not differ between CFD with the no-slip and slip boundary conditions.

While it is observed that slip boundary conditions do affect the convergence of the

(a) Convergence Without Re-Start   (b) Convergence From Re-Start
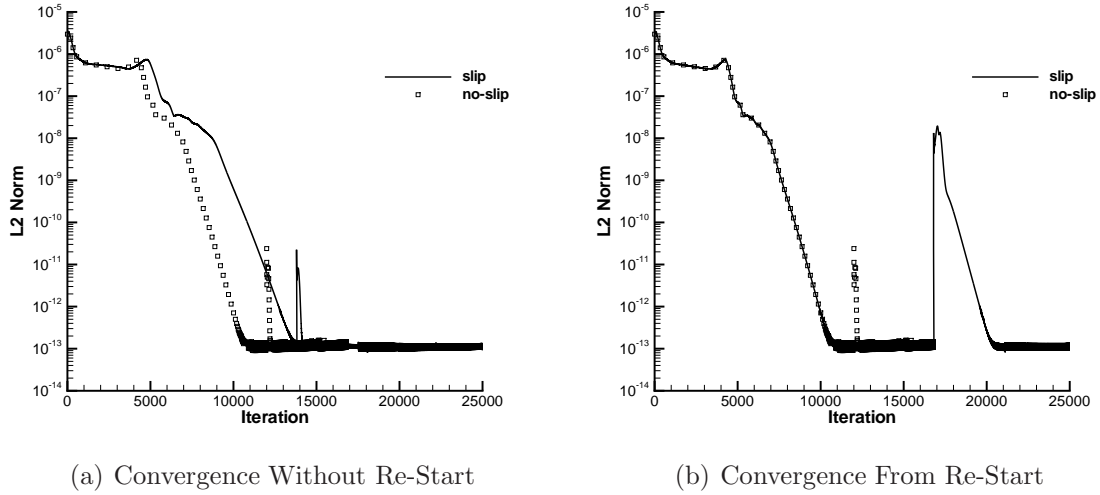
Figure 4.6: Convergence of L2 normal with and without slip boundary conditions

CFD method, it is still not clear if including slip boundary conditions affects the flow field. Figure 4.7 gives the horizontal velocity from DSMC, in flooded contours, and CFD for all three slip boundary conditions along with the no-slip boundary condition, in contour lines, in the fore body and aft body of the sphere. Figure 4.7(a) shows that all the contours line up well near the stagnation point. Near the shock there are significant differences between CFD and DSMC, but this is an expected result due to DSMC predicting a thicker shock. In the aft body, Fig. 4.7(b), there are larger differences observed, but slip boundary conditions show improved agreement with DSMC. It can be seen that Maxwell and Lockerby slip models perform better near the surface with the Gökçen slip model performing better further away from the body.

Figure 4.8 gives the corresponding translational temperature contours from DSMC and CFD for all three slip boundary conditions and the no-slip boundary condition in the wake and fore body of the sphere. Translational temperature agrees well near the stagnation point, as depicted in Fig. 4.8. It can also be seen that CFD and

(a) Fore Body   (b) Aft Body
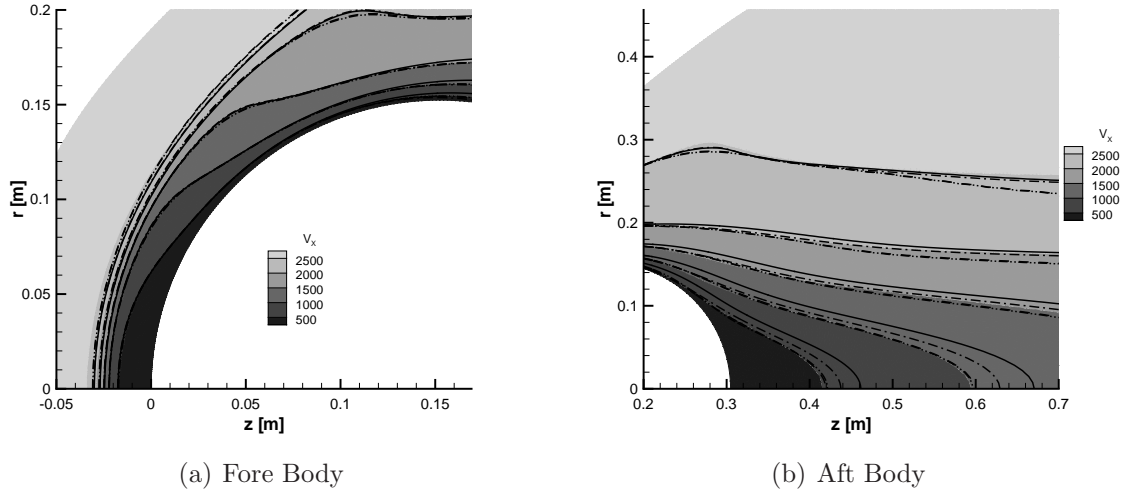
Figure 4.7: Effects of slip boundary conditions on the horizontal velocity over a sphere in Mach 10 $Kn_\infty = 0.01$ nitrogen flow; flood represents DSMC, solid line is no-slip, dashed line gives Maxwell slip, dashed-dot line represents Gökçen slip, dashed dot line is Lockerby slip

DSMC show disagreement near the shock, due to strong thermal nonequilibrium and a thicker shock predicted by DSMC. The translational temperature in the wake of the sphere is given in Fig. 4.8(b). From this figure it can be seen that there is significant difference between CFD and DSMC, but it should be noted that slip improves agreement with DSMC.

From these figures it can be observed that, in all cases, slip boundary conditions improve the agreement with DSMC.

4.4 Flow Over a Sphere

The following results are presented in order of increasing Mach number while varying the global Knudsen number. This allows the changes in breakdown due to increasing global Knudsen number to be easily seen, while still permitting the comparison of increasing Mach number.

(a) Fore Body　　　　　　　　　　(b) Aft Body
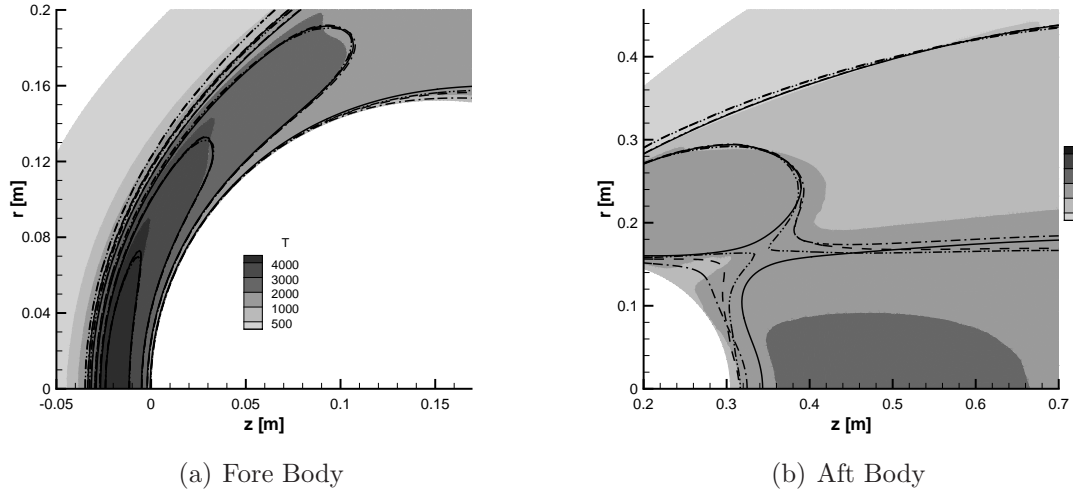
Figure 4.8: Effects of slip boundary conditions on the translational temperature over a sphere in Mach 10 $Kn_\infty = 0.01$ nitrogen flow; flood represents DSMC, solid line is no-slip, dashed line gives Maxwell slip, dashed-dot line represents Gökçen slip, dashed dot line is Lockerby slip

4.4.1　Mach 10

To begin with, the results for the Mach 10 simulations at Knudsen numbers of 0.002 to 0.25 are discussed in detail. The integrated drag and peak heat flux are given in Tables 4.2 and 4.3, respectively. The tables give the values predicted by DSMC and CFD along with a percent difference between the two methods. Since DSMC is a particle method that works in both the continuum regime and the rarefied regime, it is assumed that the DSMC results are more accurate, so the percent difference is calculated using the DSMC result as the basis. At the lowest Knudsen number, the integrated drag predictions and peak heat flux are nearly identical. However, as the Knudsen number grows, the results diverge. It can be seen that slip boundary conditions improve the agreement between CFD and DSMC in all cases.

Table 4.2: Integrated Drag [N] (% difference) from DSMC and CFD at Mach 10

Kn_∞	Re_∞	DSMC	CFD (no-slip)	CFD (slip)
0.002	6,400	29.0	29.0(0.00%)	28.9(-0.34%)
0.01	1,280	6.42	6.60(2.78%)	6.47(0.78%)
0.05	256	1.60	1.83(14.0%)	1.61(0.63%)
0.25	51.2	0.42	0.71(67.4%)	0.43(2.38%)

Table 4.3: Peak Heating $\left[\frac{W}{m^2}\right]$ (% difference) from DSMC and CFD at Mach 10

Kn_∞	Re_∞	DSMC	CFD (no-slip)	CFD (slip)
0.002	6,400	1.09×10^5	$1.13\times10^5(3.40\%)$	$1.13\times10^5(3.19\%)$
0.01	1,280	4.71×10^4	$5.28\times10^4(12.0\%)$	$5.08\times10^4(7.79\%)$
0.05	256	2.10×10^4	$2.54\times10^4(20.9\%)$	$2.28\times10^4(8.46\%)$
0.25	51.2	6.43×10^3	$1.02\times10^4(58.4\%)$	$7.16\times10^3(11.5\%)$

From the integrated drag and the total heat flux there is a correlation between increasing Knudsen number and increasing difference between DSMC and CFD results. Each Knudsen number case is discussed in more detail in the following sections.

$\mathbf{Kn_\infty = 0.002}$

At a global Knudsen number of 0.002, the flow is expected to be well within the continuum regime, therefore CFD should have no problem properly simulating this flow. However, there is still continuum breakdown in the flow, as shown in Fig. 4.9(a). This figure shows that there is continuum breakdown in the shock and in the wake of the sphere. At this global Knudsen number, CFD and DSMC give approximately the same amount of continuum breakdown in the flow, even the shocks predicted by DSMC and CFD have approximately the same thickness and location.

(a) Kn_{GLL} (b) Coefficient of Pressure

Figure 4.9: $Kn_\infty = 0.002$, Kn_{GLL} and surface pressure (left axis) and Kn_{GLL} surface profile (right axis) on a sphere in a Mach 10 flow of nitrogen

The surface coefficient of pressure is given in Fig. 4.9(b). It can be seen that the pressures predicted by DSMC and CFD agree very well. A theoretical calculation of the coefficient of stagnation pressure, found in the inviscid limit to be 1.825, compares well with the numerical prediction of 1.823. The heat flux coefficient over the surface of the sphere is given in Fig. 4.10(a). The CFD prediction of surface heat flux coefficient is higher than DSMC over most of the surface, but CFD under predicts DSMC over the back side of the sphere. An estimate of the stagnation point heat flux coefficient using a real gas Fay-Riddell analysis[81] is found to be 0.0874 which compares well to the numerically predicted value of 0.09. The surface plots also show that Kn_{GLL} is greater than 0.05 over the whole surface, which means breakdown has occurred. The shear stress along the surface, as given in Fig. 4.10(b), compares very well over the surface. The CFD and DSMC predictions for shear stress coefficient start to diverge over the backside of the sphere, which is to be expected since there is a large area of breakdown in the wake. From these figures it is seen that slip boundary conditions have little effect on the surface properties. This confirms what

(a) Coefficient of Heat Flux   (b) Coefficient of Shear Stress

Figure 4.10: $Kn_\infty = 0.002$, surface heat flux (left axis), surface shear stress (left axis) and Kn_{GLL} surface profile (right axis) on a sphere in a Mach 10 flow of nitrogen

is already known; at low Knudsen numbers, no-slip is a good approximation.

$\mathbf{Kn_\infty = 0.01}$

The traditional, but often debated, limit for accurate CFD simulations is a global Knudsen number of 0.01. From Fig. 4.11(a) it can be seen from the contours of Kn_{GLL} that there is breakdown occurring in the shock, near the wall and in the wake of the sphere. It should be noted that at this global Knudsen number, DSMC predicts a larger amount of breakdown in the wake than CFD. Also, at this condition, the shock is noticeably thicker in the DSMC case while the location of the shock is approximately the same for DSMC and CFD.

Even at this higher global Knudsen number, the pressures from DSMC and CFD still agree very well. For this case, the flow is in continuum breakdown from the shock all the way to the wall on the stagnation streamline, which may explain the small discrepancies in pressure. The surface heat flux coefficient predicted by CFD with no-slip is always larger than DSMC, however slip boundary conditions significantly

(a) Kn_{GLL}

(b) Coefficient of Pressure
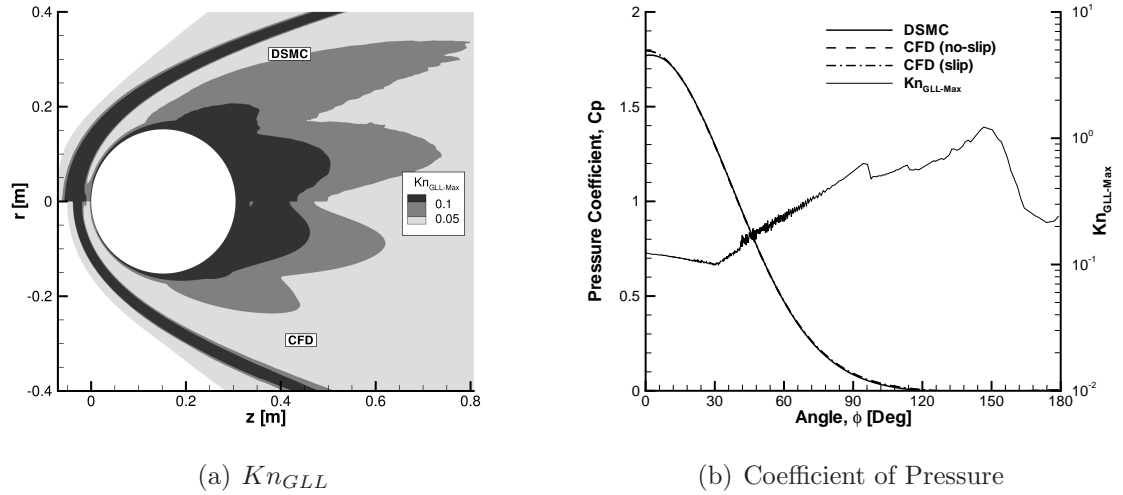
Figure 4.11: $Kn_\infty = 0.01$, Kn_{GLL} and surface pressure (left axis) and Kn_{GLL} surface profile (right axis) on a sphere in a Mach 10 flow of nitrogen

improve the heat flux predicted by CFD especially on the aft body as shown in Fig. 4.12(a). The shear stress coefficient, given in Fig. 4.12(b), compares well between the two techniques near the stagnation region but then begins to diverge over the latter part of the surface. The slip boundary condition improves the agreement between CFD and DSMC for the shear stress. For this case it is easy to notice that the shear and heat flux on the surface are higher in CFD than DSMC, but the slip boundary condition improves the agreement. The surface profile of Kn_{GLL} shows that the entire surface is considered to be in breakdown, which may explain the disagreement between CFD and DSMC.

$Kn_\infty = 0.05$

At a global Knudsen number of 0.05, the flow is outside the supposed limit for physically accurate CFD simulations, it is in the transition regime between continuum flow and a rarefied gas. The flow does show that there is a large amount of breakdown in the shock, boundary layer and wake, as seen in Fig. 4.13(a). From

(a) Coefficient of Heat Flux

(b) Coefficient of Shear Stress
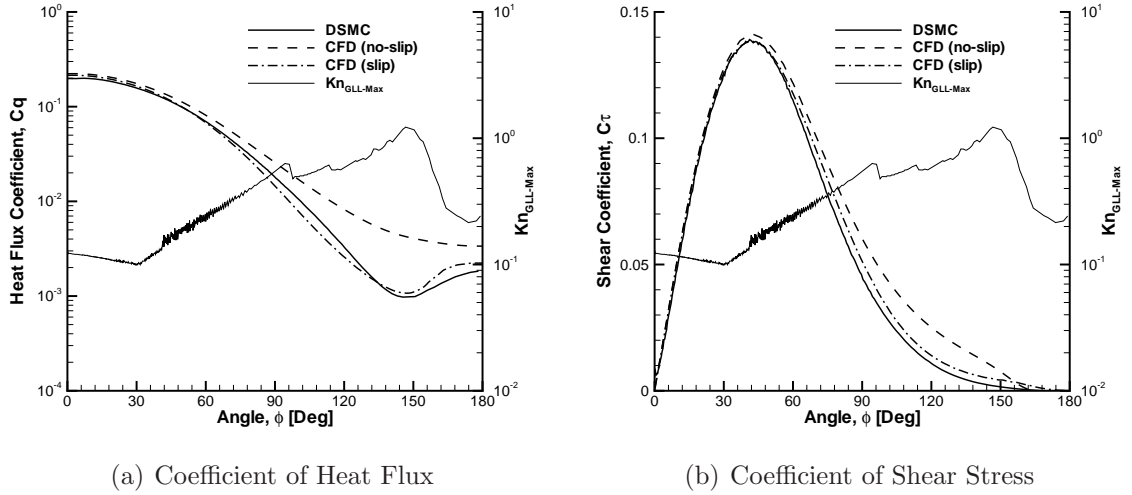
Figure 4.12: Kn_∞=0.01, surface heat flux (left axis), surface shear stress (left axis) and Kn_{GLL} surface profile (right axis) on a sphere in a Mach 10 flow of nitrogen

this figure it is seen that Kn_{GLL} exceeds the critical value of 0.05 for a large part of the domain for both CFD and DSMC. This means that continuum breakdown has occurred and CFD should have difficulty simulating the flow accurately. While the amount of breakdown in the shock is approximately the same it can be seen that the breakdown predicted by CFD is larger in the wake.

The surface pressure on the sphere simulated by CFD and DSMC is still in very good agreement as shown in Fig. 4.13(b). One oddity is that the CFD prediction of pressure is less than DSMC at the stagnation point, although this effect is not observed with slip boundary conditions. The surface heat flux, as seen in Fig. 4.14(a), displays a large separation between CFD with no-slip and DSMC. This separation starts at the stagnation point and goes all the way to the backside of the sphere. When the slip boundary condition is utilized, the heat transfer coefficient drops, improving the agreement between CFD and DSMC, although not as much as the peak heating comparison would lead one to believe. The shear stress, given in Fig. 4.14(b),

(a) Kn_{GLL} (b) Coefficient of Pressure
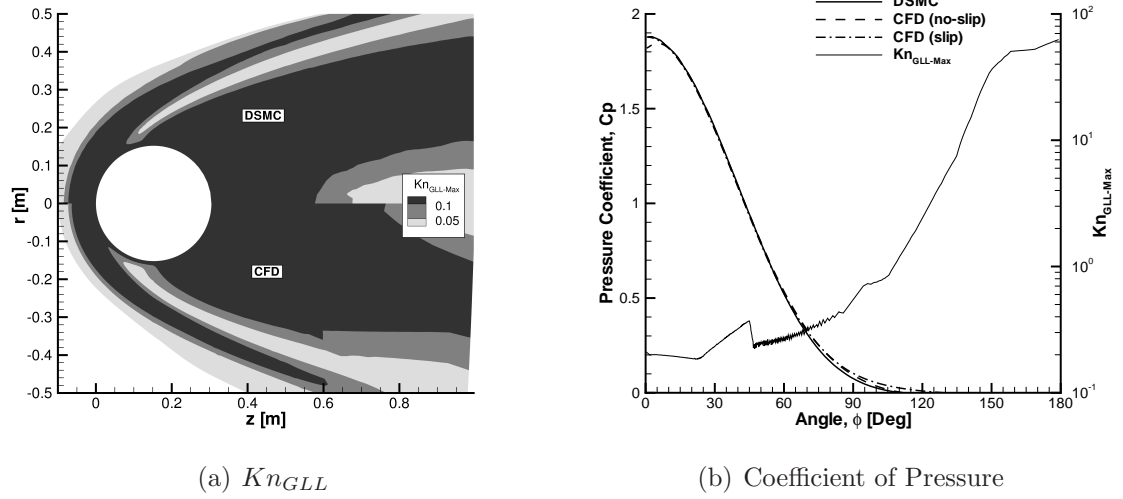
Figure 4.13: $Kn_{\infty} = 0.05$, Kn_{GLL} and surface pressure (left axis) and Kn_{GLL} surface profile (right axis) on a sphere in a Mach 10 flow of nitrogen

for both DSMC and CFD with no-slip agree very well over the first 25 degrees, but then the two diverge over the rest of the surface due to the growing amount of breakdown. The no-slip CFD prediction for the surface shear stress gives the peak value at a slightly later point on the surface and gives a value higher than DSMC does. The slip boundary condition significantly improves the agreement between CFD and DSMC for the shear stress, giving the same peak value at the same location as DSMC.

$Kn_{\infty} = 0.25$

The last, and highest global Knudsen number that is discussed in this work is 0.25. This gives a flow that is well outside of the continuum regime and is now a rarefied gas. At this Knudsen number, the flow is nearly entirely in continuum breakdown, as seen in Fig. 4.15(a). There is only a small portion that is not in continuum breakdown behind the sphere for DSMC. At this global Knudsen number, the shock is very far out in front of the sphere, approximately 0.4 m from the stagnation point,

(a) Coefficient of Heat Flux   (b) Coefficient of Shear Stress
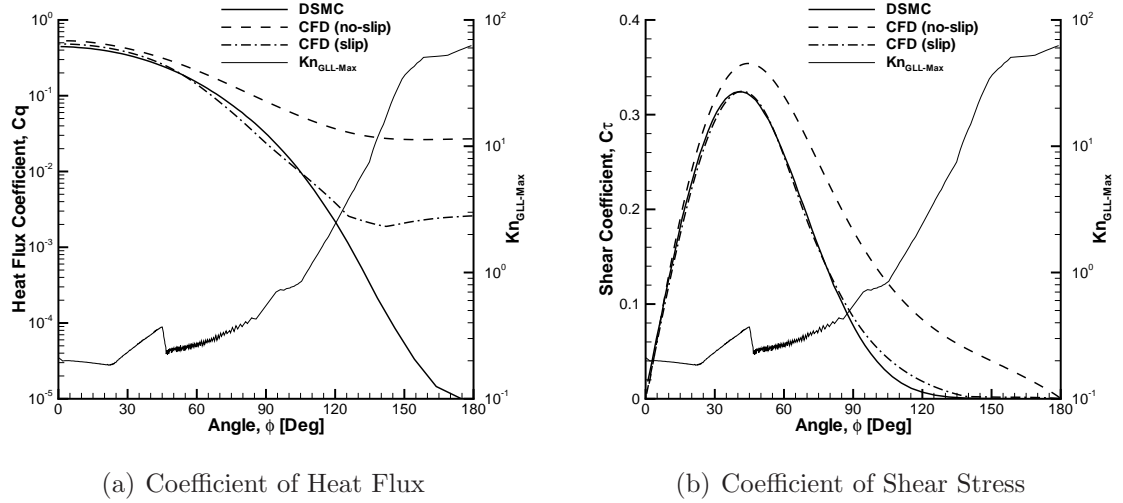
Figure 4.14: $Kn_\infty = 0.05$, surface heat flux (left axis), surface shear stress (left axis) and Kn_{GLL} surface profile (right axis) on a sphere in a Mach 10 flow of nitrogen

while in the other cases it is less than 0.1 m from the stagnation point.

At a global Knudsen number of 0.25, the flow is rarefied and as a result the entire flow is considered to be in continuum breakdown, which has a significant effect on the surface properties of the sphere. Figure 4.15(b) gives the coefficient of pressure along the surface of the sphere. It is interesting to note that at this global Knudsen number, the no-slip CFD predicted coefficient of pressure goes above 2 at the stagnation point. A theoretical calculation of the coefficient of stagnation pressure, found in the free molecular limit[26] to be 2.25, shows that a value near two is still within reason at this high a global Knudsen number. The surface heat flux coefficient, given in Fig. 4.16(a), shows that there is a large difference between DSMC and CFD with no-slip over the whole surface of the sphere. An estimate of the stagnation point heat flux coefficient using free molecular theory is found to be 0.941 verifying that the numerically found value of 0.7 is within reason. Figure 4.16(b) shows the shear stress coefficient along the surface of the sphere. The shear stresses agree well near

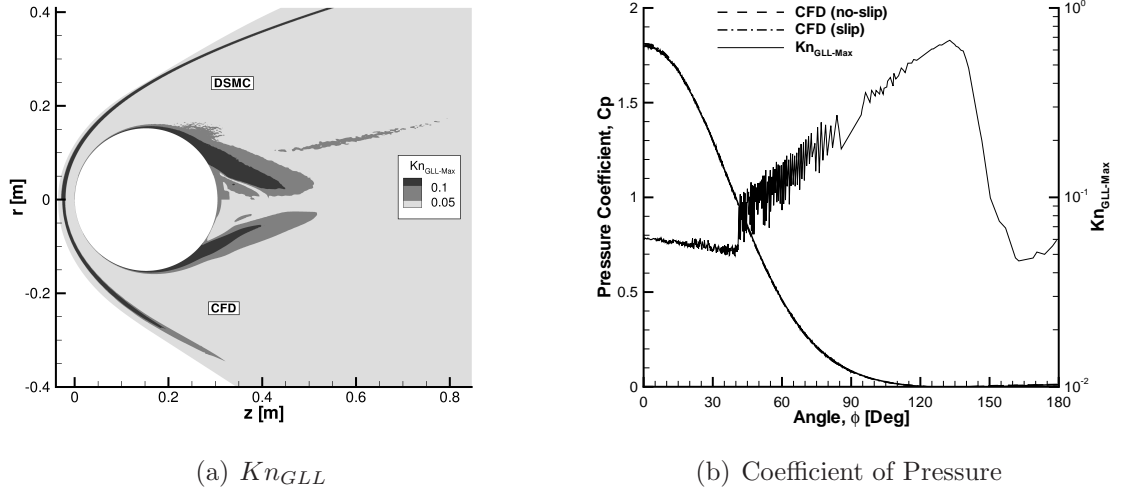(a) Kn_{GLL} (b) Coefficient of Pressure

Figure 4.15: $Kn_\infty = 0.25$, Kn_{GLL} and surface pressure (left axis) and Kn_{GLL} surface profile (right axis) on a sphere in a Mach 10 flow of nitrogen

the stagnation point, but then DSMC and CFD start to diverge. The shear stress predicted by DSMC gives a peak at a smaller angle and at a much smaller magnitude than CFD with no-slip. Utilizing the slip boundary conditions in this case did not improve the agreement.

It can be seen that as the Knudsen number grows, the CFD method over predicts pressure as compared to DSMC. To determine the reason for this phenomenon, the pressure profiles along the stagnation streamline for the Knudsen number 0.002 and 0.01 cases are examined, as given in Fig. 4.17. The profile of the gradient length local Knudsen number along the stagnation streamline is also included in the figures. To bound the numerical data, the free stream pressure is given as a solid line while the stagnation pressure, found using the Rankine-Hugoniot relations for a steady shock with real gas effects[82, 81], is given as a dashed line. From Fig. 4.17(a), it can be seen that the pressure predicted by the DSMC and CFD methods agree very well along the stagnation streamline. This level of agreement is expected given that the gradient length local Knudsen number is below the 0.05 limit, except in the shock

(a) Coefficient of Heat Flux

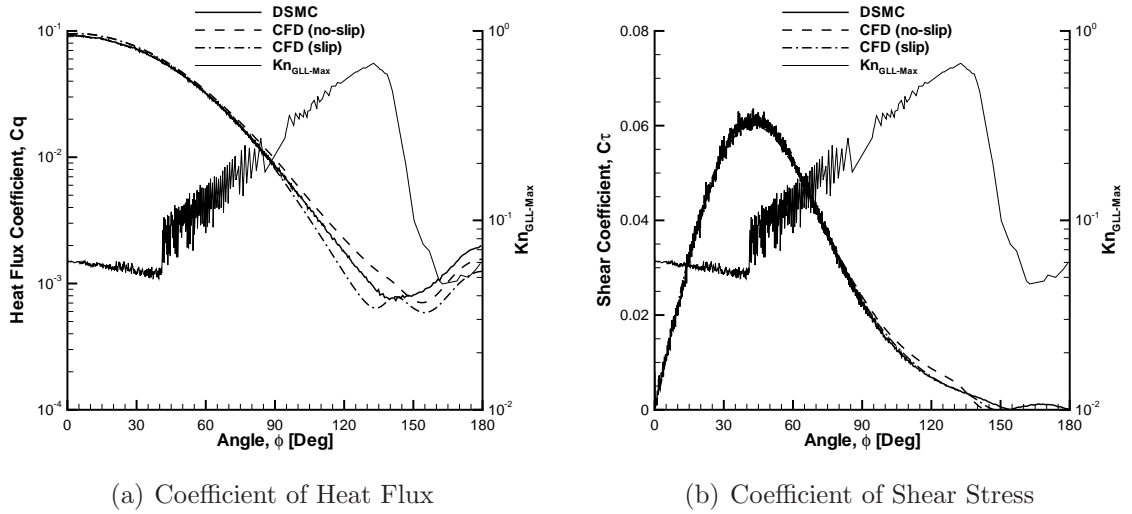(b) Coefficient of Shear Stress

Figure 4.16: $Kn_\infty = 0.25$, surface heat flux (left axis), surface shear stress (left axis) and Kn_{GLL} surface profile (right axis) on a sphere in a Mach 10 flow of nitrogen

and at the wall, indicating the flow is only in continuum breakdown in the shock and at the wall. It can also be seen that both CFD and DSMC agree with the theoretical stagnation pressure. From Fig. 4.17(b), the pressures predicted by the CFD and DSMC methods show some disagreement. It can be seen that the gradient length local Knudsen number is above the 0.05 limit, indicating the the flow along that stagnation streamline is in continuum breakdown. From this figure it can be seen that CFD predicts a stagnation pressure higher than the theoretical calculation, but DSMC provides good agreement with the theoretical stagnation pressure. There are two important points to note about these figures. First, as the Knudsen number increases it can be seen that CFD starts to over predict not only DSMC, but the theoretical stagnation pressure as well. Second, the CFD method reaches the post-shock pressure quicker than the DSMC method. This is caused by higher gradients being calculated in the CFD method, which has the effect of making the shock thinner and ultimately causing pressure to be over predicted in the post-shock region.

(a) $Kn_\infty = 0.002$ (b) $Kn_\infty = 0.01$
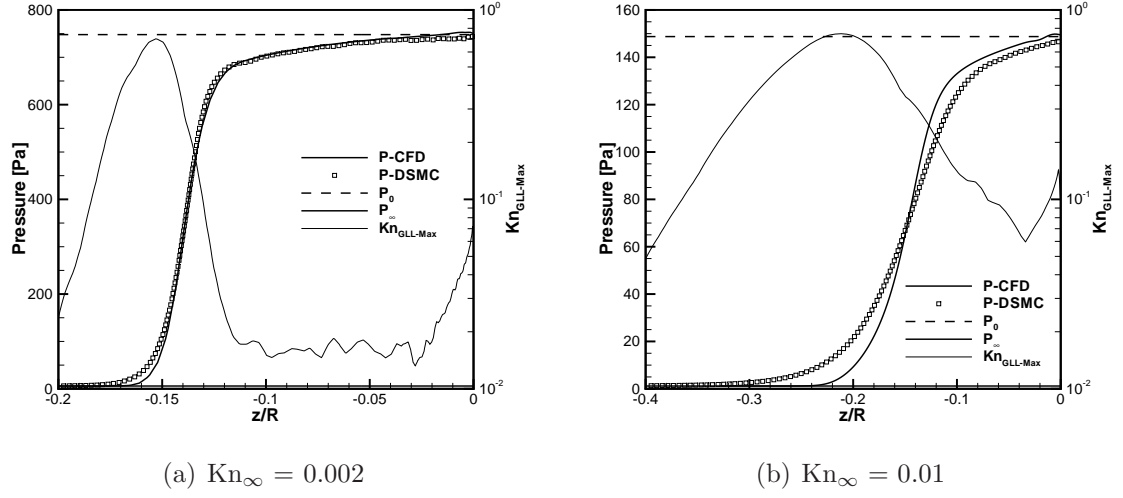
Figure 4.17: Pressure profiles along the stagnation streamline. The maximum Kn_{GLL} is plotted on the right axis. Flow is from left to right; distance is normalized by the radius of the sphere.

Computational Details

Relevant computational details of the Mach 10 simulations from DSMC and CFD are given in Tables 4.4 and 4.5, respectively. The CFD cases in Table 4.5 are for simulations with no-slip boundary conditions. In general, simulations with slip boundary conditions did not take any longer to converge, as discussed in section 4.3.

Table 4.4: Computational Details for DSMC Mach 10 Simulations

Kn_∞	Cells	Particles	Time Steps	CPU Time [hrs]
0.002	1,293,365	94,204,304	250,000	12,240
0.01	74,012	20,014,670	143,000	4,608
0.05	9,432	4,517,502	157,000	384
0.25	7,836	2,147,885	139,000	192

Table 4.5: Computational Details for CFD Mach 10 Simulations

Kn_∞	Cells	Iterations	CPU Time [hrs]
0.002	48,000	20,000	320
0.01	40,000	12,276	192
0.05	26,000	14,000	112
0.25	12,000	30,000	112

4.4.2 Mach 25

The next set of results discussed is for a Mach 25 flow at Knudsen numbers of 0.002 to 0.25. At this Mach number, there is rotational and vibrational nonequilibrium. The integrated drag and peak heat flux are given in Tables 4.6 and 4.7, respectively. The tables give the values predicted by DSMC and CFD along with a percent difference between the two methods, assuming DSMC is more accurate. From the tables below it is clear that the differences between CFD and DSMC grow with increasing Knudsen number. It is interesting to note, when comparing the Mach 25 results with those found in Tables 4.2 and 4.3 for Mach 10, the percent differences are comparable, even though the values predicted by DSMC and CFD are not.

Table 4.6: Integrated Drag [N] (% difference) from DSMC and CFD at Mach 25

Kn_∞	Re_∞	DSMC	CFD (no-slip)	CFD (slip)
0.002	16,000	180	181(0.55%)	181(0.55%)
0.01	3,200	41.2	42.4(2.91%)	40.3(-2.18%)
0.05	639	10.5	13.0(23.8%)	10.8(2.78%)
0.25	128	2.46	5.24(113%)	3.20(30.1%)

Table 4.7: Peak Heating $\left[\frac{W}{m^2}\right]$ (% difference) from DSMC and CFD at Mach 25

Kn_∞	Re_∞	DSMC	CFD (no-slip)	CFD (slip)
0.002	16,000	2.14×10^6	$2.20\times10^6(2.92\%)$	$2.18\times10^6(1.82\%)$
0.01	3,200	9.81×10^5	$1.08\times10^6(10.2\%)$	$1.03\times10^6(4.87\%)$
0.05	639	3.92×10^5	$4.90\times10^5(25.0\%)$	$4.59\times10^5(17.1\%)$
0.25	128	1.06×10^5	$1.88\times10^5(76.9\%)$	$1.36\times10^5(28.4\%)$

The integrated drag and the total heat flux results are similar to the Mach 10 case in that there is a correlation between increasing Knudsen number and increasing difference between DSMC and CFD results. The results of each Knudsen number are discussed in more detail in the following sections.

$\mathbf{Kn_\infty = 0.002}$

For this case it can be seen, in Fig. 4.18(a), that the gradient length local knudsen number is greater than 0.05 in the shock and wake of the sphere, indicating that continuum breakdown has occurred in those regions. From this figure, it can also be seen that DSMC predicts a larger amount of continuum breakdown than CFD. It can be observed, from both CFD and DSMC, that there is a larger area of continuum breakdown in the shock and wake of the sphere as compared to the Mach 10 case, in section 4.4.1. It should be noted that the location of the shock is approximately the same as in the Mach 10 case.

Even though the Knudsen number is in the continuum regime, the gradient length local Knudsen number, as seen in Fig. 4.18(a), is greater than the 0.05 limit across the entire surface, indicating that the surface is in continuum breakdown. Despite the continuum breakdown on the surface, the coefficient of pressure agrees well between the two methods, as shown in Fig. 4.18(b). The stagnation coefficient of pressure

(a) Kn_{GLL}

(b) Coefficient of Pressure
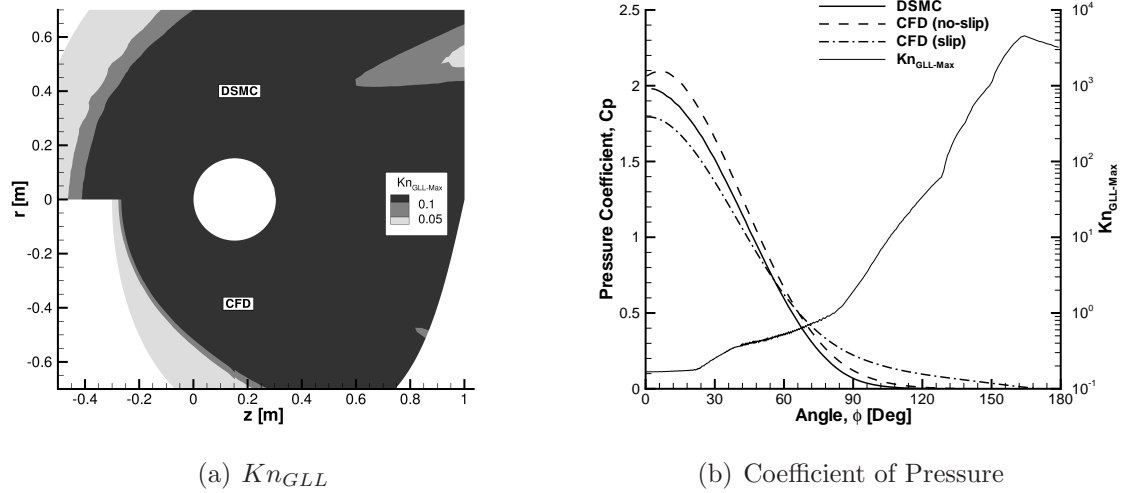
Figure 4.18: $Kn_{\infty} = 0.002$, Kn_{GLL} and surface pressure (left axis) and Kn_{GLL} surface profile (right axis) on a sphere in a Mach 25 flow of nitrogen

found in the inviscid limit is 1.832, which compares well with the numerically found value of 1.839. The heat flux coefficient displays good agreement between CFD and DSMC in the fore body of the sphere, with disagreement over the aft of the sphere as shown in Fig. 4.19(a). An estimate of the stagnation point heat flux coefficient using a real gas Fay-Riddell analysis is found to be 0.094, which provides reasonable agreement with the numerically predicted value of 0.115. The shear stress, as given in Fig. 4.10(b), compares very well over the surface. It is not surprising to note that at this Knudsen number the inclusion of the slip boundary condition in the CFD method has little effect on the final results.

$Kn_{\infty} = 0.01$

For this case there is breakdown occurring in the shock, near the wall and in the wake of the sphere, as seen in Fig. 4.20(a). From this figure, it can also be seen that the amount of continuum breakdown predicted by DSMC is greater than the amount of breakdown predicted by CFD. It should be noted that at this Mach number, as

(a) Coefficient of Heat Flux
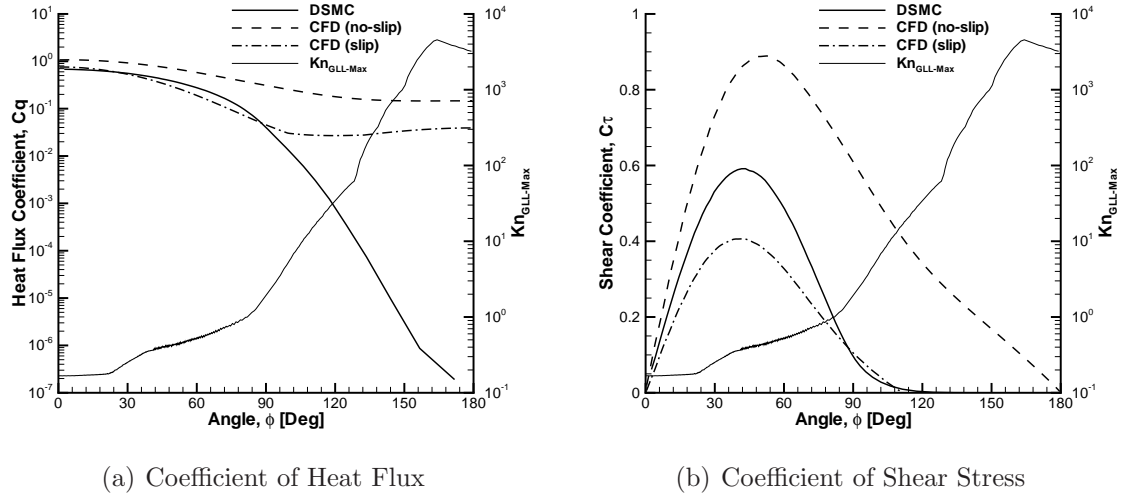
(b) Coefficient of Shear Stress

Figure 4.19: Kn_∞=0.002, surface heat flux (left axis), surface shear stress (left axis) and Kn_{GLL} surface profile (right axis) on a sphere in a Mach 25 flow of nitrogen

compared to Mach 10 in section 4.4.1, DSMC and CFD predict a larger amount of continuum breakdown. It can also be observed that the shock is thicker, but it remains in nearly the same location.

The surface pressure coefficient predicted by DSMC and no-slip CFD agree well, as seen in Fig. 4.20(b). The surface pressure predicted by CFD with the slip boundary conditions improves agreement with DSMC. The heat flux coefficient, given in Fig. 4.21(a), predicted by CFD with no-slip boundary conditions is always larger than DSMC. However, the slip boundary condition improves the agreement between CFD and DSMC. The shear stress coefficient, given in Fig. 4.21(b), compares well between the two techniques near the stagnation region but begins to diverge over the latter part of the sphere. From this figure it is also seen that while CFD has a higher magnitude at the peak, the peak for both DSMC and CFD occur at approximately the same location. Again, the slip boundary condition improves the agreement between CFD and DSMC for the shear stress coefficient.

(a) Kn_{GLL}

(b) Coefficient of Pressure

Figure 4.20: $Kn_\infty = 0.01$, Kn_{GLL} and surface pressure (left axis) and Kn_{GLL} surface profile (right axis) on a sphere in a Mach 25 flow of nitrogen
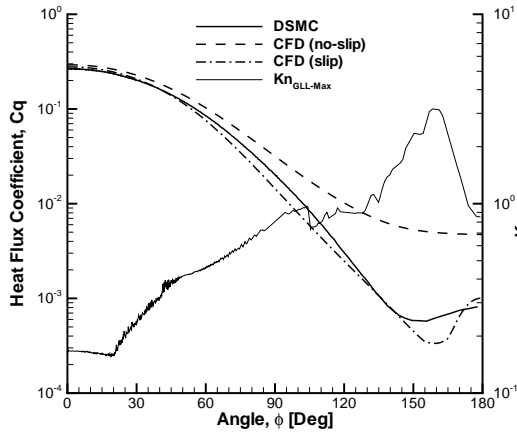
(a) Coefficient of Heat Flux
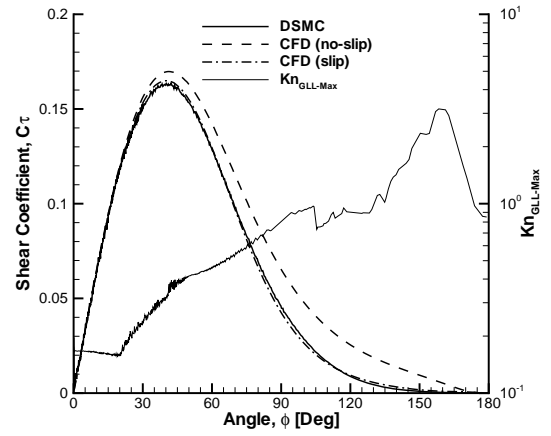
(b) Coefficient of Shear Stress

Figure 4.21: Kn_∞=0.01, surface heat flux (left axis), surface shear stress (left axis) and Kn_{GLL} surface profile (right axis) on a sphere in a Mach 25 flow of nitrogen

(a) Kn_{GLL}

(b) Coefficient of Pressure

Figure 4.22: $Kn_\infty = 0.05$, Kn_{GLL} and surface pressure (left axis) and Kn_{GLL} surface profile (right axis) on a sphere in a Mach 25 flow of nitrogen

$Kn_\infty = 0.05$

The contours of gradient length local Knudsen number are given in Fig. 4.22(a). It can be seen that Kn_{GLL} is greater than the 0.05 limit in the shock, near the surface and in the wake of the sphere. Indicating significant continuum breakdown in these regions. From this figure it can also be seen that DSMC predicts a larger area of continuum breakdown than CFD. Comparing with the Mach 10 case, section 4.4.1, it can be observed that both methods predict larger amounts of continuum breakdown; this is most noticeable in the shock region.

The surface pressure displays good agreement between CFD and DSMC, as shown in Fig. 4.22(b). This figure also gives the gradient length local Knudsen number, which shows that at the surface the Kn_{GLL} is over 0.05; indicating the flow is in continuum breakdown. The CFD method over predicts the heat flux over the entire surface as compared to DSMC, as shown in Fig. 4.23(a). There is an improvement in the agreement with DSMC when the slip boundary condition is utilized in the

(a) Coefficient of Heat Flux

(b) Coefficient of Shear Stress
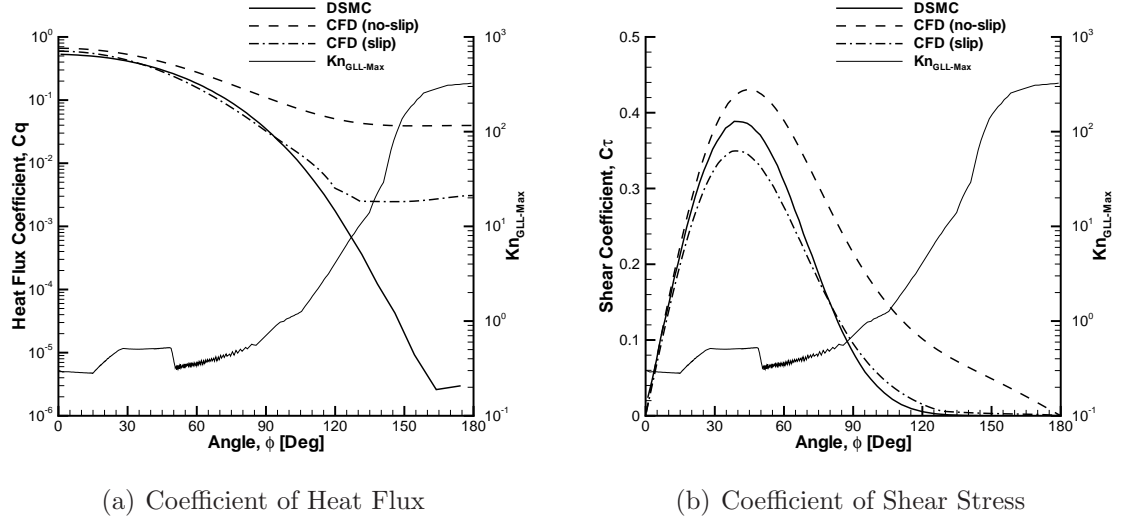
Figure 4.23: $Kn_\infty=0.05$, surface heat flux (left axis), surface shear stress (left axis) and Kn_{GLL} surface profile (right axis) on a sphere in a Mach 25 flow of nitrogen

CFD method, but there is still a large disagreement over the aft of the sphere. The shear stress coefficient, given in Fig. 4.23(b), is over predicted by CFD assuming no-slip boundaries as compared to DSMC. However, when a slip boundary condition is employed in the CFD technique the shear coefficient under predicts DSMC over the fore body, but over predicts DSMC for the rest of the surface. Notice that CFD with the slip boundary condition predicts the peak shear stress in approximately the same location as DSMC.

$\mathbf{Kn_\infty = 0.25}$

At this Knudsen number, most of the flow field is considered to be in breakdown, as seen in Fig. 4.24(a). At a global Knudsen number of 0.25, the flow is considered to be rarefied so it is not surprising to see large amounts of continuum breakdown in the flow. Comparing to the Mach 10 case, section 4.4.1, it can be observed that the shock has moved further away from the body causing the amount of continuum breakdown to increase. The shock front in this case is approximately 0.6 m in front
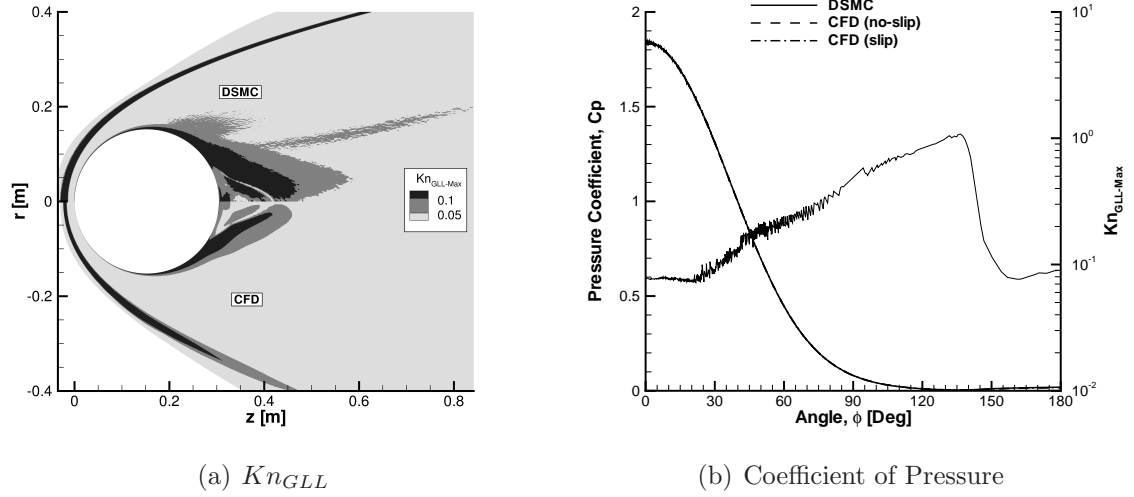
(a) Kn_{GLL}

(b) Coefficient of Pressure

Figure 4.24: $Kn_\infty = 0.25$, Kn_{GLL} and surface pressure (left axis) and Kn_{GLL} surface profile (right axis) on a sphere in a Mach 25 flow of nitrogen

of the body while it is approximately 0.4 m in the Mach 10 case.

At this Knudsen number, the flow is considered to be rarefied and this can be clearly seen in the coefficient of pressure, given in Fig. 4.24(b). The CFD method, with or without a slip boundary condition, over predicts DSMC for the surface pressure. It is interesting to note that, in the free molecular limit, the stagnation coefficient of pressure is 2.06, which confirms the pressure predicted by DSMC is reasonable. However, in this case the CFD method predicts the stagnation coefficient to be an unreasonable 2.5. The heat flux coefficient, given in Fig. 4.25(a), shows that CFD over predicts DSMC over the whole surface. The inclusion of a slip boundary condition in the CFD method helps improve the agreement, but still over predicts DSMC. A theoretical calculation of the stagnation point heat flux in the free molecular limit is found to be 0.976, which verifies the DSMC found value of 0.72 is within reason. As expected, the CFD method predicts the stagnation point coefficient to be an unreasonable 1.27, but CFD with the slip boundary condition gives a more reasonable value of 0.92. Figure 4.25(b) gives the shear stress coefficient

(a) Coefficient of Heat Flux
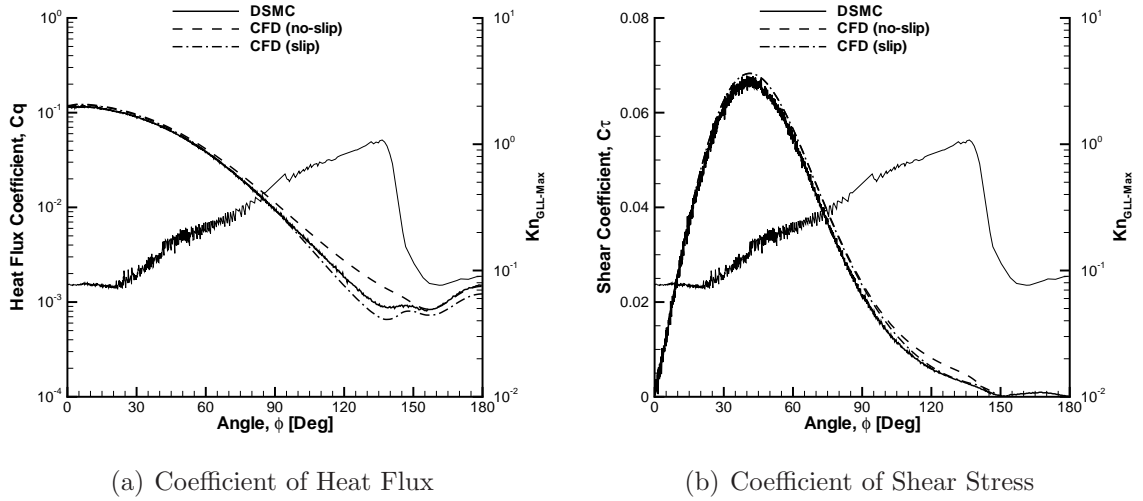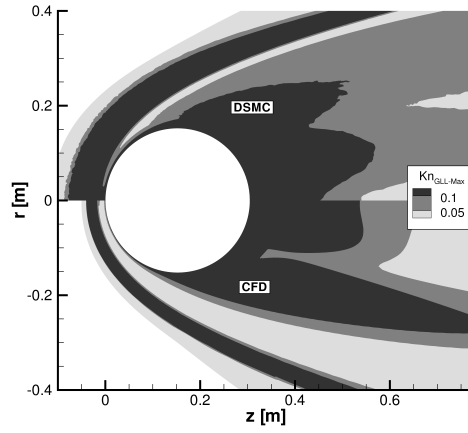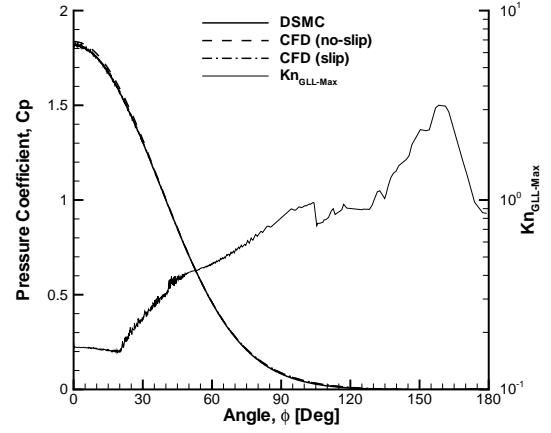
(b) Coefficient of Shear Stress

Figure 4.25: Kn_∞=0.25, surface heat flux (left axis), surface shear stress (left axis) and Kn_{GLL} surface profile (right axis) on a sphere in a Mach 25 flow of nitrogen

found with the DSMC and CFD methods. The CFD method predicts a larger value of the shear stress than DSMC. CFD with the slip boundary condition predicts a smaller value than DSMC over the fore body, but predicts a larger value over the rest of the sphere.

Computational Details

The computational details for the Mach 25 simulations in nitrogen are given in Tables 4.8 and 4.9.

Table 4.8: Computational Details for DSMC Mach 25 Simulations

Kn_∞	Cells	Particles	Time Steps	CPU Time [hrs]
0.002	1,240,876	237,527,176	347,000	33,696
0.01	103,985	14,213,372	150,000	1,152
0.05	19,311	5,849,453	120,000	232
0.25	6,113	4,459,637	110,000	192

Table 4.9: Computational Details for CFD Mach 25 Simulations

Kn_∞	Cells	Iterations	CPU Time [hrs]
0.002	100,000	29,209	1,152
0.01	84,000	14,747	384
0.05	45,000	16,392	144
0.25	45,000	21,329	112

4.4.3   Mach 45

The highest Mach number considered for this study is Mach 45. The results of the Mach 45 simulations in a flow of nitrogen with Knudsen numbers of 0.002 to 0.25 are discussed in more detail. The integrated drag and peak heat flux are given in Tables 4.10 and 4.11, respectively. The tables give the values predicted by DSMC and CFD along with a percent difference between the two methods. Again, it can be seen from the tables that the differences between CFD and DSMC grow with increasing Knudsen number. Comparing these results with those of Mach 10, Tables 4.2 and 4.3, and Mach 25, Tables 4.6 and 4.7, it can be observed that the percent differences are comparable for all three Mach numbers.

Table 4.10: Integrated Drag [N] (% difference) from DSMC and CFD at Mach 45

Kn_∞	Re_∞	DSMC	CFD (no-slip)	CFD (slip)
0.002	28,800	592	589(-0.51%)	588(-0.68%)
0.01	5,760	135	141(4.44%)	133(-1.48%)
0.05	1,150	35.0	45.1(28.9%)	35.6(1.71%)
0.25	230	8.23	19.3(135%)	11.1(34.9%)

Table 4.11: Peak Heating $\left[\frac{W}{m^2}\right]$ (% difference) from DSMC and CFD at Mach 45

Kn_∞	Re_∞	DSMC	CFD (no-slip)	CFD (slip)
0.002	28,800	1.58×10^7	1.57×10^7(-0.64%)	1.57×10^7(-0.64%)
0.01	5,760	6.84×10^6	7.55×10^6(10.5%)	7.14×10^6(4.41%)
0.05	1,150	2.59×10^6	3.29×10^6(27.1%)	3.11×10^6(20.1%)
0.25	230	6.70×10^5	1.24×10^6(85.3%)	9.02×10^5(34.6%)

The results of each Knudsen number are discussed in more detail in the following sections.

$\mathbf{Kn_\infty = 0.002}$

For this case, there is breakdown in the shock and wake of the flow as indicated by the contours of gradient length local Knudsen number, given in Fig. 4.26(a). From this figure it can be observed that the DSMC technique predicts a larger area of continuum breakdown than the CFD technique. It is interesting to note that the shock standoff distance is approximately the same in both methods. Comparing this case with the Mach 10 and Mach 25 cases, sections 4.4.1 and 4.4.2, it can be observed that the location of the shock remains unchanged but the area of breakdown is larger.

Even at a global Knudsen number of 0.002, the gradient length local Knudsen number along the surface is greater than the 0.05 limit, and therefore the flow at the surface is considered to be in continuum breakdown. Despite the flow at the surface being in continuum breakdown, the surface pressure coefficient, given in Fig. 4.26(b), is in perfect agreement between CFD and DSMC. In the inviscid limit the stagnation pressure coefficient is found to be 1.833, which compares well to the numerically found stagnation pressure coefficient of 1.855. The surface heat flux coefficient shows good agreement between CFD and DSMC with slight disagreement in the aft of the sphere,

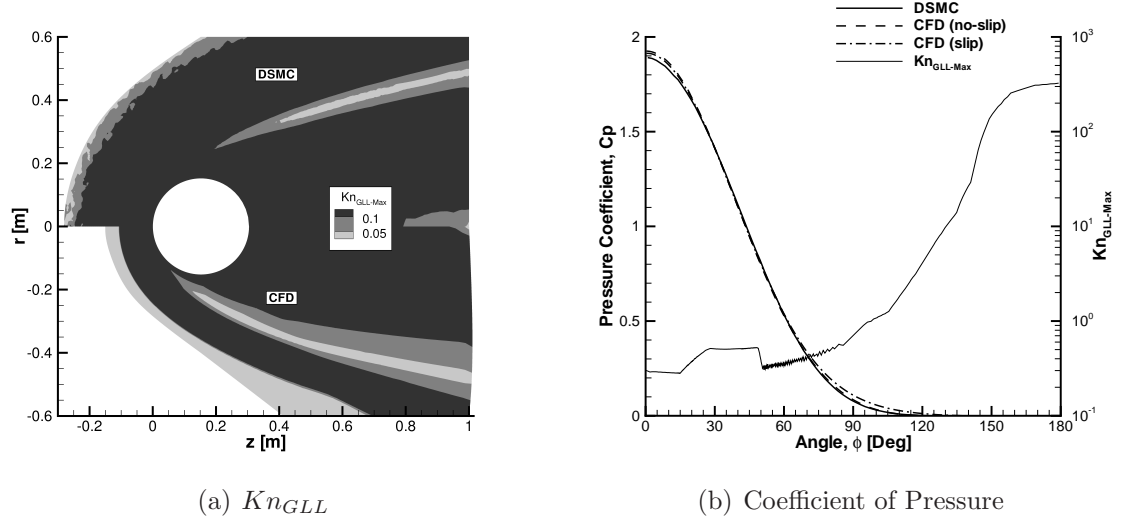(a) Kn_{GLL} (b) Coefficient of Pressure

Figure 4.26: $Kn_\infty = 0.002$, Kn_{GLL} and surface pressure (left axis) and Kn_{GLL} surface profile (right axis) on a sphere in a Mach 45 flow of nitrogen

as shown in Fig. 4.27(a). This is the same trend that is seen in the Mach 10 and Mach 25 cases. The surface shear stress, given in Fig. 4.27(b), displays good agreement between CFD and DSMC, with CFD over predicting DSMC over the aft of the sphere. The differences seen in the shear stress and heat flux coefficients over the aft of the sphere make sense because of the level of continuum breakdown.

$Kn_\infty = 0.01$

At a global Knudsen number of 0.01, there is breakdown in the shock and the wake of the flow as seen in Fig. 4.28(a), and again the flow from the shock all the way to the wall near the stagnation stream line is in continuum breakdown. From the figure it is seen that the amount of breakdown predicted by the DSMC method is larger in the shock region and in the wake than predicted by the CFD method. Comparing back to the Mach 10 and Mach 25 cases, it is again noticeable that the Mach 45 case predicts a larger amount of continuum breakdown in the flow field.

The surface pressure coefficient, given in Fig. 4.28(b), for DSMC and CFD match

(a) Coefficient of Heat Flux

(b) Coefficient of Shear Stress

Figure 4.27: Kn_∞=0.002, surface heat flux (left axis), surface shear stress (left axis) and Kn_{GLL} surface profile (right axis) on a sphere in a Mach 45 flow of nitrogen
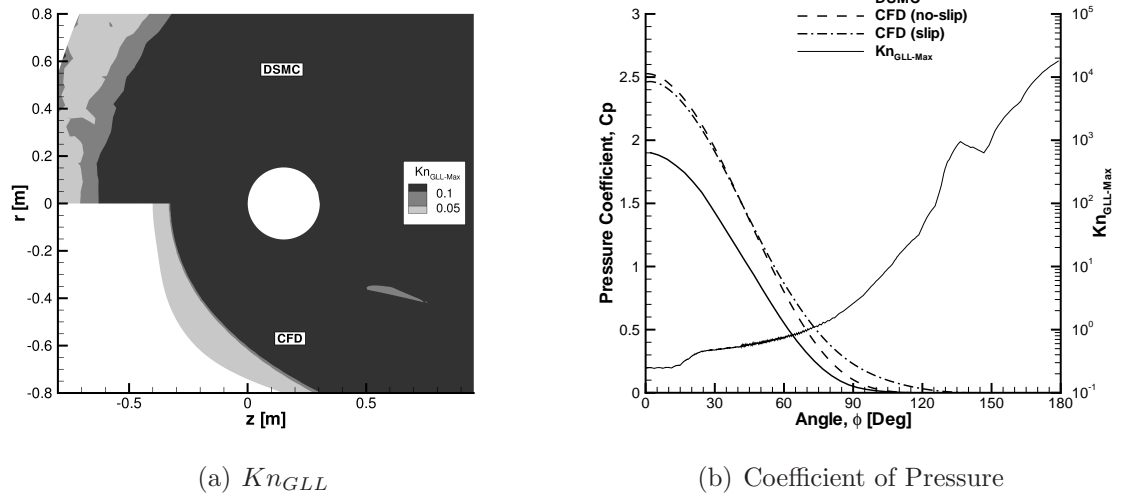

(a) Kn_{GLL}

(b) Coefficient of Pressure
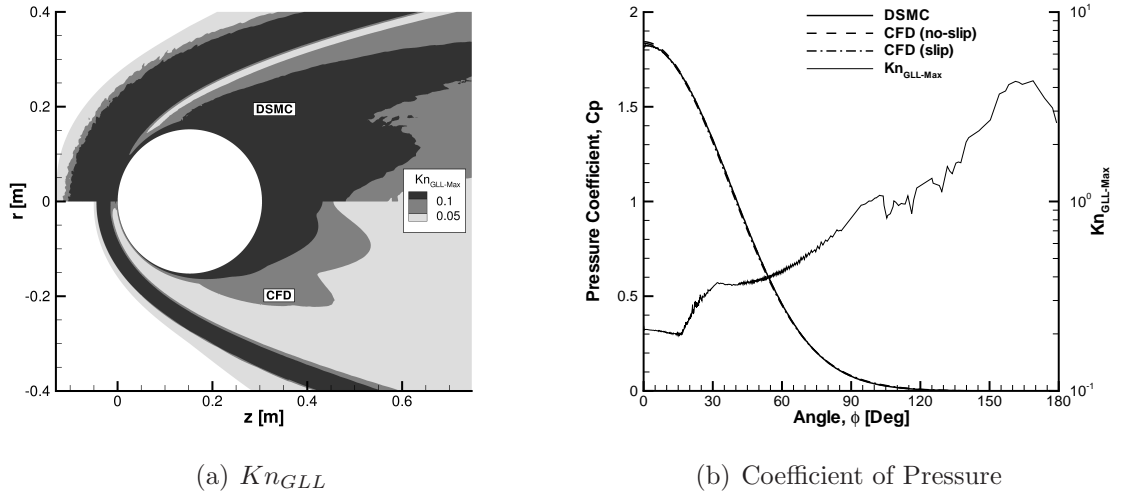
Figure 4.28: $Kn_\infty = 0.01$, Kn_{GLL} and surface pressure (left axis) and Kn_{GLL} surface profile (right axis) on a sphere in a Mach 45 flow of nitrogen

(a) Coefficient of Heat Flux
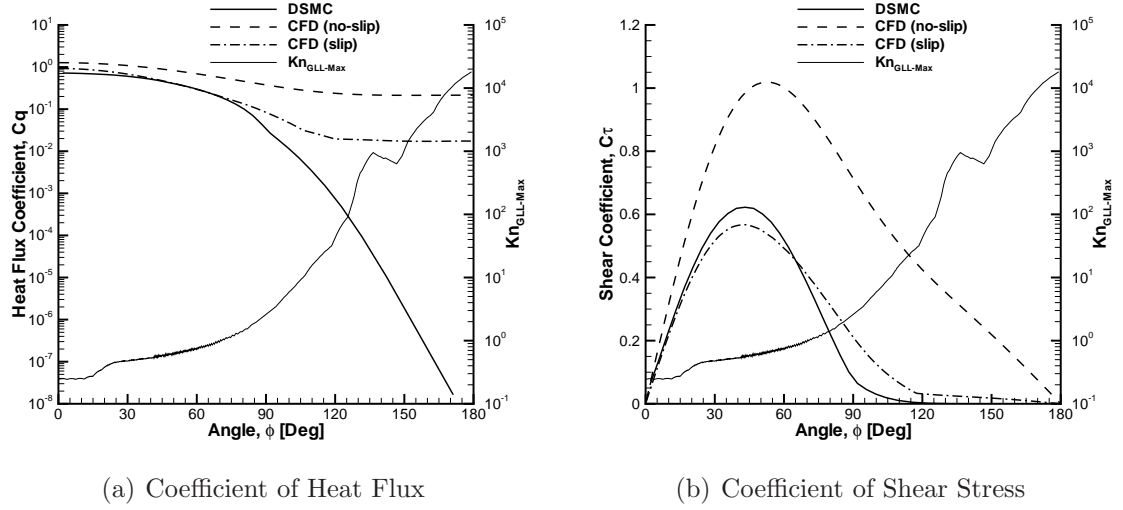
(b) Coefficient of Shear Stress
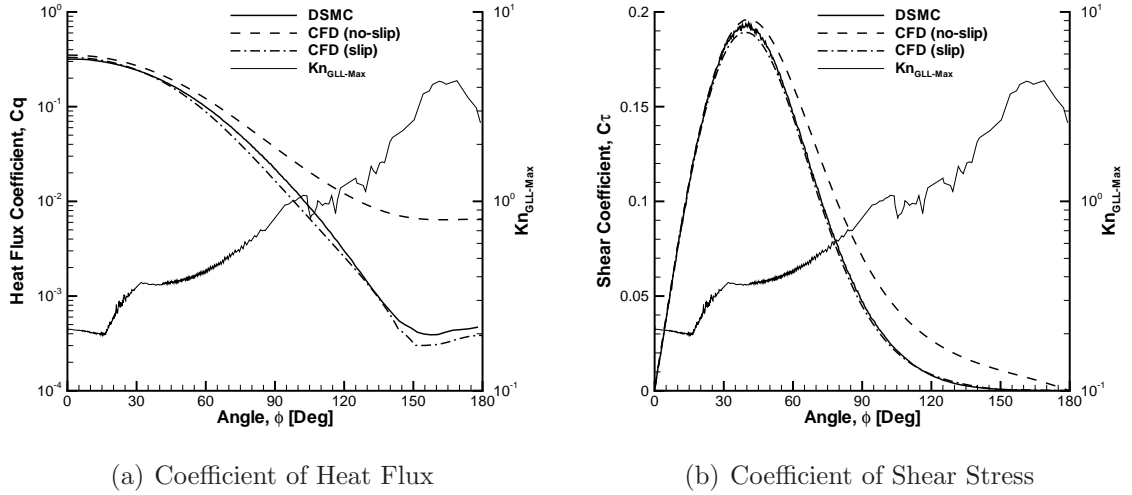
Figure 4.29: Kn_∞=0.01, surface heat flux (left axis), surface shear stress (left axis) and Kn_{GLL} surface profile (right axis) on a sphere in a Mach 45 flow of nitrogen

very well over the surface of the sphere. From this figure, it can also be seen that Kn_{GLL} is above the 0.05 limit for the whole surface, indicating that the flow is in continuum breakdown. The surface heat flux coefficient displays a gap between CFD with no-slip and DSMC over the entire surface of the sphere, as shown in Fig. 4.29(a). However, the use of the slip boundary condition improves the heat flux predicted by CFD and now matches much more closely with the heat flux predicted by DSMC. The surface shear stress, as given in Fig. 4.29(b), for CFD and DSMC agree well over the beginning of the sphere. The CFD shear stress has a higher magnitude at the peak, but both methods predict the peak at nearly the same location. After the peak, the CFD and DSMC predictions of the shear stress coefficient diverge. The slip boundary condition shows improved agreement between CFD and DSMC for the shear stress coefficient.

(a) Kn_{GLL} (b) Coefficient of Pressure
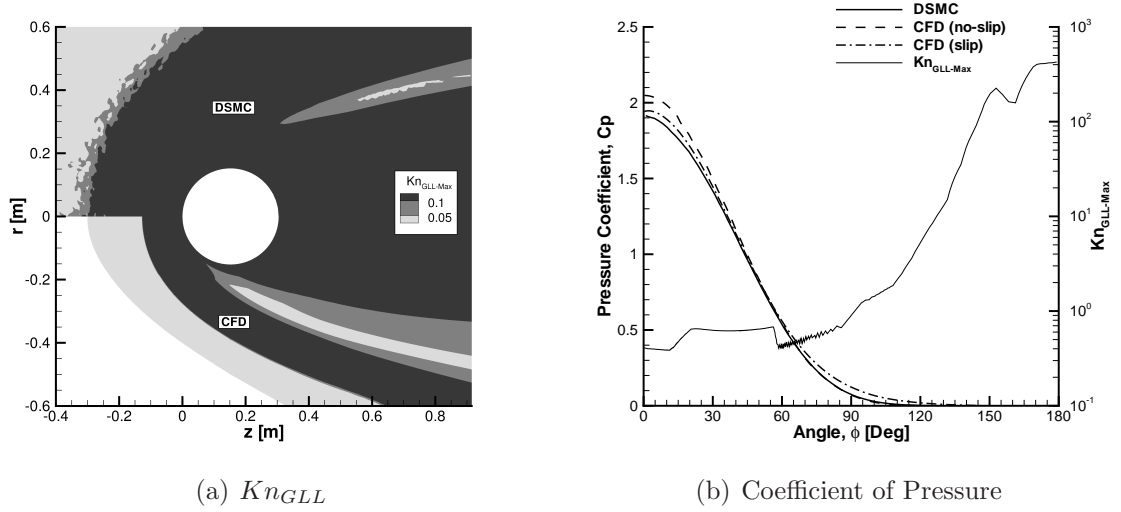
Figure 4.30: $Kn_\infty = 0.05$, Kn_{GLL} and surface pressure (left axis) and Kn_{GLL} surface profile (right axis) on a sphere in a Mach 45 flow of nitrogen

$Kn_\infty = 0.05$

At this global Knudsen number it can be seen from the contours of the gradient length local Knudsen number, shown in Fig. 4.30(a), that there is continuum breakdown occurring over most of the flow field. From the figure, it can be seen that the DSMC method predicts a larger amount of continuum breakdown than the CFD method. Also it can be observed, by comparing to the Mach 10 and Mach 25 cases, that the area of the flow field considered to be in breakdown has increased with increasing Mach number.

The CFD method over predicts the surface pressure coefficient as compared to DSMC, as shown in Fig 4.30(b). It is interesting to note that no-slip CFD predicts a stagnation pressure coefficient over 2, which did not happen with the two lower Mach number cases. The inclusion of a slip boundary condition into the CFD method improves the agreement with DSMC over the fore body of the sphere, but makes little difference over the backside of the sphere. The CFD method predicts a larger

(a) Coefficient of Heat Flux

(b) Coefficient of Shear Stress
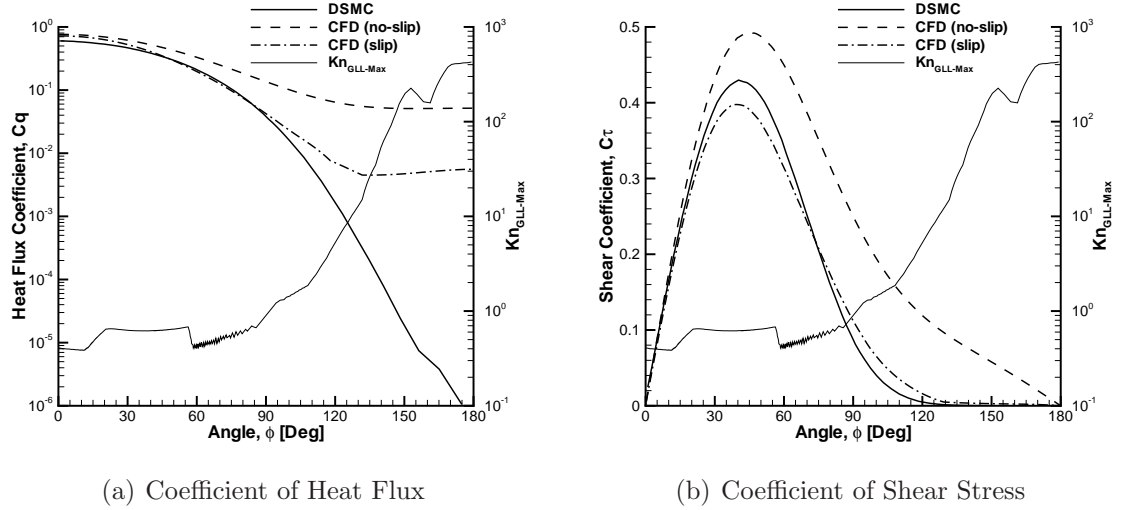
Figure 4.31: Kn_∞=0.05, surface heat flux (left axis), surface shear stress (left axis) and Kn_{GLL} surface profile (right axis) on a sphere in a Mach 45 flow of nitrogen

value than DSMC for the surface heat flux, shown in Fig. 4.31(a), over the entire surface, but the difference is most noticeable over the aft of the sphere. The heat flux calculated by the CFD method with a slip boundary condition improves the comparison with DMSC, but there is still a large difference over the aft of the sphere. The shear stress coefficient, given in Fig. 4.31(b), shows that CFD compares well with DSMC for the first 25 degrees, but then over predicts DSMC for the rest of the surface of the sphere. When slip boundary conditions are utilized in the CFD technique, the shear stress coefficient in lower than DSMC over the front of the sphere, but is higher than DSMC over the rest of the sphere. However, CFD with the slip boundary condition predicts the location of the peak shear to be approximately the same as DSMC.

Kn$_\infty$ = 0.25

From the gradient length local Knudsen number contours, given in Fig. 4.32(a), it can be seen that most of the flow is considered to be in continuum breakdown.

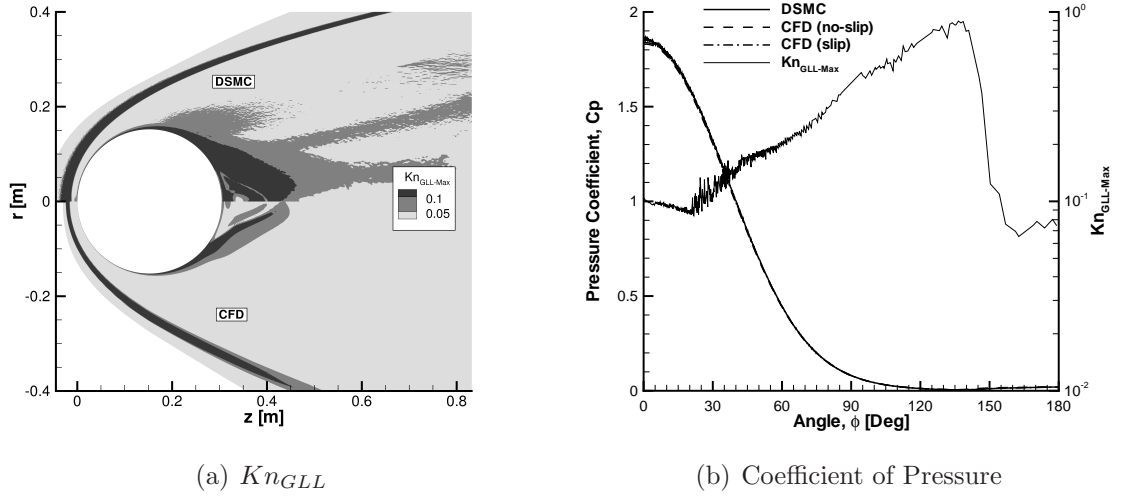(a) Kn_{GLL} (b) Coefficient of Pressure
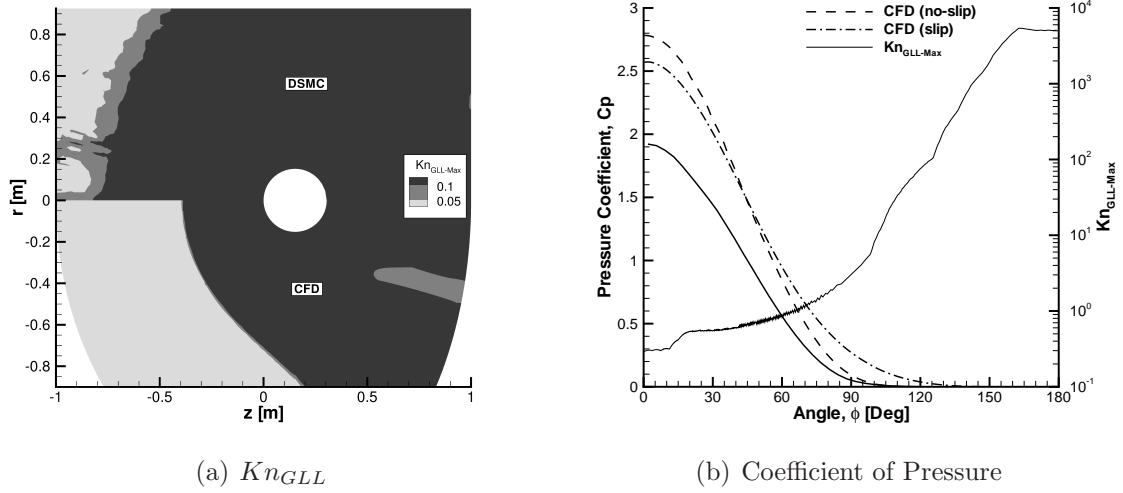
Figure 4.32: $Kn_\infty = 0.25$, Kn_{GLL} and surface pressure (left axis) and Kn_{GLL} surface profile (right axis) on a sphere in a Mach 45 flow of nitrogen

This is not a surprising outcome given that at this global Knudsen number the flow is considered to be in the rarefied regime. From the figure it is clear that the DSMC technique predicts a larger amount of breakdown than the CFD technique. Comparing to the Mach 10 and 25 cases, it can be observed that the shock has moved further away from the body causing the amount of continuum breakdown to increase. The shock front in this case is approximately 0.8 m in front of the body while it is approximately 0.4 and 0.6 m in the Mach 10 and 25 cases, respectively.

At this global Knudsen number, the pressure coefficient from CFD at the surface is in very poor agreement with DSMC, as shown in Fig 4.32(b). Evaluation in the free molecular limit gives the stagnation pressure coefficient to be 2.01, while at this condition the CFD method predicts the stagnation coefficient to be an unreasonable 2.8. The inclusion of a slip boundary condition in the CFD method does improve the agreement near the stagnation point, but makes it worse over the aft of the sphere. The surface heat flux coefficient, given in Fig 4.33(a), shows the CFD methods over predict DSMC over the entire surface of the sphere. There is an improvement

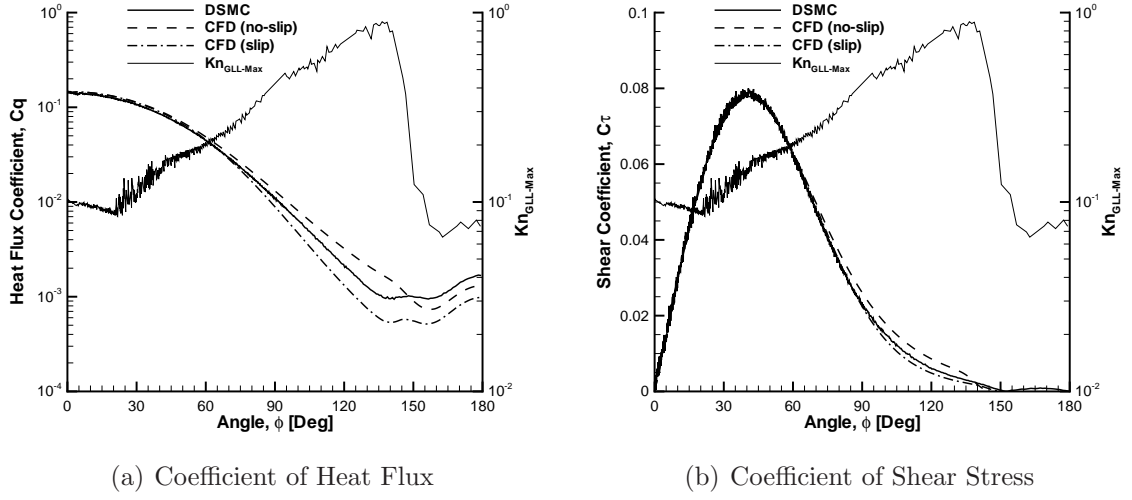(a) Coefficient of Heat Flux

(b) Coefficient of Shear Stress
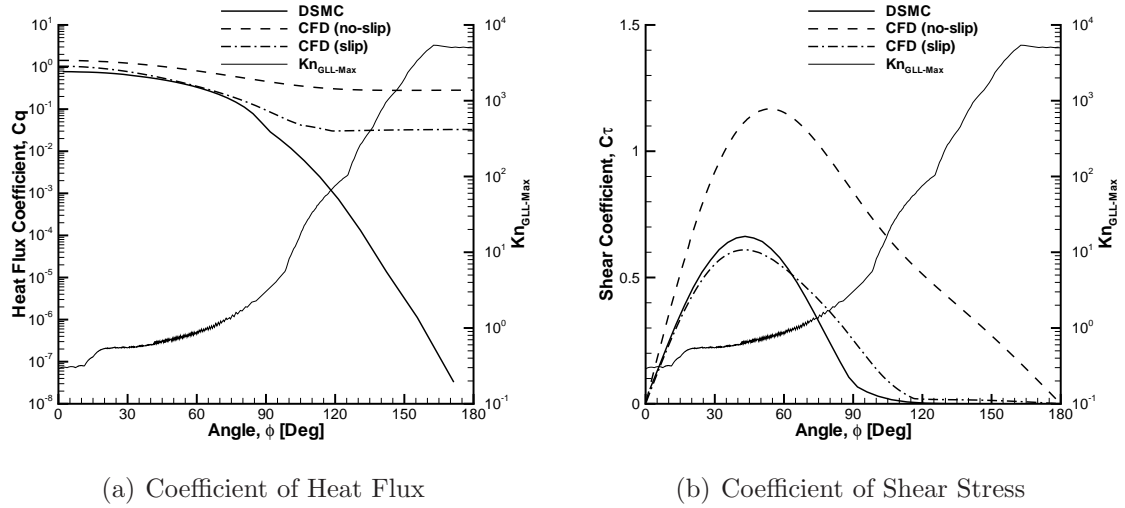
Figure 4.33: Kn_∞=0.25, surface heat flux (left axis), surface shear stress (left axis) and Kn_{GLL} surface profile (right axis) on a sphere in a Mach 45 flow of nitrogen

in the agreement with DSMC when the slip boundary condition is utilized in the CFD method, but there is still a large disagreement over the aft of the sphere. A theoretical calculation of stagnation point heat flux in the free molecular limit is found to be 0.998, which confirms the value found by DSMC of 0.78 is reasonable. The CFD method predicts the stagnation point coefficient to be an unreasonably high value of 1.44. Even with the slip boundary condition the CFD method still gives an unreasonable stagnation coefficient of 1.04. The CFD method over predicts the shear stress over the entire surface as compared to DSMC as shown in Fig. 4.33(b). When the slip boundary condition is utilized in the CFD method, the shear stress is lower than DSMC over the front of the sphere, but predicts a larger value than DSMC over the rest of the surface.

Even though the amount of continuum breakdown has increased with increasing Mach number, the differences in the surface properties between CFD and DSMC remain relatively constant. This behavior can be better understood by looking at
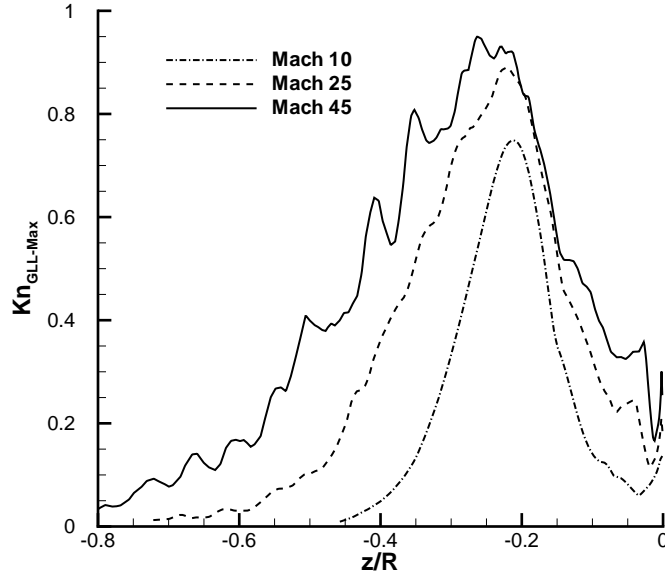
Figure 4.34: $Kn_\infty = 0.01$, Kn_{GLL} along the stagnation stream line for Mach 10, 25 and 45 in a flow of nitrogen

Kn_{GLL} along the stagnation streamline for the three Mach numbers at a Knudsen number of 0.01, as given in Fig. 4.34. From this figure it is seen that the region of continuum breakdown increases with Mach number, but Kn_{GLL} is not significantly changed. Continuum breakdown increases because the thickness of the shock increases, this is seen in the figure by the fact that the profile of Kn_{GLL} widens with increasing Mach number. It is interesting to note that the location of the shock remains relatively unchanged. This is most likely due to not including critical physics at these Mach numbers, such as chemical reactions.

Computational Details

The computational details for the Mach 45 simulations are given in Tables 4.12 and 4.13.

Table 4.12: Computational Details for DSMC Mach 45 Simulations

Kn_∞	Cells	Particles	Time Steps	CPU Time [hrs]
0.002	1,189,239	151,270,965	850,000	84,500
0.01	119,959	71,345,469	97,000	3,456
0.05	43,812	4,103,362	125,000	310
0.25	13,888	5,046,907	100,000	243

Table 4.13: Computational Details for CFD Mach 45 Simulations

Kn_∞	Cells	Iterations	CPU Time [hrs]
0.002	120,000	24,449	1,152
0.01	84,000	12,560	576
0.05	45,000	33,178	288
0.25	45,000	20,752	192

4.5   Comparison to Cylinder Flow

A further part of this study compares the results of the sphere with that of the analogous cylinder case. This is performed to compare the amount of continuum breakdown and the effects on the surface properties caused by changing the geometry. Since the main focus of this study is on the sphere, only one case is employed to make a comparison to the cylinder. The case chosen for this comparison is the global Knudsen number of 0.01 case at Mach 10. The integrated drag and peak heat flux are given in Tables 4.14 and 4.15, respectively. The tables give the values predicted by DSMC and CFD along with a percent difference between them.

Table 4.14: Integrated Drag [N], $\left[\frac{N}{m}\right]$ for cylinder, for DSMC and CFD for a Knudsen Number of 0.01 and a Mach number of 10

	DSMC	CFD	Percent Difference
Cylinder	34.0	33.8	-0.59%
Sphere	6.42	6.60	2.78%

Table 4.15: Peak Heating $\left[\frac{W}{m^2}\right]$ for DSMC and CFD for a Knudsen Number of 0.01 and a Mach number of 10

	DSMC	CFD	Percent Difference
Cylinder	3.20×10^4	3.23×10^4	1.12%
Sphere	4.71×10^4	5.27×10^4	11.89%

From the integrated drag and the peak heat flux it can be seen that running a simulation axisymmetrically leads to larger differences between DSMC and CFD. So the question becomes, how does axisymmetry affect continuum breakdown? This question can be answered by comparing the plots of Kn_{GLL} for the sphere and cylinder cases, obtained with DSMC and CFD, as presented in Fig. 4.35. It is seen that the DSMC prediction of Kn_{GLL} shows a slighly larger amount of continuum breakdown in the wake of the sphere than for the cylinder. The CFD prediction of Kn_{GLL} remains nearly the same for both the sphere and the cylinder. The shock in the cylinder case is farther out than for the sphere, but this is expected due to the ability of gas to flow in all directions around the sphere thus allowing the shock to move closer to the surface.

Figure 4.36 gives the temperature and Kn_{GLL} profiles along the stagnation stream line for the sphere and the cylinder. From this figure it is seen that the flow is in continuum breakdown from the shock to the surface for the sphere, while for the

(a) DSMC   (b) CFD
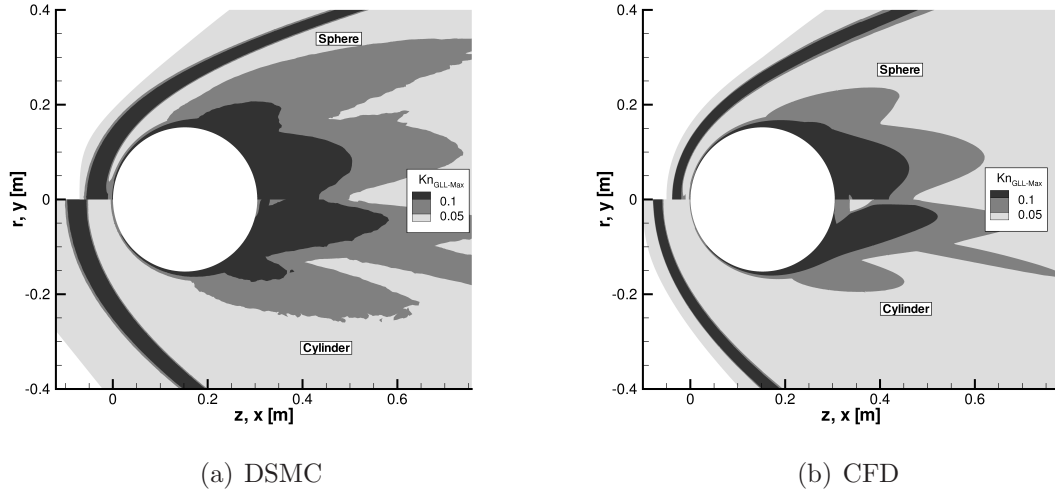
Figure 4.35: $Kn_\infty = 0.01$, Kn_{GLL} from DSMC and CFD in a Mach 10 flow of nitrogen over a sphere and a cylinder

cylinder there is only breakdown in the shock and in the boundary layer. Since there is less breakdown for the cylinder case, the temperature profiles for CFD and DSMC match very well. The only difference in the temperature profiles for the cylinder is that the shock is thicker in DSMC so the temperatures begin increasing slightly farther upstream than CFD. Also, notice that the rotational temperature predicted by CFD does not overshoot the DSMC solution as it does with the sphere.

It appears that the Knudsen number fails as an approach to determine the level of continuum breakdown for a sphere and a cylinder. It is not surprising the sphere and cylinder cases give different results given the different shapes; one is a two dimensional cylinder with no edge effects and the other is a three dimensional sphere. The problem with Knudsen number is that is only takes into account a one dimensional length, this study highlights differences seen in three dimensions. It would make more sense to use a characteristic area rather than a characteristic length. This study suggests the use of an area Knudsen number,

(a) Sphere   (b) Cylinder
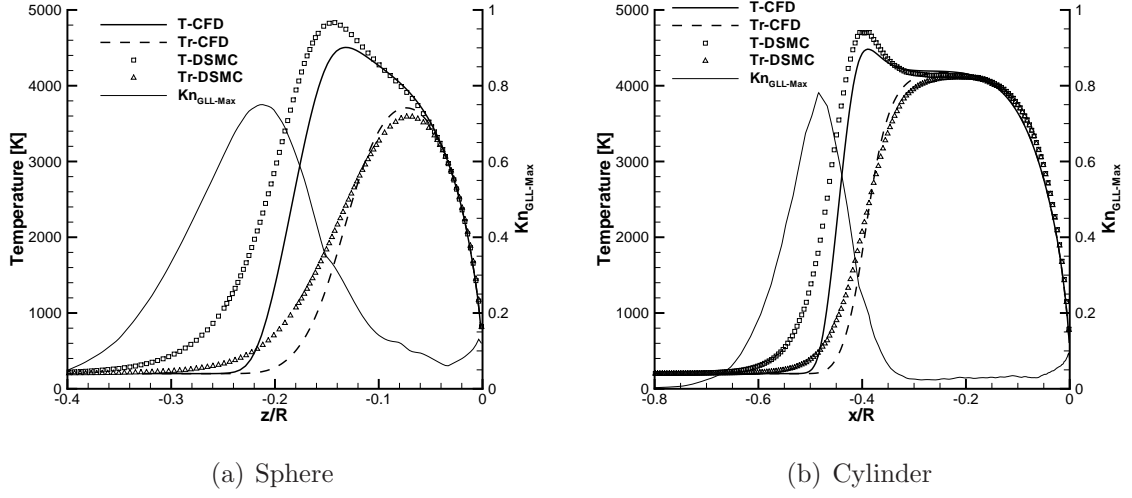
Figure 4.36: $Kn_\infty = 0.01$, Temperature and Kn_{GLL} profiles along the stagnation stream line at Mach 10

$$Kn_A = \frac{\lambda^2}{A} \qquad (4.10)$$

where λ is the mean free path, and A is a characteristic area. The area, in this case, is selected to be the surface area of the object. The area Knudsen numbers for the sphere and cylinder cases are 9.70×10^{-6} and 3.18×10^4, respectively. Setting the area Knudsen number for the cylinder equal to that of the sphere, an adjusted Knudsen number for the cylinder is found to be 0.033. Instead of simulating an additional cylinder case, the present Knudsen number 0.01 sphere case is compared to the Knudsen number 0.05 cylinder case performed by Lofthouse[15]. Lofthouse obtained differences of 5.6% and 13/7% for integrated drag and peak heating flux, respectively, on a cylinder at a Knudsen number of 0.05. These values compare better with the present sphere case at a Knudsen number of 0.01 instead of 0.05, providing partial support for the area based Knudsen number concept. Also, the amount of continuum breakdown seen in the flow field of the Knudsen number 0.05 cylinder compares better with the Knudsen number 0.01 sphere case, given in Fig. 4.36.

The use of an area based Knudsen number is promising, but needs to be further investigated.

4.6   Summary: Comparison of Non-Reacting Nitrogen Flow

A comparison of the rotational energy model in the CFD and DSMC methods was performed by comparing the temperature profiles along the stagnation stream line for several different flow conditions. At lower Mach numbers and Knudsen numbers it is found that the temperature profiles from DSMC and CFD agree very well. As the Mach number or Knudsen number are increased the agreement grows worse, but it is found that this is not caused by problems with the rotational energy model. The studies showed that CFD with a separate rotational energy and DSMC match well, with differences appearing due to thermal nonequilibrium near the wall.

A study comparing the three slip boundary condition models was conducted at Mach 10 and a Knudsen number of 0.01 in a flow of nitrogen. It was performed using both DSMC and CFD to determine which model is to be utilized for this study. It was seen that all slip boundary conditions improve the agreement with DSMC, but on closer inspection the Gökçen slip boundary condition provides the best agreement. Another study was performed on the effects of the slip boundary condition on the convergence and flow field. It is found that in all cases slip boundary conditions improved the agreement with DSMC.

This chapter discussed the effects of continuum breakdown on the surface aerothermodynamic properties (pressure, stress, heat transfer rate) of a sphere in Mach 10, 25, and 45 flows of nitrogen gas in regimes varying from continuum to a rarefied gas flow.

The differences between CFD and DSMC for peak heat flux and the integrated

drag increased for global Knudsen numbers increasing from 0.002 to 0.25. At low Knudsen numbers, where the flow is expected to be in the continuum regime, the aerothermodynamic properties are very similar between CFD and DSMC. It was observed that with increasing global Knudsen number, the amount of continuum breakdown increased and this had a large effect on the surface properties of the sphere. It is clear that continuum breakdown affects surface properties, but the effects are much less noticeable on the surface pressure than on shear stress or heat flux. The reason for this is because the heat flux and shear stress are dependent on gradients calculated at the wall, where as pressure is calculated from primitive variables, temperature and density, that does not require additional gradients. These gradients are always higher in CFD, with no-slip boundary conditions, than DSMC. However, slip boundary conditions lower the gradients at the wall giving better comparisons to DSMC. This is also the reason CFD with no-slip always over predicts peak heating and integrated drag when compared to DSMC.

As Mach number was increased, the amount of continuum breakdown also increased, but there were no clear effects on the surface properties. Even though the amount of continuum breakdown increased with Mach number, the value of Kn_{GLL} remained relatively constant causing the differences in the surface properties between CFD and DSMC to be nearly unchanged. The slip boundary conditions improved the agreement between CFD and DSMC for all three Mach numbers.

The last part of this chapter compared the results of the sphere with the analogous case of a two dimensional cylinder for a global Knudsen number of 0.01 at Mach 10. The integrated drag and peak heat flux both show that the differences between CFD and DSMC increase for a sphere in comparison to a cylinder. For DSMC, the amount of continuum breakdown slightly increased when run for the sphere as compared to

the cylinder, although this trend is not observed in CFD. A new area Knudsen number was introduced and it was utilized to display the differences between the cylinder and sphere cases.

CHAPTER V

Investigation of Reacting Flow

5.1 Introduction

Chapter IV discussed the effects of continuum breakdown over a 12 inch sphere in a hypersonic flow of nitrogen. It was seen that temperatures reached levels where dissociation would occur in the flow, but chemical reactions were ignored to be able to focus on the effects of thermal nonequilibrium. This chapter continues to explore the effects of continuum breakdown on the surface properties of a 12 inch sphere. The previous work focused on single species gas simulations, this study adds the complexity of multiple species. Since there are multiple species now being simulated, reacting flow can also be considered. This adds the complexity of thermo-chemical nonequilibrium. This chapter examines the continuum breakdown in a Mach 25 flow of reacting nitrogen and reacting air.

The simulations are performed using two different numerical methods. First, the Navier-Stokes equations are numerically solved using the LeMANS CFD code. For the LeMANS simulations, a grid convergence study is conducted to determine the final mesh utilized for each case. Second, the DSMC solutions are provided by the MONACO code. All DSMC meshes are refined by hand so that the cell size is of the order of a mean free path. The grids utilized for the DSMC simulations are a hybrid

mesh, where the structured cells are stretched near the stagnation point.

The results of the surface aerothermodynamic properties that are presented in this chapter are given as non-dimensionalized coefficients, which were defined in section 4.1. The surface properties are plotted against the surface angle ϕ, which is measured from the stagnation point.

This chapter is presented in two sections. This first section presents and discusses the results of reacting nitrogen flow and how it compares to non-reacting nitrogen flow over a Mach 25 sphere. The non-reacting nitrogen flow has already been discussed in section 4.4.2. The second section discusses the results of reacting air flow over a Mach 25 sphere.

5.2   Nitrogen Flow

The first part of this chapter examines continuum breakdown in Mach 25 flows of reacting nitrogen over a 12 inch diameter sphere. The free stream temperature is 200 K giving a free stream velocity of 7209 m/s. The surface of the sphere has a fixed temperature of 1500 K. The density of the free stream is varied to change the global Knudsen number of the flow from continuum to a rarefied gas as given in Table 5.1. The Knudsen number is calculated using the diameter of the sphere as the characteristic length and the hard sphere model to calculate the mean free path, as given in section 4.1.

Table 5.1: Simulated reacting nitrogen flow regimes

Kn_∞	Mass Density (kg/m^3)	Number Density $(particles/m^3)$	Mean Free Path (m)
0.002	9.875×10^{-5}	2.124×10^{21}	6.096×10^{-4}
0.01	1.975×10^{-5}	4.247×10^{20}	3.048×10^{-3}
0.05	3.949×10^{-6}	8.494×10^{19}	1.524×10^{-2}
0.25	7.899×10^{-7}	1.699×10^{19}	7.620×10^{-2}

5.2.1 Mach 25

The results for a Mach 25 reacting nitrogen flow at various global Knudsen numbers are discussed and compared to cases without chemical reactions, which were discussed in section 4.4.2. The reason for this is to be able to discern the effects of including reacting flow on continuum breakdown and the surface properties. This case involves two reactions for the dissociation and recombination of nitrogen. The dissociation reactions and the reaction rate coefficients are given in Appendix A.3. These rate coefficients are utilized in the VFD model to calculate the forward reaction rates in DSMC, while CFD employs the modified Arrhenius form with a preferential dissociation model to calculate forward reaction rates, as discussed in Chapter III. In both numerical methods, the backward reaction rates are calculated using the equilibrium constant found with Park's equilibrium model[66]. For this study, both numerical techniques use non-catalytic, fully diffuse wall conditions. In the next section, more complexity is incorporated with additional species and reactions. The integrated drag and the peak heat flux values predicted by DSMC and CFD, with and without slip boundary conditions, are given in Tables 5.2 and 5.3.

From Table 5.2 it appears that the inclusion of reacting flow has decreased the integrated drag. For the reacting simulations, the transport properties model is

switched from a VHS viscosity model with Eucken's relation to Gupta's mixing rule with collision integral data in the CFD method. In the DSMC method, new VHS parameter values are found to match the collision integral data for the reacting flow simulations, as discussed in chapter III. The new VHS parameters for molecular and atomic nitrogen are given in Appendix A.4. It was not anticipated that these modifications would cause any change in the surface properties. However, CFD simulations of non-reacting nitrogen flow using Gupta's mixing rule for Knudsen numbers of 0.01 and 0.05 prove that these modifications do have an impact on the surface properties. The integrated drag for the Knudsen number 0.05 case is calculated to be 11.6 N. This is lower than the non-reacting CFD simulation using the VHS model but is equal to the CFD simulation with reacting flow. Since there is essentially no chemistry occurring at a Knudsen number of 0.05, the decrease in the drag is due to the use of Gupta's mixing model and not reacting flow. The integrated drag for the Knudsen number 0.01 case is predicted by CFD to be 41.1 N, which is lower than the non-reacting CFD simulation using the VHS model. Again, this decrease is caused by the change in the way the transport properties are calculated. However, there are chemical reactions occurring in this case. This means that the decrease is drag observed was not caused by reacting flow, but rather the change in the transport property model. This can be further observed in Fig. 5.1, which gives the coefficient of viscosity calculated from the two different methods; the VHS viscosity model and Gupta's mixing rule with collision integrals. It can be seen from this figure that the VHS model predicts a higher viscosity coefficient which leads to higher drag values. From this table it can be observed that the percent differences between CFD and DSMC remain relatively constant for the reacting and non-reacting cases across the range of Knudsen numbers.
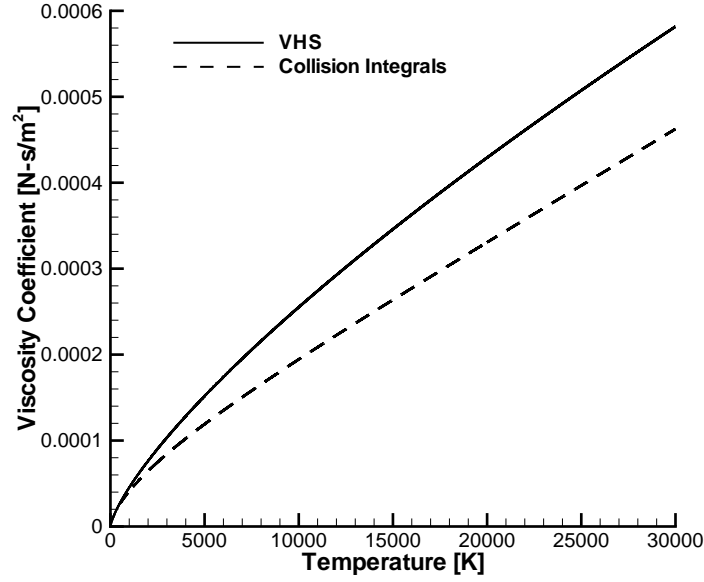
Figure 5.1: Coefficient of Viscosity for Nitrogen gas as a Function of Temperature

Table 5.2: Integrated Drag [N] (% difference) from DSMC and CFD at Mach 25; grayed rows are without reactions

Kn_∞	Transport Model	DSMC	CFD (no-slip)	CFD (slip)
0.002	Gupta	180	179(-0.55%)	179(-0.55%)
0.002	VHS	180	181(0.55%)	181(0.55%)
0.01	Gupta	40.2	41.1(2.19%)	40.3(0.25%)
0.01	VHS	41.2	42.4(2.91%)	40.3(-2.18%)
0.01	Gupta	—	41.1	—
0.05	Gupta	9.93	11.6(16.8%)	9.81(-1.18%)
0.05	VHS	10.5	13.0(23.8%)	10.8(2.78%)
0.05	Gupta	—	11.6	—
0.25	Gupta	2.48	4.54(82.8%)	2.14(-13.7%)
0.25	VHS	2.46	5.24(113%)	3.20(30.1%)

In Table 5.3, it can be seen that including reacting flow, in general, lowers the peak heating. The behavior of the peak heating is an expected trend for a non-

catalytic wall: it takes energy for a reaction to occur lowering the energy in the flow and causing a decrease in the peak heating. However, it is observed that the transport property model caused a portion of the reduction in the peak heating. The peak heating predicted by CFD at a Knudsen number of 0.05 with Gupta's mixing rule without chemical reactions is $4.32 \times 10^5\ W/m^2$, which is lower than the value predicted by CFD without chemical reactions, but equal to the value predicted by CFD with chemical reactions, as seen in Table 5.3. Hence, the decrease in the peak heat flux is caused by the switch to Gupta's mixing rule with collision integral data and not chemical reactions. The peak heating predicted by CFD at a Knudsen number of 0.01 with Gupta's mixing rule without chemical reactions is 9.93×10^5 W/m^2. This is lower than the value predicted by CFD without chemistry, but higher than CFD with chemistry. In this case, there are two reasons for the decrease in peak heating; a portion of the decrease in the peak heating is caused by the change in the transport property model, and a secondary cause can be attributed to chemical reactions occurring in the flow. A separate figure for thermal conductivity is not included because it has the same trends as viscosity. Therefore, looking at Fig. 5.1, it can be seen that Gupta's Mixing model with collision integral data gives lower thermal conductivity, which leads to lower heat flux values. It can be seen that the differences between CFD and DSMC are similar with and without reacting flow across the range of Knudsen numbers.

Table 5.3: Peak Heating $\left[\frac{W}{m^2}\right]$ (% difference) from DSMC and CFD at Mach 25; grayed rows are without reactions

Kn_∞	Transport Model	DSMC	CFD (no-slip)	CFD (slip)
0.002	Gupta	1.15×10^6	$1.19\times10^6(3.78\%)$	$1.17\times10^6(2.17\%)$
0.002	VHS	2.14×10^6	$2.20\times10^6(2.92\%)$	$2.18\times10^6(1.82\%)$
0.01	Gupta	8.26×10^5	$9.64\times10^5(16.8\%)$	$9.24\times10^5(11.9\%)$
0.01	VHS	9.81×10^5	$1.08\times10^6(10.2\%)$	$1.03\times10^6(4.87\%)$
0.01	Gupta	—	9.93×10^5	—
0.05	Gupta	3.56×10^5	$4.32\times10^5(21.4\%)$	$3.52\times10^5(-1.12\%)$
0.05	VHS	3.92×10^5	$4.90\times10^5(25.0\%)$	$4.59\times10^5(17.1\%)$
0.05	Gupta	—	4.32×10^5	—
0.25	Gupta	1.04×10^5	$1.67\times10^5(60.7\%)$	$7.86\times10^4(-24.4\%)$
0.25	VHS	1.06×10^5	$1.88\times10^5(76.9\%)$	$1.36\times10^5(28.4\%)$

From these tables it can be seen that the comparisons between CFD and DSMC diverge with growing global Knudsen number. In the following subsections, the surface properties and gradient length local Knudsen number are discussed in more detail for each case.

$\text{Kn}_\infty = 0.002$

At a global Knudsen number of 0.002, the flow is expected to be in the continuum regime, but there are still regions of continuum breakdown in the shock and wake of the flow as shown in Fig. 5.2. This figure gives the contours of Kn_{GLL} with reacting flow, shown as flooded contours, along with the contours without reacting flow, given as contour lines. From this figure it can be seen that there is a difference in Kn_{GLL} between nitrogen flow with and without chemical reactions seen in the shock. Dissociation occurring in the flow has caused the shock to move closer to the body. However, this has not significantly changed the area of continuum breakdown

observed. The data seen in Tables 5.2 and 5.3 can be explained by the fact that the amount of breakdown has not significantly changed with the inclusion of chemistry.

The surface profile of the coefficient of pressure and the gradient length local Knudsen number is given in Fig. 5.3(a). From the Kn_{GLL} profile on the surface it can be seen that the critical value of 0.05 is broken for most of the surface, indicating the flow at the surface is in breakdown. From the surface pressure profiles it can be observed that there is near perfect agreement between CFD and DSMC, despite the breakdown on the surface. The surface heat flux coefficient is given in Fig. 5.3(b). From this figure it can be seen that CFD compares well with DSMC over the fore body of the sphere, but shows some disagreement over the aft of the vehicle. The surface shear stress, given in Fig. 5.3(c), displays good agreement between CFD and DSMC, except CFD under predicts the peak shear stress as compared to DSMC. It can be seen from the pressure, heat flux and shear stress that CFD with a slip boundary condition shows improved agreement in the aft of the sphere, where continuum breakdown is more prevalent.

To determine the level of chemistry occurring in the flow, the mass fractions along the stagnation streamline of each species are given in Fig. 5.4(a). In this case there is significant dissociation of molecular nitrogen following the shock, as can be seen by the dip in the mass fraction to 0.7. From the figure it can be seen that the mass fractions predicted by the two methods compare well. A small increase in the mass fraction of molecular nitrogen in the DSMC method near the wall can be observed, while in CFD this is not seen. However, the peak mass fraction of atomic nitrogen compares well between the two numerical methods. The difference in the atomic nitrogen mass fraction in front of the shock is caused by diffusion of trace species in DSMC. It is unclear if this diffusion may be a physical phenomenon or

Figure 5.2: $Kn_\infty = 0.002$, Kn_{GLL} contours from DSMC (top) CFD (bottom) with reacting flow (flooded contours) and without reacting flow (contour lines)
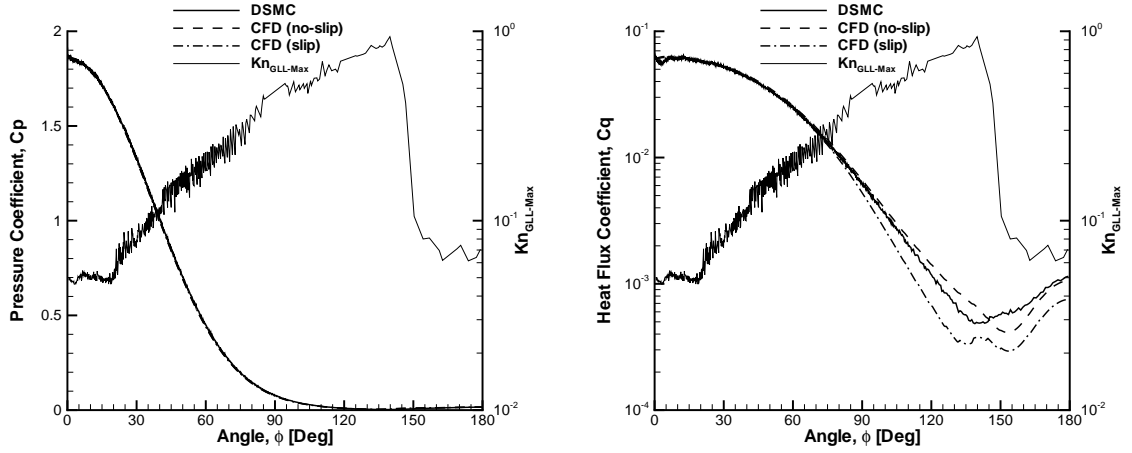
(a) Coefficient of Pressure

(b) Coefficient of Heat Flux
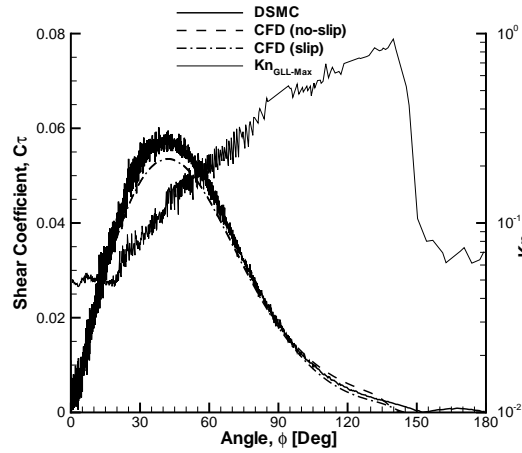
(c) Coefficient of Shear Stress

Figure 5.3: $Kn_\infty = 0.002$, surface pressure (left axis), surface heat flux (left axis), surface shear stress (left axis) and Kn_{GLL} surface profile (right axis) on a sphere in a Mach 25 flow of reacting nitrogen

(a) Mass Fraction   (b) Temperature
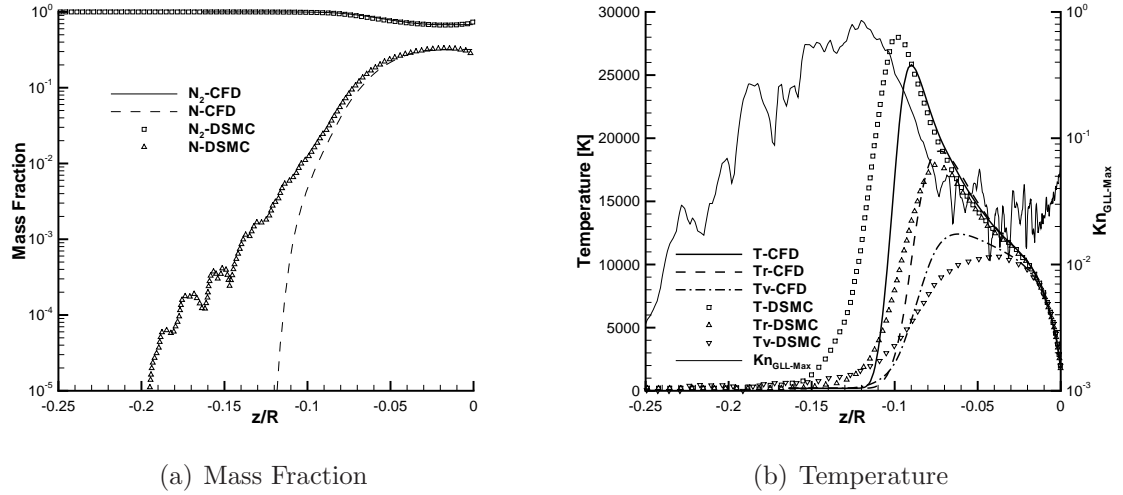
Figure 5.4: $Kn_\infty = 0.002$, mass fraction (left axis), temperature (left axis) and Kn_{GLL} (right axis) profiles along the stagnation streamline in a Mach 25 flow of reacting nitrogen

caused by problems with how DSMC deals with trace species. The temperature and gradient length local Knudsen number profiles along the stagnation streamline are given in Fig. 5.4(b). It can be observed that the translational temperature matches well between the two numerical techniques. However, the rotational and vibrational temperatures do not match as well. The over prediction of rotational and vibrational temperatures by CFD as compared to DSMC is an expected result, caused by thermal nonequilibrium. From the profile of Kn_{GLL} it is seen that the flow is expected to be in the continuum regime as it approaches the wall.

$\mathbf{Kn_\infty = 0.01}$

The gradient length local Knudsen number contours for DSMC and CFD are given in Fig. 5.5. This figure gives the contours of Kn_{GLL} for the simulation with reacting flow, shown as flooded contours, along with the contours without reacting flow, given as contour lines. This figure also includes the contours of Kn_{GLL}, given as dashed line contours, for the CFD simulation without reacting flow, and the transport

properties are calculated utilizing Gupta's mixing rule with collision integral data as opposed to the VHS model that was employed for the non-reacting simulations. It can be observed that the area of continuum breakdown has decreased with reacting flow. However, it can be seen that the simulation utilizing Gupta's mixing rule with collision integral data predicts the same amount of continuum breakdown, except in the shock. It can be observed that the shock has moved closer to the body, and this is due to chemical reactions occurring in the flow. At this Knudsen number, the change in the amount of continuum breakdown is due to chemical reactions as well as the change in the transport property model.

The pressure coefficient over the surface of the sphere is given in Fig. 5.6(a), along with the surface profile of Kn_{GLL}. From the figure it can be seen that the gradient length local Knudsen number is above the threshold value of 0.05 everywhere, indicating that the flow is in breakdown. However, the surface pressures predicted by the two methods still agree well. The surface heat flux coefficient is given in Fig. 5.6(b). The CFD with no-slip boundary conditions predicts a higher heat flux over the entire surface. This is not surprising given the entire surface is considered to be in breakdown. However, slip boundary conditions in CFD improve the heat flux prediction in comparison to DSMC. The shear stress coefficient, given in Fig. 5.6(c), displays good agreement between the two techniques. There is a slight divergence over the aft of the sphere from the results predicted by CFD with the no-slip boundary condition. The implementation of a slip boundary condition in the CFD method improves the agreement with DSMC.

To determine the level of chemistry occurring in the flow, the mass fractions of each species along the stagnation streamline are given in Fig. 5.7(a). The large discrepancies between CFD and DSMC in mass fraction for atomic nitrogen that
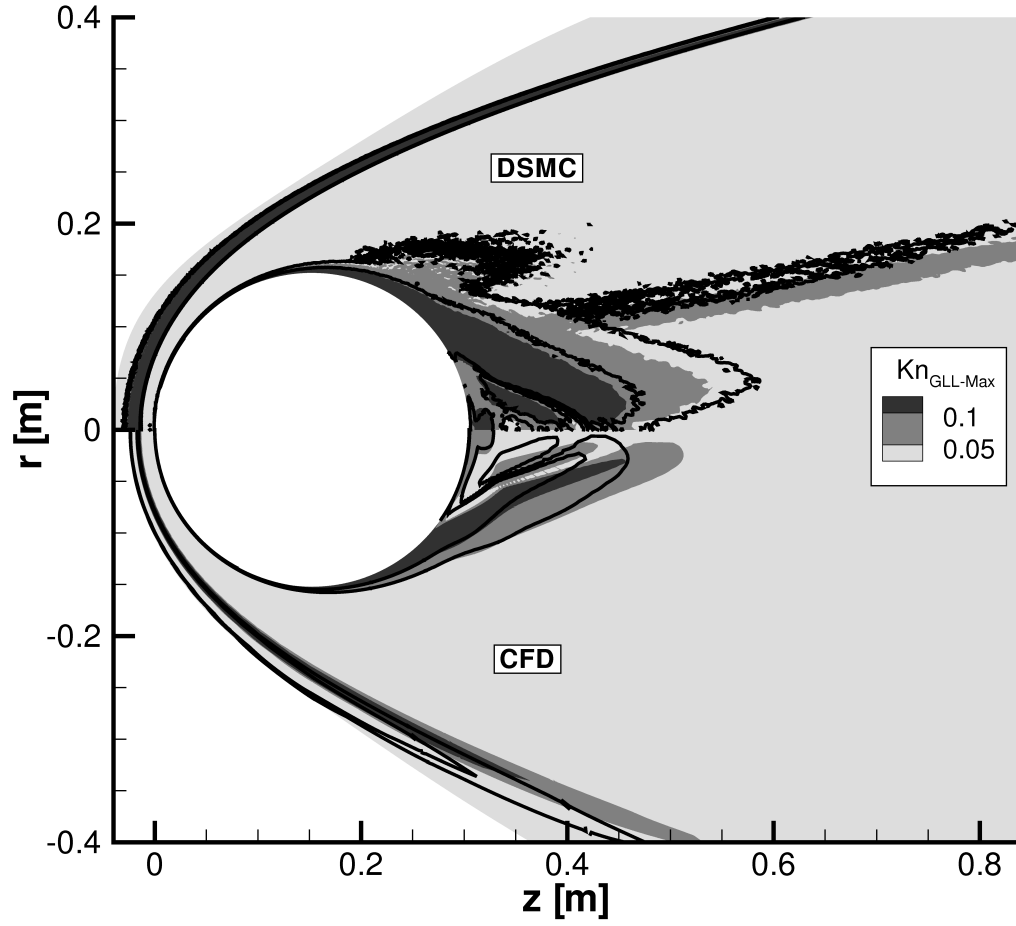
Figure 5.5: $Kn_\infty = 0.01$, Kn_{GLL} contours from DSMC (top) and CFD (bottom) with reacting flow (flooded contours) and without reacting flow (line contours), and CFD with Gupta's mixing rule (dashed line contours)
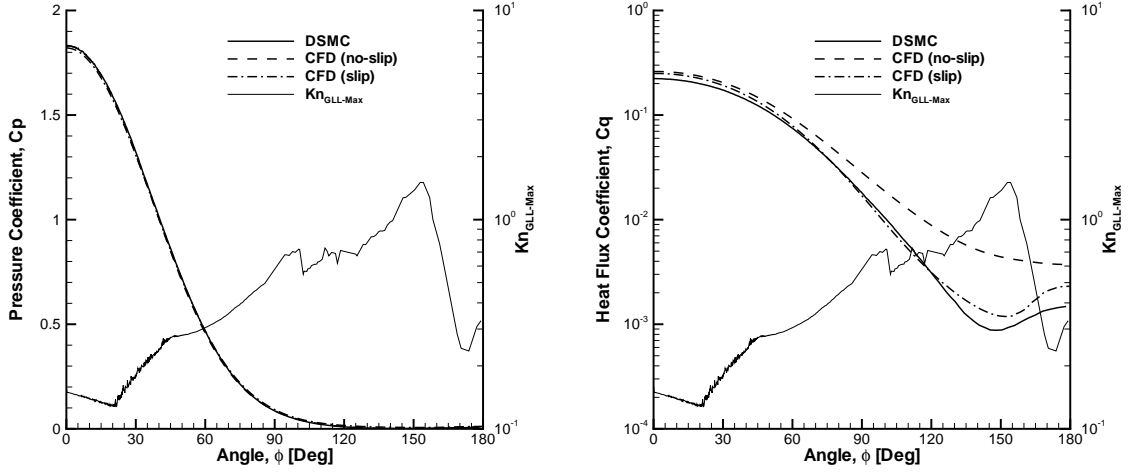
(a) Coefficient of Pressure

(b) Coefficient of Heat Flux
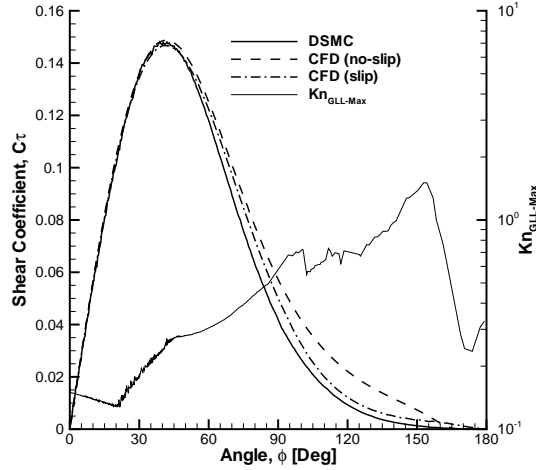
(c) Coefficient of Shear Stress

Figure 5.6: $Kn_\infty = 0.01$, surface pressure (left axis), surface heat flux (left axis), surface shear stress (left axis) and Kn_{GLL} surface profile (right axis) on a sphere in a Mach 25 flow of reacting nitrogen

(a) Mass Fraction
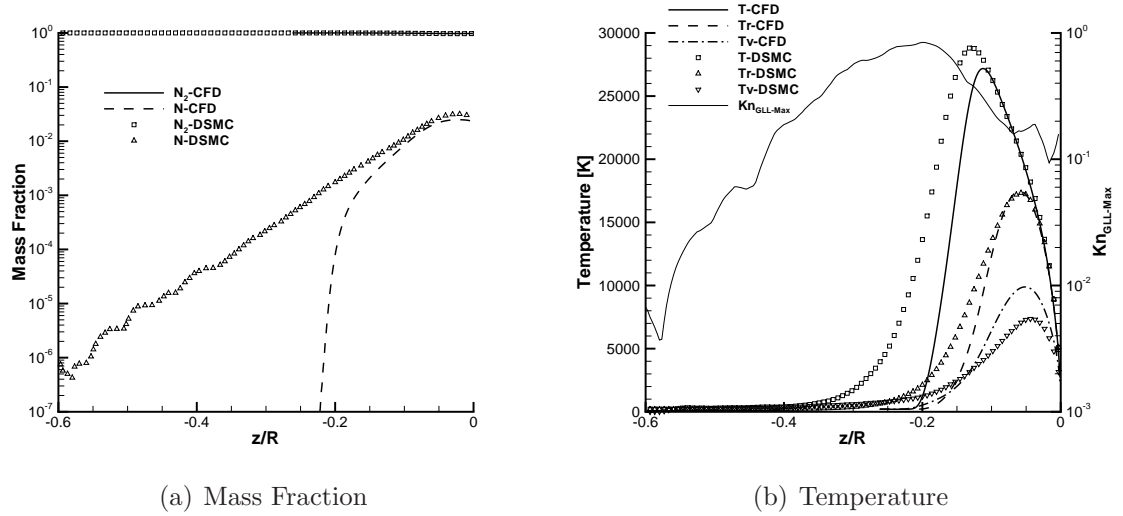
(b) Temperature

Figure 5.7: $Kn_\infty = 0.01$, mass fraction (left axis), temperature (left axis)and Kn_{GLL} (right axis) profiles along the stagnation streamline in a Mach 25 flow of reacting nitrogen

develops in front of the shock is caused by diffusion in DSMC. It is unclear if this is a physical phenomenon or the inability of DSMC to properly deal with trace species, as mentioned in Section 2.3.1. From this figure it can be seen that the amount of nitrogen dissociation is small at this Knudsen number, with the maximum mass fraction of atomic nitrogen being 0.03. From this figure it can be seen that the numerical methods compare well. The profiles for the temperatures and gradient length local Knudsen number along the stagnation streamline are given in Fig. 5.7(b). Since DSMC has a thicker shock, it can be seen that the temperature starts rising earlier than CFD. The flow is forced into thermal equilibrium as it moves closer to the wall, but CFD overshoots the DSMC vibrational temperature prior to reaching equilibrium. This phenomenon is not seen with the translational and rotational temperatures.

Kn$_\infty$ = 0.05

At a global Knudsen number of 0.05, the flow is expected to be outside of the continuum regime. From Fig. 5.8 it can be seen that the gradient length local Knudsen number is over the 0.05 limit indicating continuum breakdown in the shock and wake. The figure includes the Kn_{GLL} contours for the simulation with chemistry, given as flooded contours, and without chemistry, given as contour lines. This figure also includes the contours of Kn_{GLL}, given as dashed line contours, as predicted by the CFD method without reacting flow, but the transport properties are calculated with Gupta's mixing rule. It can be observed that there is a change in the level of breakdown between simulations with and without chemistry. However, there is no change in the amount of continuum breakdown between CFD with reacting flow and CFD with Gupta's mixing rule without chemical reactions. Since dissociation is not occurring in this flow, due to the rarefied nature of the gas at this Knudsen number, the change in the breakdown is not caused by reacting flow. The change in the gradient length local Knudsen number is caused by a different transport property model being utilized.

The coefficient of pressure and surface profile of gradient length local Knudsen number are given in Fig. 5.9(a). It is not surprising to note that the Kn_{GLL} profile is above the 0.05 limit over the entire surface, indicating continuum breakdown has occurred. The CFD method under predicts the pressure compared to DSMC near the stagnation point, but they compare well over the rest of the sphere. From the heat flux coefficient, given in Fig. 5.9(b), it can be seen that the CFD method predicts a larger value than DSMC over the whole surface. It is interesting to note that CFD with a slip boundary condition predicts a smaller value of heat flux than DSMC over the fore body, but a larger value over the aft body. The surface shear stress coefficient
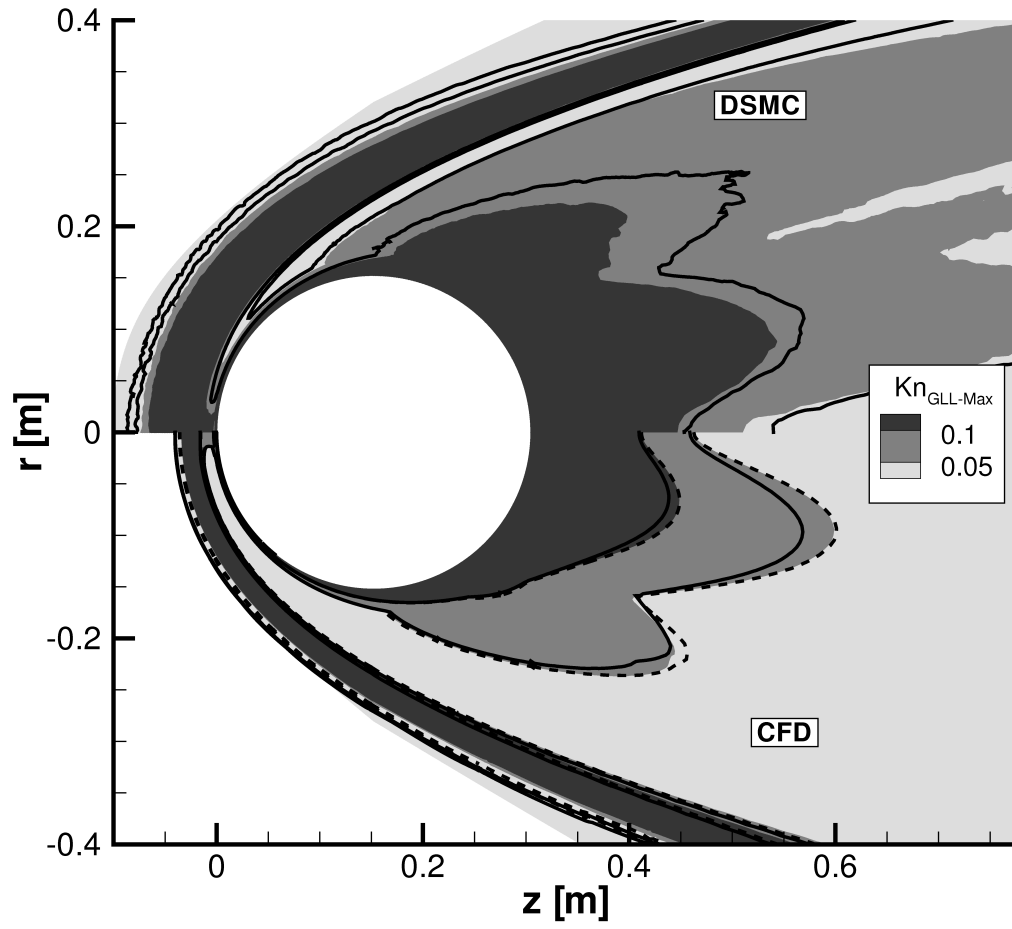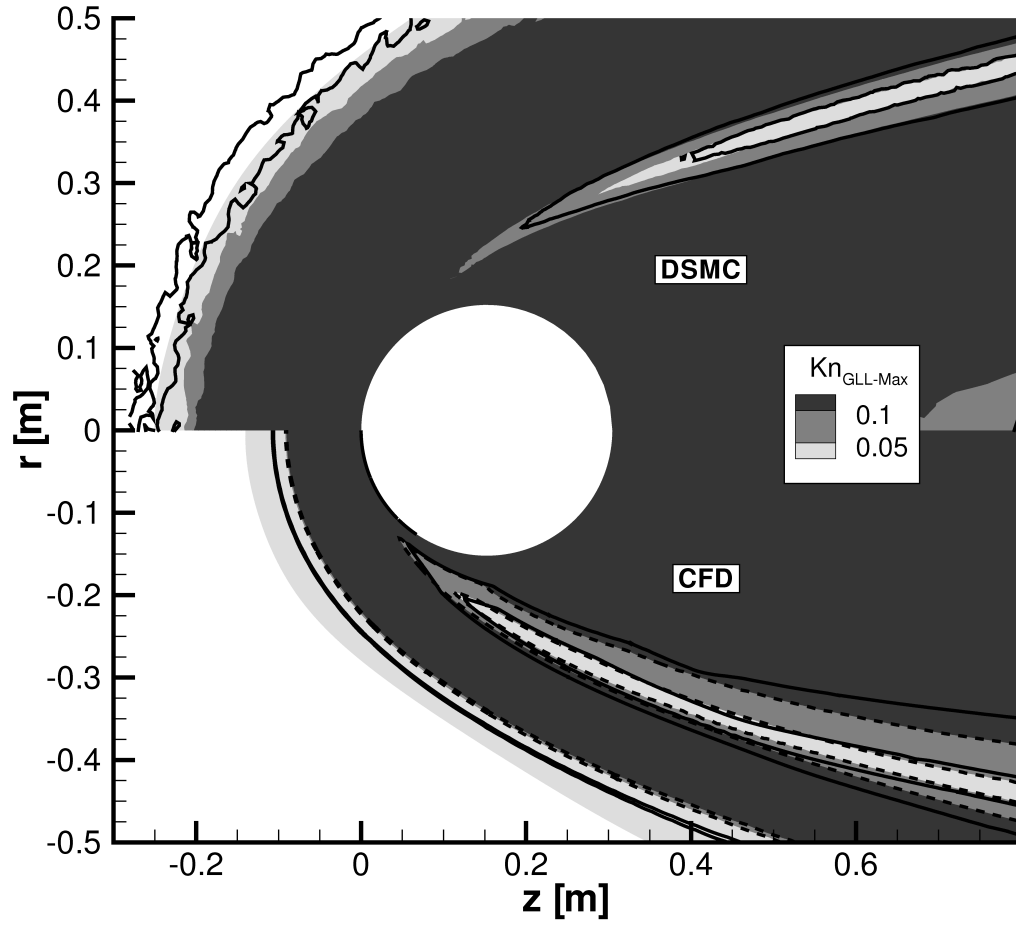
Figure 5.8: $Kn_\infty = 0.05$, Kn_{GLL} contours from DSMC (top) and CFD (bottom) with reacting flow (flooded contours) and without reacting flow (line contours), and CFD with Gupta's mixing rule (dashed line contours)

is given in Fig. 5.9(c). It can be observed that CFD agrees well with DSMC for the first 25 degrees of the sphere but then predicts a larger shear stress than DSMC over the rest of the surface. Implementation of a slip boundary condition in the CFD method improves the agreement with the DSMC prediction of shear stress. It should be noted that CFD with a slip boundary condition more accurately predicts the location of the peak shear stress.

$\text{Kn}_\infty = 0.25$

The last and highest global Knudsen number case discussed is 0.25. This is well outside the continuum regime and is considered to be a rarefied gas. This can be seen by the fact that Kn_{GLL} is greater than the 0.05 limit for most of the flow field, as shown in Fig. 5.10. This figure gives the gradient length local Knudsen number contours for a simulation with reacting flow and without reacting flow. It can be seen, in both DSMC and CFD, that there is a difference in the Kn_{GLL} contours with and without reacting flow. The shock has moved closer to the surface in the case with reacting flow, decreasing the amount of continuum breakdown seen in the flow field. This is not caused by dissociation in the flow field, since few reactions are taking place due to the rarefied nature of the gas. The cause of this change in the amount of continuum breakdown is due to the change in the transport property model utilized for the reacting flow simulations, as discussed in the previous cases.

The surface pressure coefficient, given in Fig. 5.11(a), shows that CFD with or without the slip boundary condition predicts larger values than DSMC. The CFD method predicts a stagnation pressure coefficient to be 2.2, which is higher than the 2.06 found using free molecular theory. However, CFD with a slip boundary condition predicts the stagnation coefficient of pressure to be a more reasonable 2.0, and the
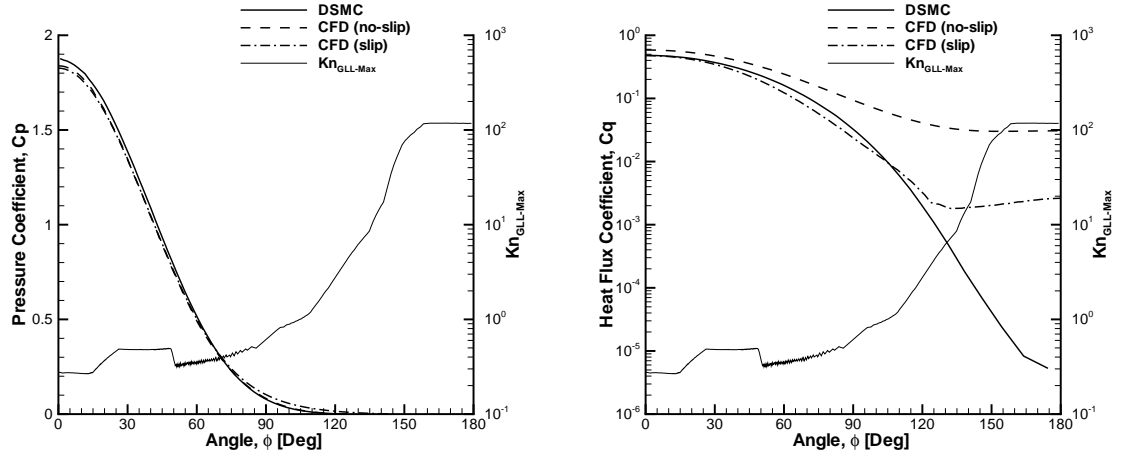
(a) Coefficient of Pressure

(b) Coefficient of Heat Flux
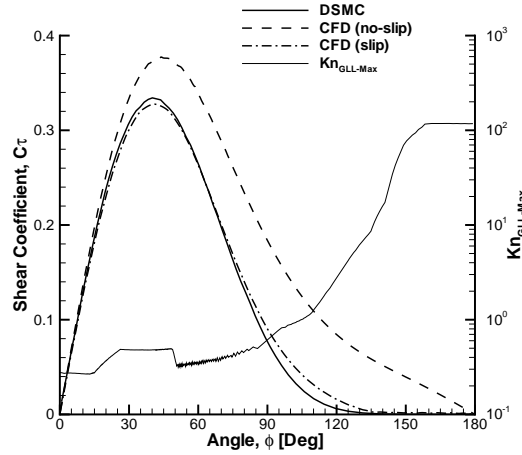
(c) Coefficient of Shear Stress

Figure 5.9: $Kn_\infty = 0.05$, surface pressure (left axis), surface heat flux (left axis), surface shear stress (left axis) and Kn_{GLL} surface profile (right axis) on a sphere in a Mach 25 flow of reacting nitrogen
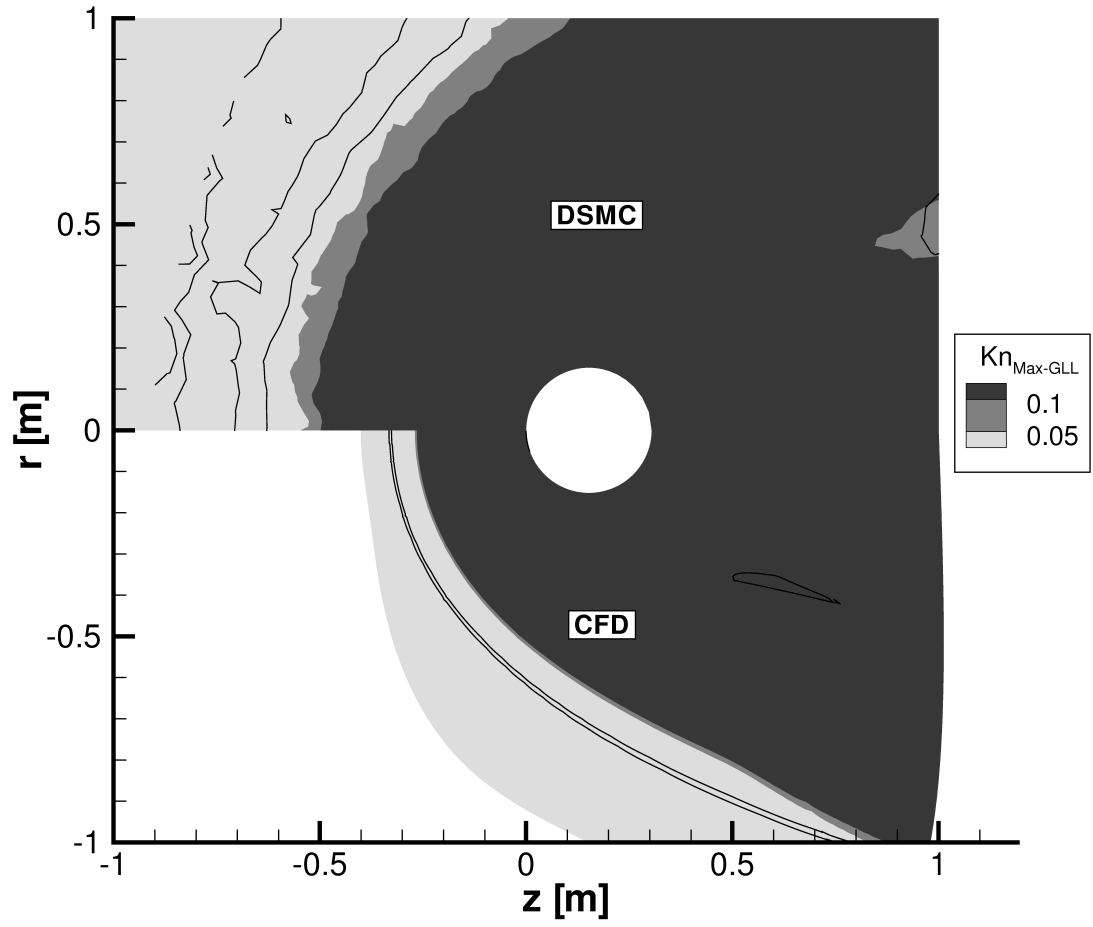
Figure 5.10: $Kn_\infty = 0.25$, Kn_{GLL} contours from DSMC (top) and CFD (bottom) with reacting flow (flooded contours) and without reacting flow (line contours)

DSMC method predicts it to be 1.9. Comparing the surface pressure with reacting flow and without reacting flow, Fig 4.24(b), it can be seen that CFD with reacting flow predicts a better agreement with DSMC. However, at this Knudsen number there are few chemical reactions occurring in the flow. The differences seen between reacting and non-reacting pressure coefficient come about due to the change in the transport property model. The surface heat flux coefficient is given in Fig. 5.11(b). It can be seen that the CFD method predicts a larger value of heat flux than DSMC over the entire surface. When a slip boundary condition is employed in the CFD method it under predicts DSMC over the fore body, but over predicts DSMC over the rest of the sphere. From the shear stress coefficient, given in Fig. 5.11(c), it can be seen that CFD with the no-slip boundary condition over predicts DSMC for the entire surface of the sphere. When a slip boundary condition is utilized, the CFD method under predicts DSMC, but it predicts the location of the peak value more accurately. This only confirms that the CFD method, with or without slip boundary conditions, cannot accurately predict the surface properties when the flow is rarefied. Comparing the reacting and non-reacting shear stress coefficient, Fig 4.25(b), it can be seen that the switch from a VHS viscosity model to Gupta's mixing rule with collision integral data has decreased the shear stress.

Computational Details

The computational details for the Mach 25 simulations in reacting nitrogen are given in Tables 5.4 and 5.5. It should be noted that Table 5.4 does not provide a fair comparison between simulations with and without reacting flow using the DSMC method, as the two sets of simulations were computed on different systems. The simulations with reacting flow using the DSMC method were performed on a system
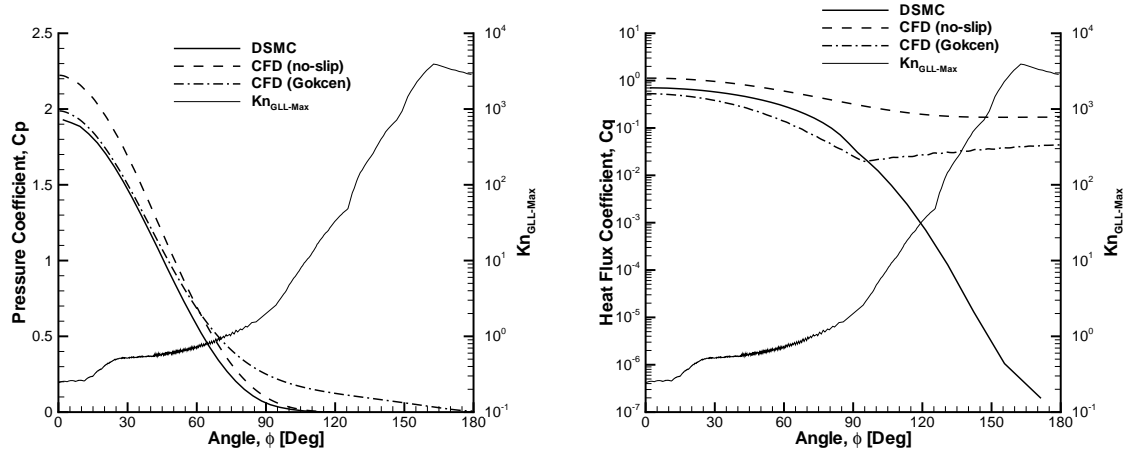
(a) Coefficient of Pressure

(b) Coefficient of Heat Flux
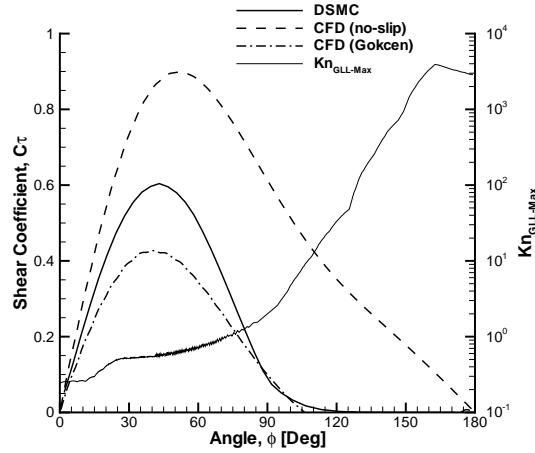
(c) Coefficient of Shear Stress

Figure 5.11: $Kn_\infty = 0.25$, surface pressure (left axis), surface heat flux (left axis), surface shear stress (left axis) and Kn_{GLL} surface profile (right axis) on a sphere in a Mach 25 flow of reacting nitrogen

with faster processors, explaining why the simulations took less time besides being more computationally intensive.

Table 5.4: Computational Details for DSMC Mach 25 Simulations, grayed rows are without chemical reactions

Kn_∞	Cells	Particles	Time Steps	CPU Time [hrs]
0.002	1,313,354	174,770,965	970,000	29,792
0.002	1,074,474	231,616,220	160,000	22,514
0.01	76,250	43,406,389	190,000	1,226
0.01	103,985	14,213,372	150,000	1,152
0.05	18,343	4,973,993	120,000	84
0.05	19,311	5,849,453	120,000	232
0.25	10,062	1,426,468	120,000	29
0.25	6,113	4,459,637	110,000	192

Table 5.5: Computational Details for CFD Mach 25 Simulations, grayed rows are without chemical reactions

Kn_∞	Cells	Iterations	CPU Time [hrs]
0.002	80,000	17,740	960
0.002	100,000	29,209	1,152
0.01	60,000	26,986	480
0.01	84,000	14,747	384
0.05	40,000	25,708	240
0.05	45,000	16,392	144
0.25	30,000	16,981	112
0.25	45,000	21,329	112

5.3 Air Flow

The next step in this study considers Mach 25 flow of 5 species reacting air over a sphere with a global Knudsen number varying from 0.002 to 0.25. The free stream

temperature is 200 K giving free a stream velocity of 7108 m/s. The surface of the sphere has a fixed temperature of 1500 K. The density of the free stream is varied to change the global Knudsen number of the flow from continuum to a rarefied gas as given in Table 5.6. The Knudsen number is calculated using the diameter of the sphere as the characteristic length and the hard sphere model to calculate the mean free path, as given in section 4.1.

Table 5.6: Simulated reacting airflow regimes

Kn_∞	Mass Density (kg/m^3)	Number Density $(particles/m^3)$	Mean Free Path (m)
0.002	1.007×10^{-4}	2.103×10^{21}	6.096×10^{-4}
0.01	2.014×10^{-5}	4.206×10^{20}	3.048×10^{-3}
0.05	3.987×10^{-6}	8.325×10^{19}	1.524×10^{-2}
0.25	8.057×10^{-7}	1.680×10^{19}	7.620×10^{-2}

5.3.1   Mach 25

This portion of the study aims to characterize the effects of continuum breakdown in a flow more representative of a real gas. This case involves 17 reactions, which includes dissociation, recombination and exchange reactions. All the reactions and their associated reaction rate coefficients are given in Appendix A.3. In the CFD method, the rate coefficients are utilized in the modified Arrhenius form along with a preferential dissociation model to calculate the forward reaction rates. In the DSMC technique, the rate coefficients are utilized in the VFD model to calculate the forward reaction rates. The backward reaction rates are calculated using Park's equilibrium constant[66]. For this study, both numerical techniques use non-catalytic, fully diffuse wall conditions. Also, in the CFD method the transport property model is switched from a VHS viscosity model with Eucken's relation to Gupta's mixing

rule with collision integral data. In the DSMC method, to maintain consistency between both numerical methods, new VHS parameter values are found to match the collision integral data for the reacting flow simulations. The new VHS parameters for all five species are given in Appendix A.4. A more in depth discussion on all of these models is provided in Chapter III.

The integrated drag, peak heat flux and percent difference between DSMC and CFD are given in Tables 5.7 and 5.8, respectively. Since DSMC is a particle method that works in both the continuum regime and the rarefied regime, it is assumed that the DSMC results are more accurate. Therefore, the percent difference is calculated using the DSMC result as the basis.

Table 5.7: Integrated Drag [N] (% difference) from DSMC and CFD at Mach 25 in Reacting Air

Kn_∞	DSMC	CFD (no-slip)	CFD (Gökçen)
0.002	178	175(-1.69%)	174(-2.25%)
0.01	40.8	41.0(0.49%)	40.3(-1.22%)
0.05	10.1	11.8(16.8%)	9.79(-3.07%)
0.25	2.53	4.80(89.9%)	2.58(1.98%)

Table 5.8: Peak Heating $\left[\frac{W}{m^2}\right]$ (% difference) from DSMC and CFD at Mach 25 in Reacting Air

Kn_∞	DSMC	CFD (no-slip)	CFD (Gökçen)
0.002	9.30×10^5	9.46×10^5(1.63%)	9.26×10^5(-0.46%)
0.01	8.04×10^5	8.98×10^5(11.7%)	8.42×10^5(4.72%)
0.05	3.54×10^5	4.44×10^5(25.5%)	3.70×10^5(4.60%)
0.25	1.05×10^5	1.72×10^5(63.5%)	8.55×10^4(-18.7%)

From these tables it can be seen that the comparisons between CFD and DSMC

(a) Kn_{GLL}

(b) Coefficient of Pressure

Figure 5.12: $Kn_\infty = 0.002$, Kn_{GLL} contours, surface pressure (left axis) and Kn_{GLL} surface profile (right axis) on a sphere in a Mach 25 flow of reacting air

diverge with growing global Knudsen number. In the following subsections, the surface properties and gradient length local Knudsen number are discussed in more detail for each case.

$\mathbf{Kn_\infty = 0.002}$

Given the global Knudsen number, the flow is expected to be in the continuum regime. However, there are regions of local continuum breakdown in the shock and wake regions as shown in Fig. 5.12(a). There is a larger area of continuum breakdown observed in DSMC than CFD in both the shock region and in the wake region behind the sphere.

The surface pressure coefficient is given in Fig. 5.12(b), along with the surface profile of Kn_{GLL}. Notice that Kn_{GLL} is above 0.05 for nearly the entire surface, indicating the flow is considered to be in continuum breakdown. Despite continuum breakdown at the surface, the pressures predicted by DSMC and CFD match very well. The surface heat flux predicted by CFD compares well with DSMC over the

(a) Coefficient of Heat Flux

(b) Coefficient of Shear Stress

Figure 5.13: $Kn_\infty = 0.002$, surface heat flux (left axis), surface shear stress (left axis) and Kn_{GLL} surface profile (right axis) on a sphere in a Mach 25 flow of reacting air

fore body of the sphere, as shown in Fig 5.13(a). The divergence in the solution may be caused by the breakdown on the surface, especially over the aft of the sphere. The shear stress over the surface of the sphere is given in Fig. 5.13(b). The shear stress prediction given by CFD compares well with DSMC over the surface, with only slight disagreement in the aft of the sphere.

To determine the level of chemistry occurring in the flow, the mass fractions of each species are given in Fig. 5.14(a). It can be seen that in DSMC trace species diffuse out from behind the shock. This phenomenon can be seen by the discrepancies between CFD and DSMC in mass fraction for nitric oxide, atomic oxygen and atomic nitrogen that develop in front of the shock. It is unclear if this is a physical phenomenon or numerical problems in DSMC dealing with trace species. From the figure it can be seen that the mass fractions predicted by the two methods compare well, the only noticeable difference is in the mass fraction for nitric oxide. The temperature and gradient length local Knudsen number profiles along the stagna-

(a) Mass Fraction

(b) Temperature

Figure 5.14: $Kn_\infty = 0.002$, mass fraction (left axis), temperature (left axis) and Kn_{GLL} (right axis) profiles along the stagnation streamline in a Mach 25 flow of reacting air

tion streamline are given in Fig. 5.14(b). It can be observed that the translational temperature matches well between the two methods. However, the rotational and vibrational temperatures do not match as well. The over prediction of rotational and vibrational temperatures by CFD as compared to DSMC is an expected result, caused by thermal nonequilibrium. From the profile of Kn_{GLL}, it is seen that the flow is expected to be in the continuum regime as it approaches the wall.

$Kn_\infty = 0.01$

At a global Knudsen number of 0.01, the traditional limit for accurate CFD simulations, there is significant breakdown in the shock, boundary layer and the wake regions of the flow, as seen in Fig. 5.15(a). At this condition, the amount of continuum breakdown is larger in DSMC than in CFD. Notice that the flow is in continuum breakdown all the way from the shock to the surface of the sphere near the stagnation streamline.

The surface pressures computed from the CFD method, with or without slip
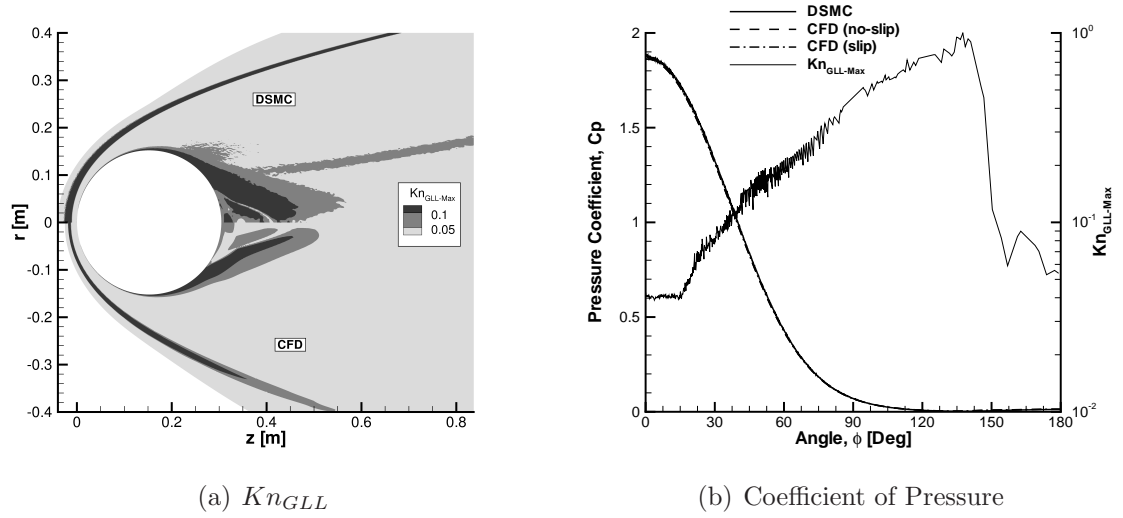
(a) Kn_{GLL}

(b) Coefficient of Pressure

Figure 5.15: $Kn_\infty = 0.01$, Kn_{GLL} contours, surface pressure (left axis) and Kn_{GLL} surface profile (right axis) on a sphere in a Mach 25 flow of reacting air

boundary conditions, under predict DSMC near the stagnation point, as shown in Fig. 5.15(b). This figure also includes the surface profile of the gradient length local Knudsen number which shows the flow over the entire surface is in breakdown. This may have caused the slight discrepancy seen in the pressure coefficient near the stagnation point. The heat flux predicted by CFD with no-slip is always larger than DSMC over the entire surface, as can be seen in Fig. 5.16(a). An improvement is seen if the slip boundary condition is employed in the CFD method. At this Knudsen number, the CFD method, with and with out slip boundary conditions, under predicts the shear stress near the location of the maximum, as shown in Fig. 5.16(b). It can also be seen that the CFD method over predicts DSMC over the aft of the sphere. It is also interesting to note that the CFD method predicts that the peak shear stress occurs slightly later on the surface of the sphere.

To be able to determine the level of chemistry occurring in the flow, the mass fractions of each species are given in Fig. 5.17(a). The large discrepancies between CFD and DSMC in mass fraction for nitric oxide, atomic oxygen and atomic nitrogen

(a) Coefficient of Heat Flux
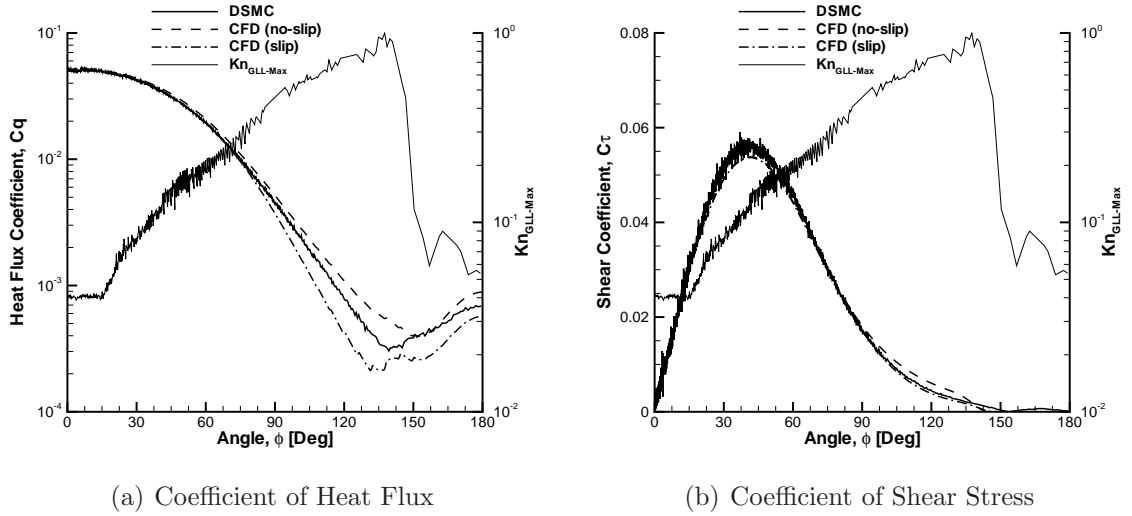
(b) Coefficient of Shear Stress

Figure 5.16: $Kn_\infty = 0.01$, surface heat flux (left axis), surface shear stress (left axis) and Kn_{GLL} surface profile (right axis) on a sphere in a Mach 25 flow of reacting air

that develop in front of the shock are caused by diffusion in DSMC. From this figure it can be seen that molecular oxygen has dissociated while molecular nitrogen has undergone little change. There is a negligible amount of atomic nitrogen and nitric oxide created behind the shock, with peak mass fractions of approximately 0.03 and 0.02, respectively. It is an expected result that molecular oxygen dissociates more easily due to a weaker bond as compared to molecular nitrogen. The profiles for the temperatures and gradient length local Knudsen number along the stagnation streamline are given in Fig. 5.17(b). Since DSMC predicts a thicker shock, it can be seen that the temperature starts rising earlier then CFD. The flow is forced into thermal equilibrium as it moves closer to the wall, but CFD overshoots the DSMC temperatures prior to reaching equilibrium. This phenomenon was discussed in section 4.2, and is caused by the fact that the flow is in thermal nonequilibrium following the shock.
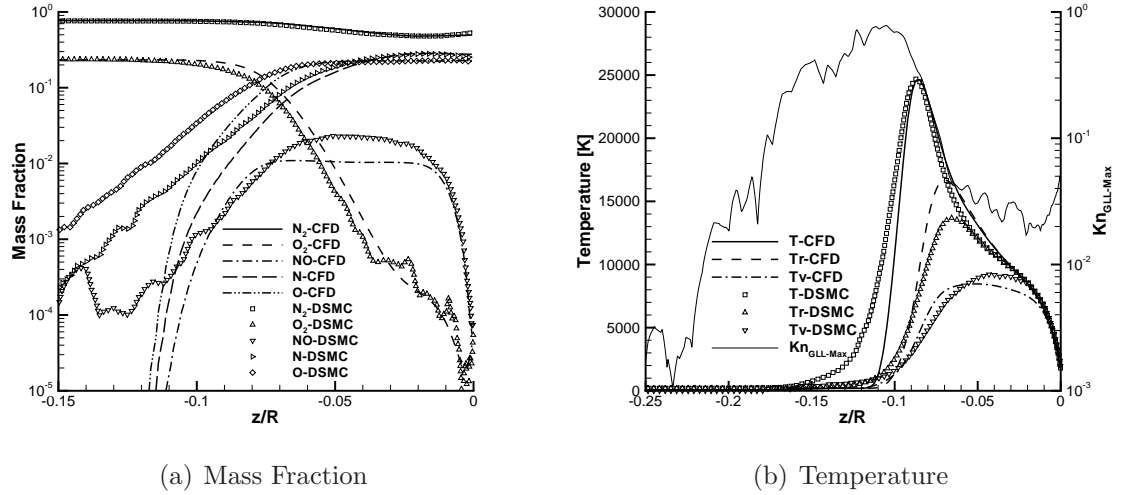
(a) Mass Fraction

(b) Temperature

Figure 5.17: $Kn_\infty = 0.01$, mass fraction (left axis), temperature (left axis) and Kn_{GLL} (right axis) profiles along the stagnation streamline in a Mach 25 flow of reacting air

$\mathbf{Kn_\infty = 0.05}$

At a global Knudsen number of 0.05, the flow is expected to be outside of the continuum regime and in the transition regime. The contours of gradient length local Knudsen number are given in Fig. 5.18(a). It can be seen that the gradient length local Knudsen number is over the 0.05 limit indicating continuum breakdown in the shock and wake. It can be observed that the DSMC method predicts larger amounts of continuum breakdown than CFD.

It can be seen that the CFD method, with or without slip boundary conditions, under predicts the DSMC surface pressure coefficient over the fore body, but over predicts DSMC over the aft of the sphere, as shown in Fig. 5.18(b). This figure also gives the gradient length local Knudsen number, which shows that at the surface the value of Kn_{GLL} is over 0.05; indicating the flow is in continuum breakdown. The CFD method over predicts the heat flux over the entire surface as compared to DSMC, as shown in Fig. 5.19(a). There is an improvement in the agreement with
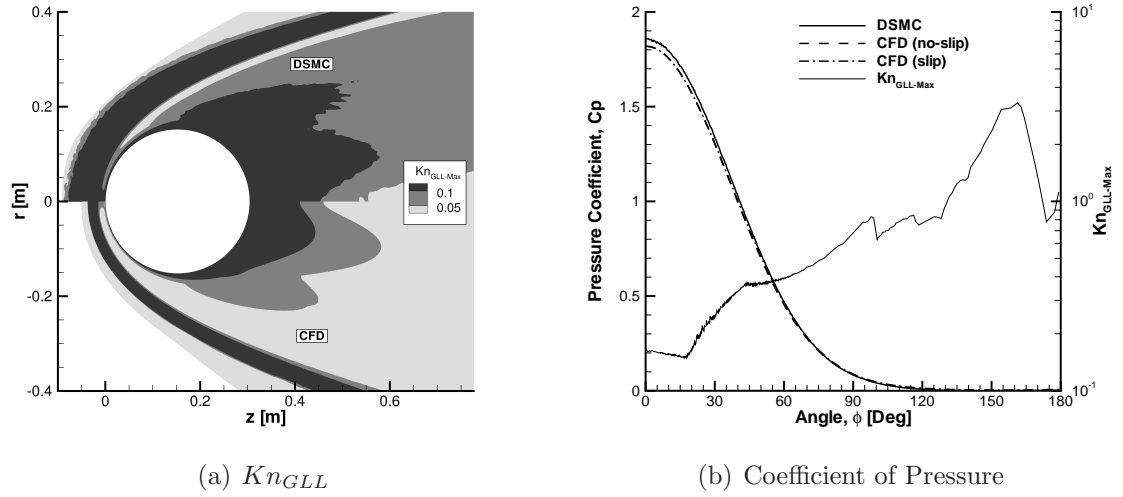
(a) Kn_{GLL}

(b) Coefficient of Pressure

Figure 5.18: $Kn_\infty = 0.05$, Kn_{GLL} contours, surface pressure (left axis) and Kn_{GLL} surface profile (right axis) on a sphere in a Mach 25 flow of reacting air

DSMC when the slip boundary condition is utilized in the CFD method, but there is still a large disagreement over the aft of the sphere. The shear stress coefficient, given in Fig. 5.19(b), is over predicted by CFD assuming no-slip boundaries as compared to DSMC. However, when a slip boundary condition is employed in the CFD technique there is better agreement with DSMC for the shear stress coefficient.

The mass fractions of each species are given in Fig. 5.20(a). At this Knudsen number, it can be seen from the molecular nitrogen and oxygen that little dissociation is occurring along the stagnation streamline. This is because the flow is relatively diffuse, with few collisions and even fewer reactions taking place. It can be seen that trace species diffuse out in front of the shock in the DSMC method. However, for both numerical methods there is a negligible amount of atomic nitrogen, atomic oxygen and nitric oxide behind the shock. A mass fraction of less than 0.02 for all trace species in DSMC, and much lower in CFD, can be observed in the figure. It can be seen that there is a large discrepancy in the mass fraction of atomic oxygen, almost 90 percent difference at the wall. Large differences can be observed in the atomic

(a) Coefficient of Heat Flux
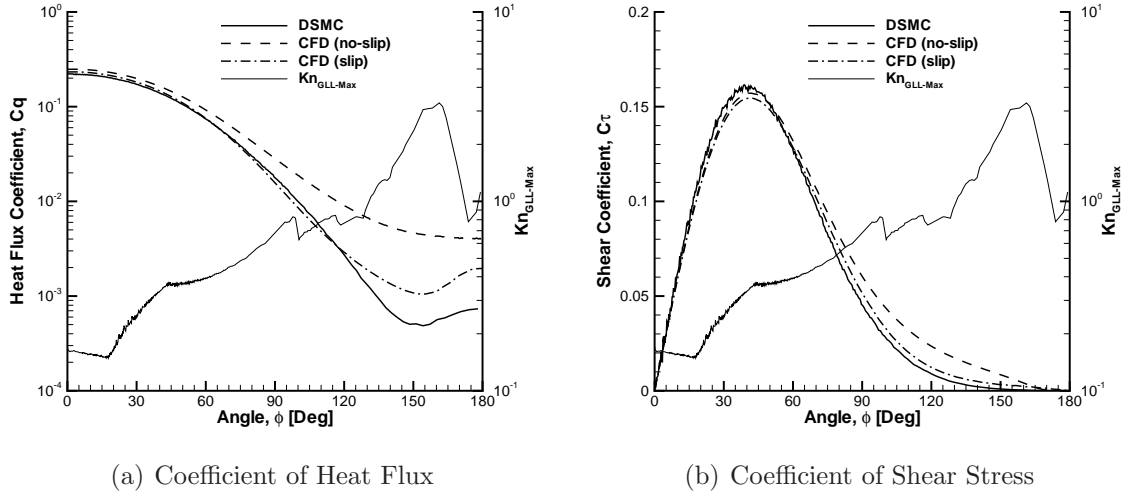
(b) Coefficient of Shear Stress
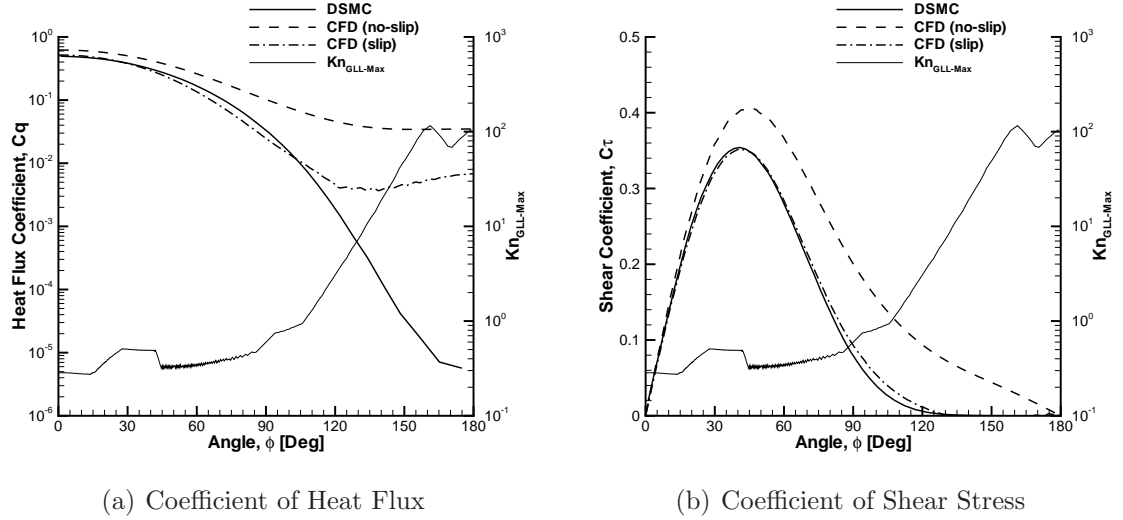
Figure 5.19: $Kn_\infty = 0.05$, surface heat flux (left axis), surface shear stress (left axis) and Kn_{GLL} surface profile (right axis) on a sphere in a Mach 25 flow of reacting air

nitrogen and nitric oxide mass fractions as well. The profiles for the temperatures and gradient length local Knudsen number along the stagnation streamline are given in Fig. 5.20(b). Since DSMC has a thicker shock it can be seen that the temperature starts rising earlier then CFD. The flow is forced towards thermal equilibrium as it moves closer to the wall. However, at this high of a Knudsen number, thermal equilibrium is not reached prior to the wall.

$\mathbf{Kn_\infty = 0.25}$

The highest global Knudsen number considered in this study is 0.25. At this Knudsen number, the flow is in the rarefied regime, outside the range of where the CFD method should be employed. At this high of a global Knudsen number, the entire flow is in continuum breakdown, as seen in Fig. 5.21(a). The shock standoff distance in DSMC is farther out than in CFD, almost twice the distance in DSMC as compared to CFD.

At this condition, continuum breakdown, has a strong effect on the surface prop-
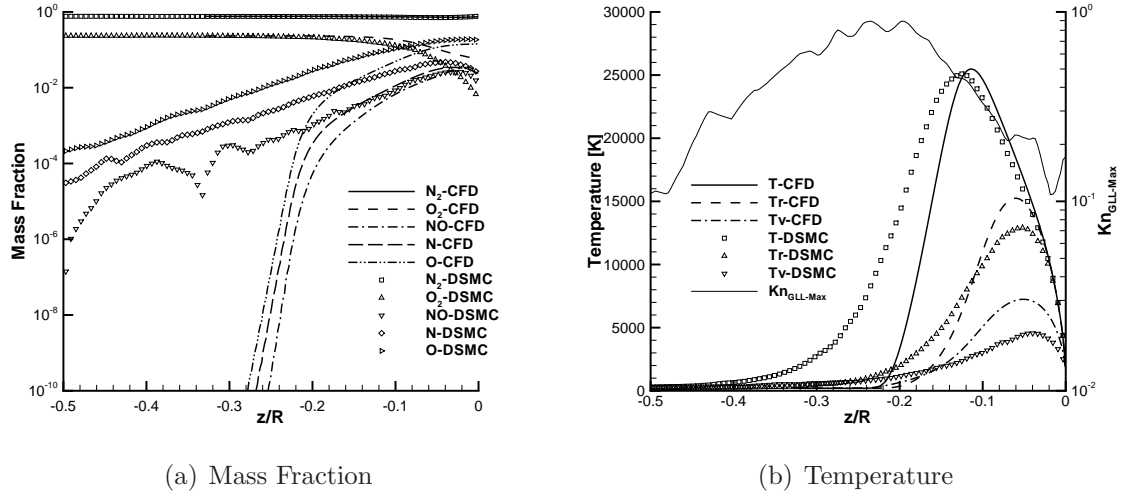
(a) Mass Fraction
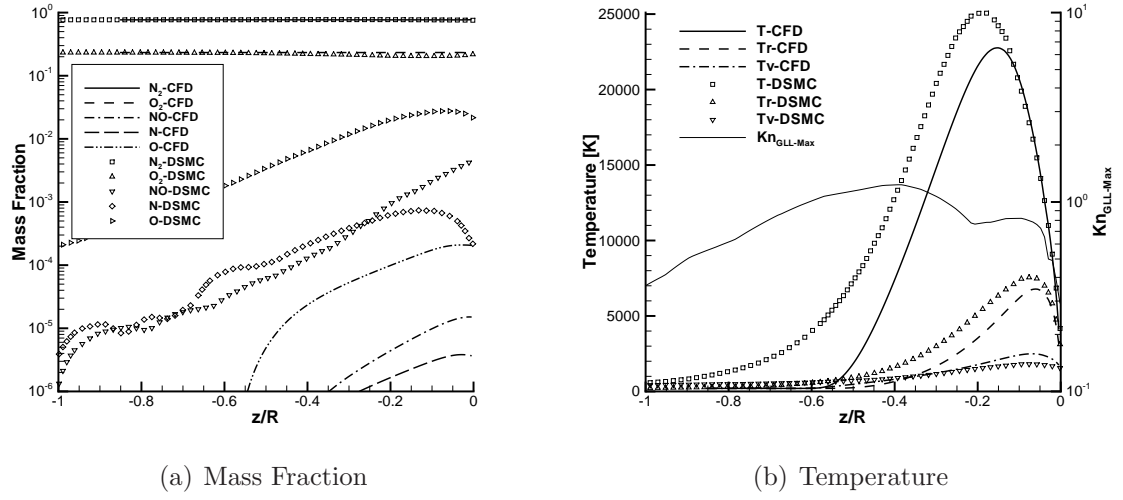
(b) Temperature

Figure 5.20: $Kn_\infty = 0.05$, mass fraction (left axis), temperature (left axis) and Kn_{GLL} (right axis) profiles along the stagnation streamline in a Mach 25 flow of reacting air

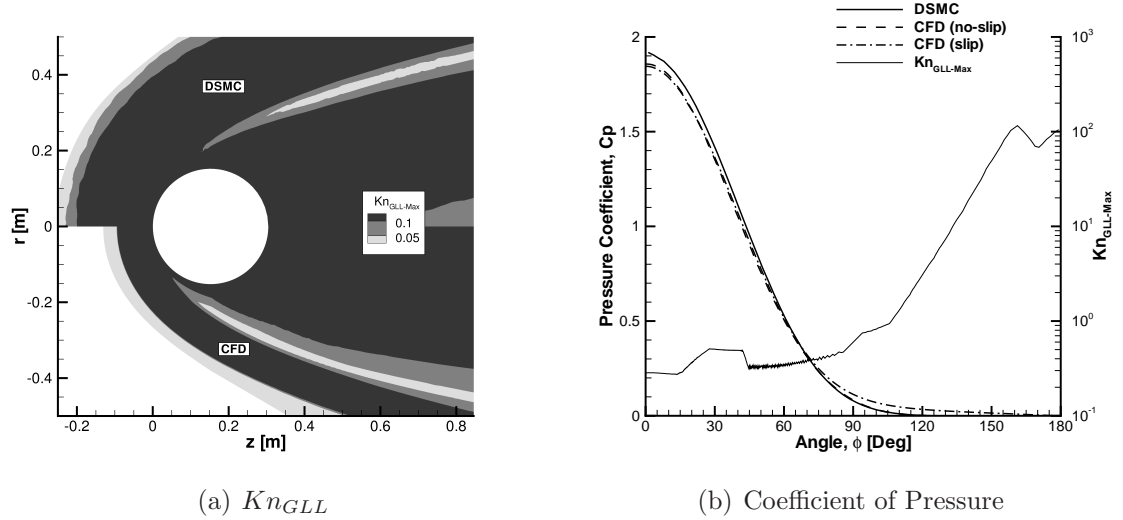(a) Kn_{GLL}

(b) Coefficient of Pressure
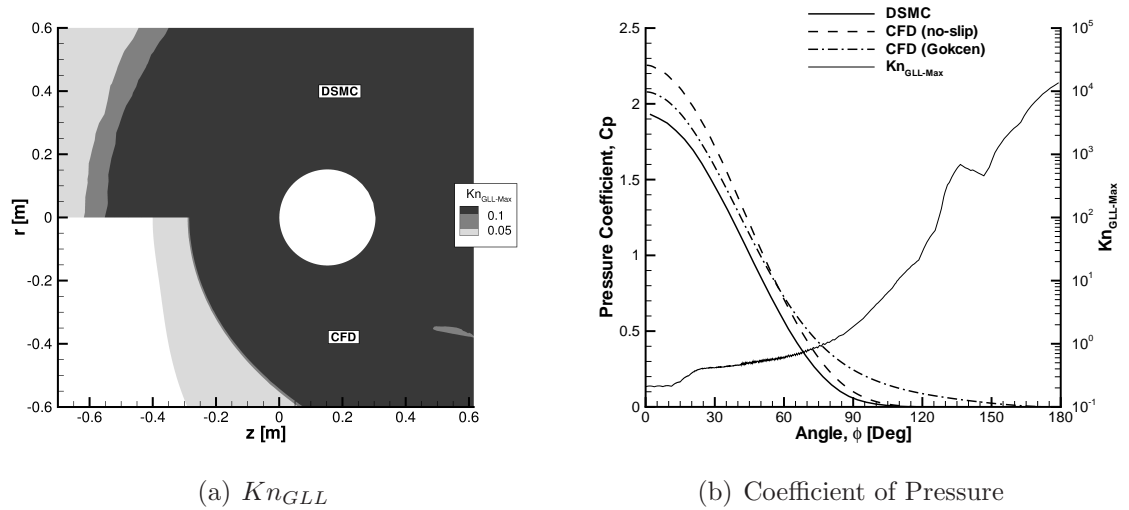
Figure 5.21: $Kn_\infty = 0.25$, Kn_{GLL} contours, surface pressure (left axis) and Kn_{GLL} surface profile (right axis) on a sphere in a Mach 25 flow of reacting air

(a) Coefficient of Heat Flux

(b) Coefficient of Shear Stress
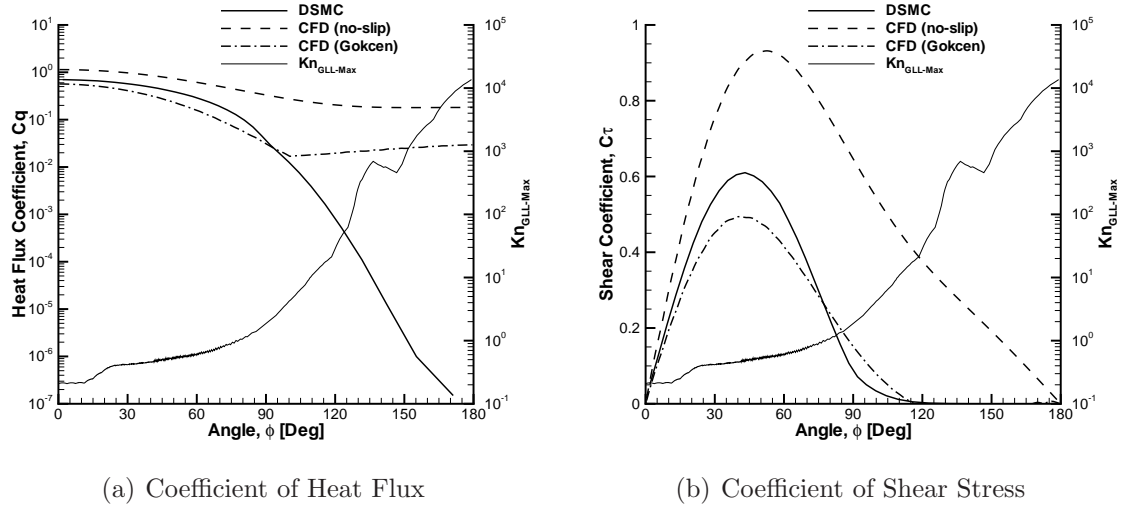
Figure 5.22: $Kn_\infty = 0.25$, surface heat flux (left axis), surface shear stress (left axis) and Kn_{GLL} surface profile (right axis) on a sphere in a Mach 25 flow of reacting air

erties. The surface pressure coefficient is given in Fig. 5.21(b), along with the surface profile of gradient length local Knudsen number. The surface pressure coefficient is over predicted by CFD, with or without slip boundary conditions, as compared to DSMC. The surface heat flux coefficient shows very poor agreement between CFD and DSMC, as shown in Fig. 5.22(a). When slip boundary conditions are employed, in the CFD method the heat flux is under predicted over the fore body as compared to DSMC, but is over predicted by CFD over the aft of the sphere. The shear stress is over predicted by CFD without slip as compared to DSMC, as shown in Fig. 5.22(b). When slip boundary conditions are implemented in the CFD method, the shear stress is under predicated over the fore body and over predicted over the aft body as compared to DSMC. Notice that the location of peak shear stress predicted by CFD with slip is approximately in the same location as DSMC, while the location predicted by CFD without slip occurs further back on the surface of the sphere.

The mass fractions for each species along the stagnation streamline at this flow

(a) Mass Fraction
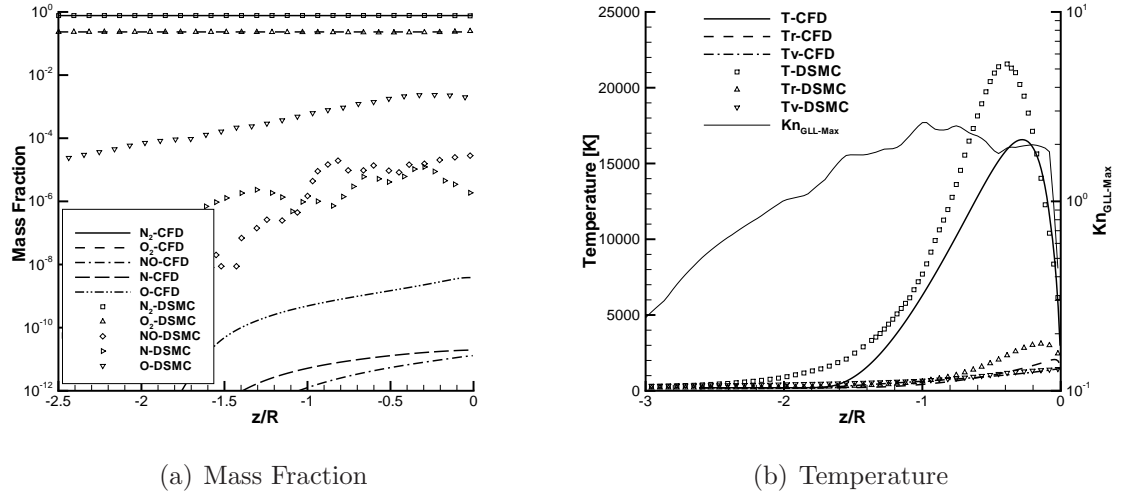
(b) Temperature

Figure 5.23: $Kn_\infty = 0.25$, mass fraction (left axis), temperature (left axis) and Kn_{GLL} (right axis) profiles along the stagnation streamline in a Mach 25 flow of reacting air

condition are given in Fig. 5.23(a). At this high of a global Knudsen number there is little change in the mass fractions for molecular oxygen and nitrogen. As a result there are negligible amounts of nitric oxide, atomic nitrogen and atomic oxygen produced. From the figure it can be seen that there are large discrepancies in the trace species between the numerical methods. However, the two numerical techniques compare very well for the two major species, molecular nitrogen and molecular oxygen. The temperature and gradient length local Knudsen number profiles along the stagnation streamline are given in Fig. 5.23(b). It is interesting to note that at this global Knudsen number, the rotational and vibrational temperatures are small in comparison to the translational temperature. Since there are so few collisions, the gas never achieves thermal equilibrium, hence the reason the rotational and vibrational temperature are so low. This also has the effect of limiting the amount of chemical reactions that take place in the flow, which is the reason there is so little dissociation seen in this case.

Computational Details

The computational details for the Mach 25 simulations in reacting air are given in Tables 5.9 and 5.10.

Table 5.9: Computational Details for DSMC Mach 25 Simulations

Kn_∞	Cells	Particles	Time Steps	CPU Time [hrs]
0.002	1,104,361	183,350,709	1,300,000	39,192
0.01	70,902	44,528,677	1.200,000	1,257
0.05	9,682	3,995,760	300,000	189
0.25	6,113	3,284,208	200,000	112

Table 5.10: Computational Details for CFD Mach 25 Simulations

Kn_∞	Cells	Iterations	CPU Time [hrs]
0.002	80,000	23,040	960
0.01	40,000	35,123	960
0.05	48,000	25,527	640
0.25	30,000	11,738	112

5.4   Summary: Comparison of Reacting Flow

This chapter investigated the effects of continuum breakdown on the surface aerothermodynamic properties (pressure, stress, heat transfer rate) of a sphere in Mach 25 flows in regimes varying from continuum flow to a rarefied gas flow. The first part of this study focused on the effects of reacting flow on continuum breakdown by comparing simulations in nitrogen with and without chemistry. For these simulations, the VHS viscosity model with Eucken's relation for thermal conductivity was replaced with Gupta's mixing rule with collision integral data. It was found that this change had several effects on the results of these simulations. It was found that this switch

in the transport property model caused the integrated drag and peak heating to decrease. It was also seen that chemically reacting flow caused a decrease in the peak heating. It was also observed that the switch in the transport property model caused a decrease in the amount of continuum breakdown. However, chemical reactions were also seen to decrease the amount of continuum breakdown in the flow field.

The second part of this study looked at the effects of reacting air flow on continuum breakdown and the surface properties of a sphere over a range of global Knudsen numbers varying from continuum to rarefied flow. Differences in peak heat flux and integrated drag between CFD and DSMC were observed to grow with growing global Knudsen number. When slip boundary conditions were employed in the CFD method, the agreement with DSMC improved. It was found that at higher Knudsen numbers, the effects of chemically reacting flow on continuum breakdown and the surface poperties of a hypersonic body were almost nonexistent. This is due to the diffuse nature of the gas at high Knudsen numbers, where collisions are infrequent and reactions are even more rare. It was found that at lower Knudsen numbers, the flow has a significant amount of chemistry occurring in the flow field. It is seen that the reactions occurring in the flow cause the surface heating to decrease.

CHAPTER VI

Comparison of Overall Trends

This chapter discusses the trends seen in the results by examining the stagnation pressure coefficient, the stagnation heat flux coefficient, and the drag coefficient for all cases presented in this thesis. This comparison is performed to be able to more easily discern the fundamental trends seen in CFD and DSMC over the whole range of Mach and Knudsen numbers presented in this work.

6.1   Drag Coefficient

In the previous two chapters, the peak heat flux and the integrated drag predictions from the CFD and DSMC methods were compared for all cases discussed. The integrated drag can be utilized to find the coefficient of drag, as given in Eq 6.1.

$$C_d = \frac{D}{\frac{1}{2}\rho_\infty U_\infty^2 A}$$
(6.1)

where D is the integrated drag, ρ is the density, U is the velocity, ∞ indicates free stream conditions, and A is the surface area. The coefficient of drag for each case as predicted by the CFD method, the CFD procedure with slip boundary conditions and the DSMC technique are given in Fig. 6.1.

In this figure, the DSMC prediction of the drag coefficient is given by green lines,
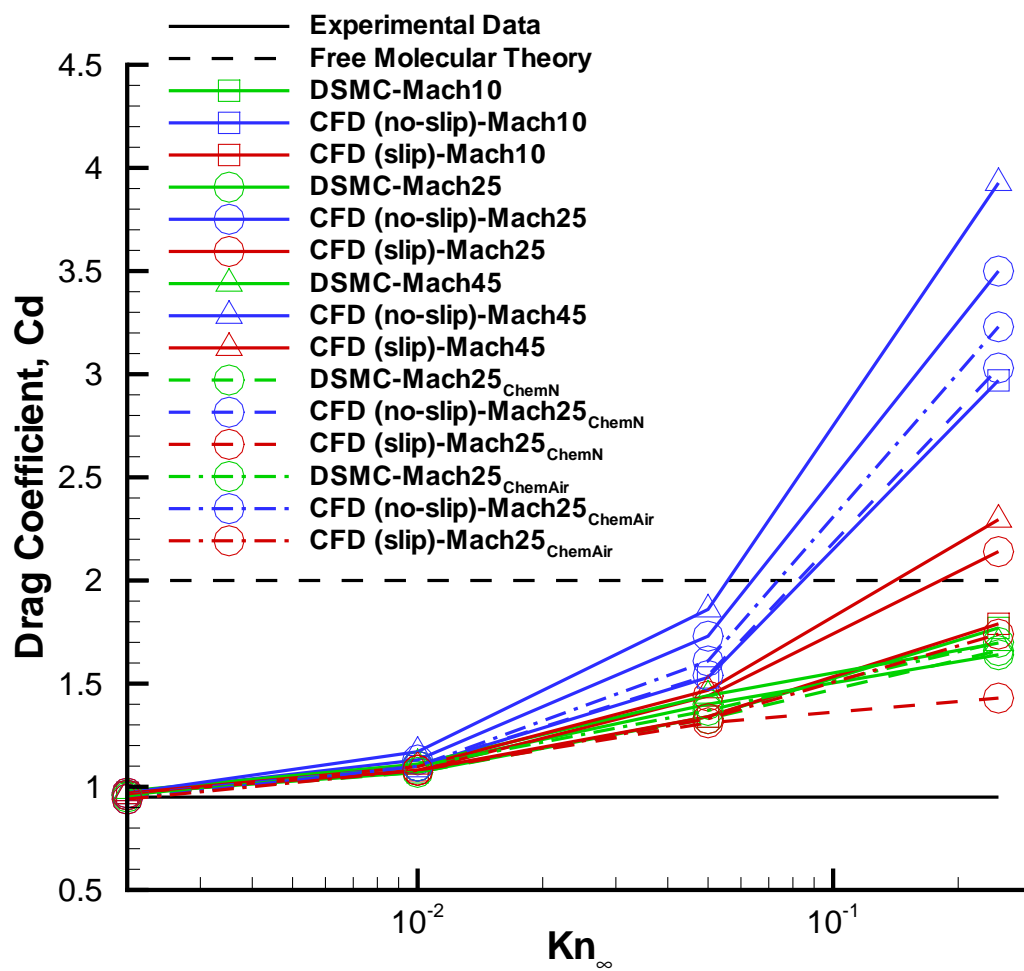
Figure 6.1: Drag Coefficient for DSMC and CFD with Upper and Lower Bounds

by blue lines for the CFD method, and by red lines for the CFD results with slip boundary conditions. The solid lines represent the coefficient of drag in a flow of nitrogen, the dashed lines represent the results in a flow of reacting nitrogen and the dash-dot lines represent the coefficient of drag in a flow of reacting air. The upper limit is found to be 2 using free molecular theory[26], and the lower limit is found to be 0.95 from experimental results[83]. From this figure it can be seen that all the cases are in good agreement at the lower Knudsen numbers. However, it can be seen that the CFD method starts to predict higher drag coefficients than the DSMC method at Knudsen numbers higher than 0.01. At Knudsen numbers higher than 0.05, the CFD method predicts the drag coefficient to be higher than the upper limit, verifying that the CFD method is only accurate in near equilibrium flow. It can also be observed that the CFD method with slip boundary conditions improves the agreement with DSMC. However, at a Knudsen number of 0.25, the results can be erratic, where one case predicts a value below the lower limit and other cases predict a value above the upper limit. From this figure it can be observed that the use of slip boundary conditions in the CFD method can extend its viability to higher Knudsen numbers, but as the Knudsen number increases it will eventually breakdown as well. The DSMC predicted values of drag coefficient are bound in the limits, and they approach the upper limit as the Knudsen number increases.

6.2 Stagnation Point Properties

The surface properties at the stagnation point are one of the most difficult areas to compute correctly in a hypersonic simulation due to the normal shock causing significant continuum breakdown. In the following sections, the stagnation pressure coefficient and the stagnation heat flux coefficient are given for all the cases presented

in this work.

6.2.1 Stagnation Pressure Coefficient

As discussed in Chapters IV and V, the pressure coefficient was given for all cases over the entire surface of the sphere. It was observed that the surface pressure was least affected by continuum breakdown, as it usually agreed well between the two numerical methods. However, the surface pressure at the stagnation point did vary with Knudsen number as shown in Fig. 6.2.

In this figure, the stagnation pressure coefficient from the DSMC method is given by green lines, is given by blue lines for the CFD method, and is given by red lines for the CFD method with slip boundary conditions. The solid lines represent the coefficient of pressure in a flow of nitrogen, the dashed lines represent the results in a flow of reacting nitrogen and the dash-dot lines represent the coefficient of pressure in a flow of reacting air. The upper limit is found to be 2.01 using free molecular theory, and the lower limit is found to be 1.825 in the inviscid limit. At lower Knudsen numbers, all the methods are in good agreement. However, as the Knudsen number increases, the agreement between the CFD method and the DSMC method diverges. At Knudsen numbers larger than 0.05, the CFD method predicts a stagnation pressure coefficient larger than the upper limit for all cases. From the figure it can be observed that the CFD method utilizing slip boundary conditions improves agreement with the DSMC prediction of the stagnation pressure coefficient. However, at a Knudsen number of 0.25, the prediction of the stagnation pressure coefficient by the CFD method with slip boundary conditions is erratic, with two cases predicting values below the lower limit and two cases predicting values above the upper limit. This confirms that the CFD method, with or with out slip boundary
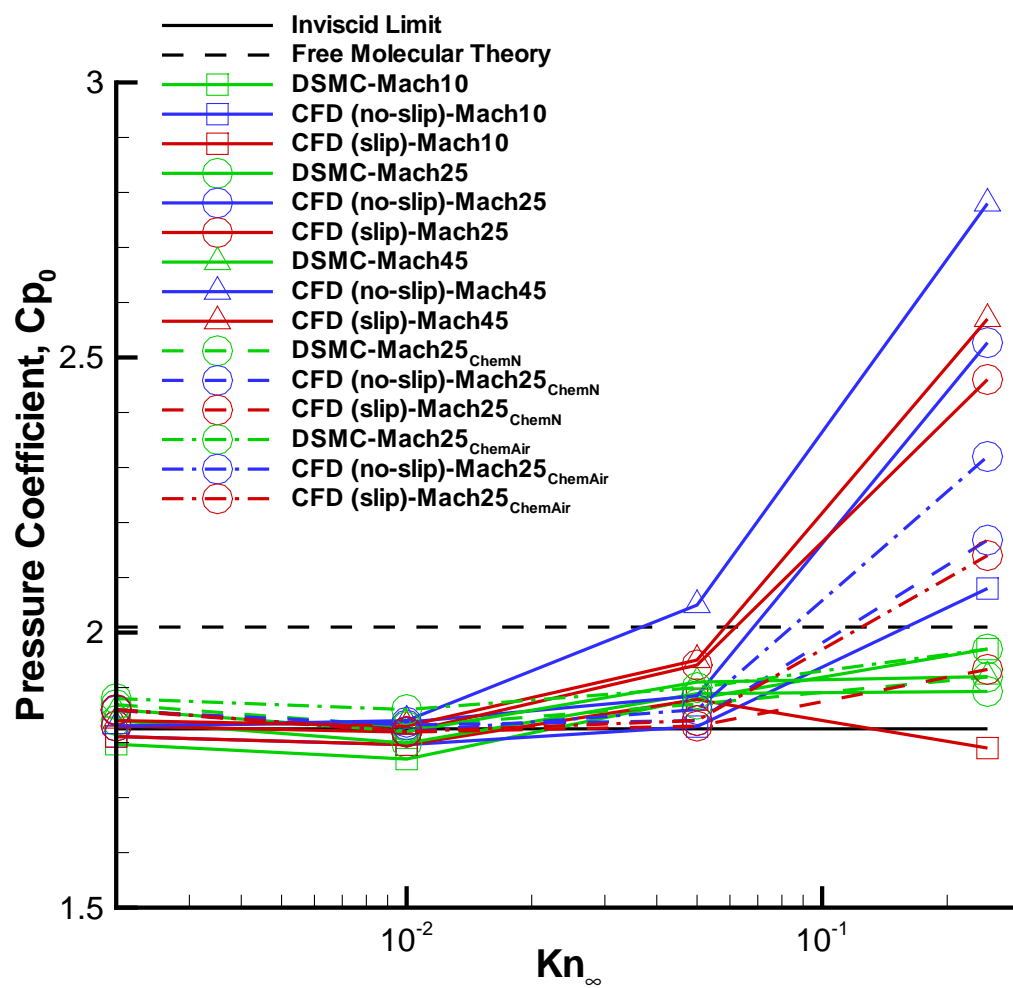
Figure 6.2: Stagnation Pressure Coefficient for DSMC and CFD with Free Molecular and Continuum Limits

conditions, will breakdown in the transitional regime. It is interesting to note that when the CFD method is past breakdown, it tends to over predict DSMC, while the CFD method with slip boundary conditions is unpredictable. Enforcing the no-slip boundary condition will always give higher gradients at the wall, hence CFD will always over predict DSMC when in continuum breakdown. However, when the slip boundary condition is utilized, the values of velocity and temperature jump at the wall are now non-zero, causing the gradient at the wall to decrease giving a better comparison to DSMC. It can be observed from this figure that the DSMC prediction of the stagnation coefficient of pressure is bounded by the limits, and is approaching the upper limit with increasing Knudsen number.

6.2.2 Stagnation Heat Rate Coefficient

As discussed earlier, the maximum heat flux and the integrated drag were utilized to compare the CFD and DSMC methods. The maximum heat flux occurs at, or near, the stagnation point. The stagnation coefficient of heat flux for each case as predicted by the CFD method, the CFD procedure with slip boundary conditions, and the DSMC technique are given in Fig. 6.3.

The stagnation heat flux coefficient as predicted by the DSMC method is given by green lines, as predicted by the CFD method is given by blue lines, and as predicted by the CFD method with slip boundary conditions is given by red lines. The solid lines represent the stagnation coefficient of heat flux in a flow of nitrogen, dashed lines represent reacting nitrogen and dash-dot lines represent reacting air. The upper limit is found to be 1 using free molecular theory, and the lower limit is found to be 0.09 using a Fay-Riddell analysis[81]. At lower Knudsen numbers, all the methods are in good agreement, and are very close to the lower limit. As the Knudsen
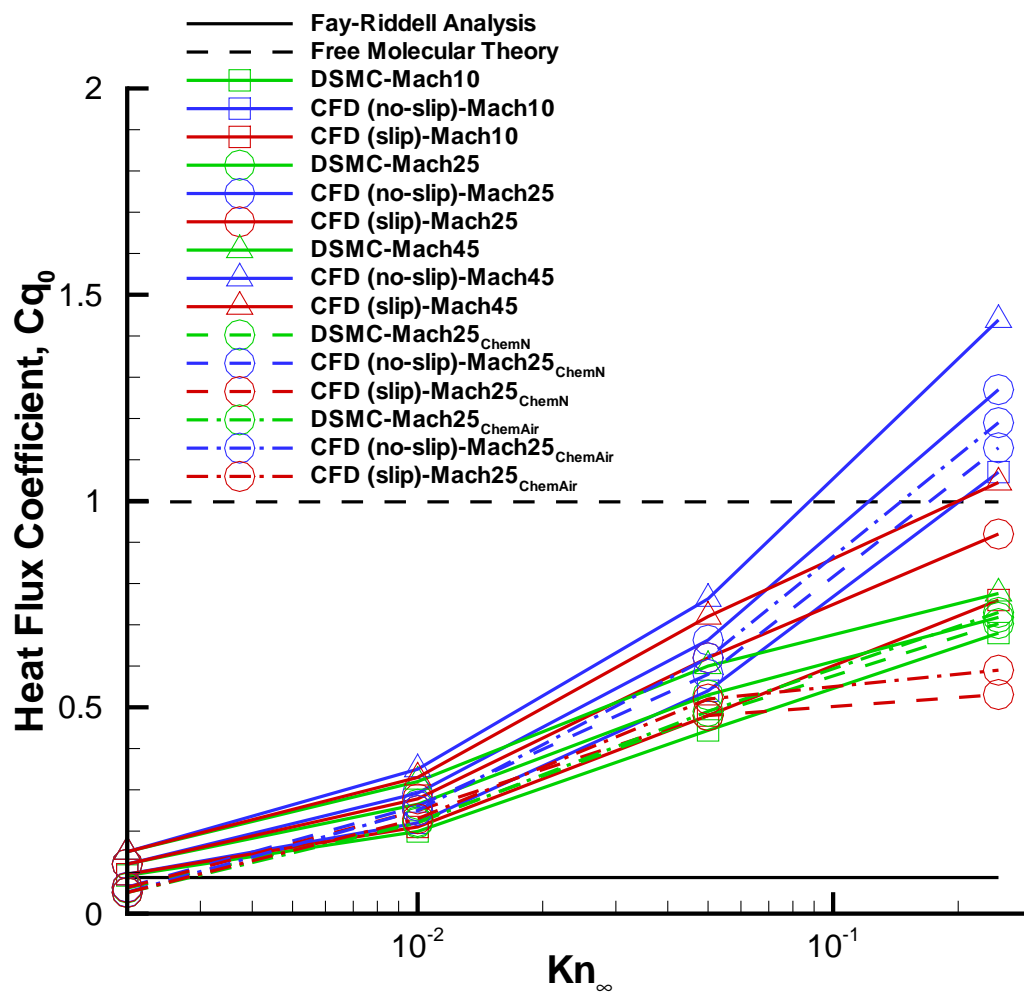
Figure 6.3: Stagnation Heat Flux Coefficient for DSMC and CFD with Free Molecular and Continuum Limits

number increases, the disparity between the values predicted by the CFD and DSMC methods widens. At Knudsen numbers larger than 0.05, the CFD method predicts stagnation heat flux coefficients to be larger than the upper limit. Implementation of slip boundary conditions in the CFD method improves the agreement with DSMC in all cases, and remains bounded by the limits even at high Knudsen numbers. However, it should be noted that the predictions from the CFD method with slip boundary conditions vary greatly from the DMSC prediction. From the figure it can be observed that the DSMC method stays bounded within the limits, and approaches the upper limit with increasing Knudsen number.

6.3   Summary

This chapter discussed the trends seen in the results by examining the stagnation pressure coefficient, the stagnation heat flux coefficient and the drag coefficient for all cases presented in this work. It was seen in all three properties that the CFD method over predicted the upper limit as Knudsen number increased. The predictions by the DSMC method were always bounded by the upper and lower limits. In general, the CFD method with velocity slip and temperature jump boundary conditions improve agreement with the DSMC method. However, it was observed that at higher Knudsen numbers the slip boundary conditions can be erratic.

It can be observed that the effects of continuum breakdown on the surface pressure are less noticeable than on the surface shear stress or surface heat flux. The reason for this is due to the fact that heat flux and shear stress are directly dependent upon gradients at the wall, while pressure is calculated from primitive variables, temperature and density, that does not require additional gradients. These gradients are always over predicted in CFD, with no-slip boundary conditions, as compared

to DSMC. However, slip boundary conditions allow velocity and temperature jump at the surface to be non-zero, decreasing the gradients at the wall. This has the effect of lowering the integrated drag and peak heating giving better comparisons to DSMC. However, the calculation of the slip boundary condition requires gradients at the surface, which in continuum breakdown are over estimated. This has the effect of generating erratic results when slip boundary conditions are utilized in the CFD method.

While slip boundary conditions can allow CFD to be run at higher Knudsen numbers it will still succumb to continuum breakdown because it only attempts to fix this problem at the surface. Continuum breakdown happens in the flow field, most notably in the shock and wake of a hypersonic object. The shear stress and heat flux are assumed to be linear functions of macroscopic flow gradients. In nonequilibrium flow, these gradients can occur over a few mean free paths making the linear assumption invalid. Mass, momentum and energy are physically carried by particles and transferred from particle to particle through collisions, which may be a completely non-linear process. This means that at higher Knudsen numbers CFD, with or without slip boundary conditions, will not be able to accurately predict the environment around the vehicle, including the surface properties. This is clearly seen in the stagnation pressure coefficient where there is good agreement between CFD and DSMC up until a Knudsen number of 0.25.

CHAPTER VII

Conclusion

7.1 Summary

The primary objective of this research was to accurately characterize the effects of continuum breakdown on surface properties of hypersonic vehicles. To be able to design a hypersonic vehicle, it is important to understand how continuum breakdown affects the surface conditions such as heat flux, pressure and shear stress. These surface conditions determine the aerodynamic and thermodynamic performance of a reentry vehicle.

This objective was addressed using continuum (CFD) and particle (DSMC) methods and starting out with simple simulations then adding complexity to determine individual effects on continuum breakdown. The work done by Lofthouse et al.[15] started this effort by characterizing breakdown over a two dimensional cylinder and wedge in flows of argon and nitrogen. The first part of this study extended this to a flow of nitrogen over a 12 inch sphere at Mach 10, 25 and 45, to be able to include a geometry that is more representative of reentry vehicles. This study also included a higher velocity where it was expected that vibrational nonequilibrium was more important than at the two lower velocities.

However, before these simulations were run, the physical models within both

the continuum and particle methods were investigated to ensure they gave similar physical solutions for the flow being simulated. For this study, it was important to assure the differences seen in the results are from the underlying assumptions of the two methods and not from the physical models being utilized. This study investigated the transport properties in both numerical methods. In this study, a VHS viscosity model with Eucken's relation was utilized for single species flows, while Gupta's mixing rule was employed for multi-species flows. Velocity slip and temperature jump boundary conditions were included in the CFD method to better compare to DSMC at higher Knudsen numbers. To better compare to DSMC, a separate rotational energy equation is included in the CFD method. This was done for two reasons; the first was to be able to simulate rotational nonequilibrium and the second was to better match the DSMC method which already employs a variable rotational energy exchange probability and therefore simulates rotational relaxation. The probability of vibrational energy exchange is modified in the DSMC method to better compare to the way the CFD technique handles vibrational relaxation. The chemistry models in both numerical techniques were investigated to ensure they agree as well as possible. A three-temperature model was introduced into the CFD method for the chemical rate calculations to be able to include the rotational temperature in the rate calculations. The preferential dissociation model was modified to not only include rotational as well as vibrational energy, but also data extracted from the DSMC method. Finally, a chemical equilibrium model was included in the DSMC method to ensure that the reverse chemical rates are calculated in the same manner as the CFD method.

In Chapter IV, a comparison of the rotational energy model in the CFD and DSMC methods was performed by comparing the temperature profiles along the

stagnation stream line for several different flow conditions. At lower Mach numbers and Knudsen numbers, it was found that the temperature profiles from DSMC and CFD agree very well. As the Mach number or Knudsen numbers were increased, the agreement diverged, but it was found this was not caused by problems with the rotational energy model. The cases showed that CFD, with a separate rotational energy, and DSMC match well, with differences appearing due to thermal nonequilibrium near the wall. A study comparing the three slip boundary condition models was conducted at Mach 10 and a Knudsen number of 0.01 in a flow of nitrogen. It was performed using DSMC and CFD to determine which slip boundary condition model best compared to the DMSC method. It was seen that all slip boundary conditions improve the agreement with DSMC, but on closer inspection the Gökçen slip boundary condition provides the best agreement with DSMC. Another study was performed on the effects of the slip boundary condition on the convergence and flow field. It was found that in all cases, slip boundary conditions improved the agreement with DSMC.

Chapter IV also discussed the effects of continuum breakdown on the surface aerothermodynamic properties (pressure, stress, heat transfer rate) of a sphere in Mach 10, 25, and 45 flows of nitrogen gas in regimes varying from continuum to a rarefied gas flow. The differences between CFD and DSMC for peak heat flux and the integrated drag increased for global Knudsen numbers increasing from 0.002 to 0.25. At low Knudsen numbers, where the flow is expected to be in the continuum regime, the aerothermodynamic properties are very similar between CFD and DSMC. It was observed that with increasing global Knudsen number, the amount of continuum breakdown increased and this had a large effect on the surface properties of the sphere. It was observed that continuum breakdown affects the surface

properties, but the effects are much less noticeable on the surface pressure than on shear stress or heat flux. The reason for this is because the heat flux and shear stress are dependent on gradients calculated at the wall, where as pressure is calculated from primitive variables, temperature and density, that does not require additional gradients. These gradients are always higher in CFD, with no-slip boundary conditions, than DSMC. However, slip boundary conditions lower the gradients at the wall giving better comparisons to DSMC. This is also the reason CFD with no-slip always over predicts peak heating and integrated drag when compared to DSMC. As Mach number was increased, the amount of continuum breakdown also increased, but there were no clear effects on the surface properties. Even though the amount of continuum breakdown increased with Mach number, the value of Kn_{GLL} remained relatively constant causing the differences in the surface properties between CFD and DSMC to be nearly unchanged. The slip boundary conditions improved the agreement between CFD and DSMC in all cases.

The last part of Chapter IV compared the results of the sphere with the analogous case of a two dimensional cylinder for a global Knudsen number of 0.01 at Mach 10. The integrated drag and peak heat flux both show that the differences between CFD and DSMC increase when run axisymmetrically. For DSMC, the amount of continuum breakdown increased for the sphere as compared to the cylinder case, however this trend was not observed in CFD. A new area Knudsen number was introduced and it was utilized to display the differences between the cylinder and sphere case.

Chapter V examined the effects of continuum breakdown on the surface aerothermodynamic properties (pressure, stress, heat transfer rate) in Mach 25 flows of reacting nitrogen and reacting air over a 12 inch diameter sphere in flow regimes from con-

tinuum to rarefied gas. This investigation added the complexity of thermo-chemical nonequilibrium. The first part of this study focused on the effects of reacting flow on continuum breakdown by comparing simulations in nitrogen with and without chemistry. For these simulations, the VHS viscosity model with Eucken's relation for thermal conductivity was replaced with Gupta's mixing rule with collision integral data. It was found that this change had several effects on the results of these simulations. It was found that this switch in the transport property model caused the integrated drag and peak heating to decrease. It was also seen that chemically reacting flow caused a decrease in the peak heating. It was also observed that the switch in the transport property model caused a decrease in the amount of continuum breakdown. However, chemical reactions were also seen to decrease the amount of continuum breakdown in the flow field.

The second part of Chapter V looked at the effects of reacting air flow on continuum breakdown and the surface properties of a sphere over a range of global Knudsen numbers varying from continuum to rarefied flow. Differences in peak heat flux and integrated drag between CFD and DSMC were observed to grow with growing global Knudsen number. When slip boundary conditions were employed in the CFD method, the agreement with DSMC improved. It was found that at higher Knudsen numbers, the effects of chemically reacting flow on continuum breakdown and the surface poperties of a hypersonic body were almost nonexistent. This is due to the diffuse nature of the gas at high Knudsen numbers, where collisions are infrequent and reactions are even more rare. It was found that at lower Knudsen numbers, the flow has a significant amount of chemistry occurring in the flow field. It is seen that the reactions occurring in the flow cause the surface heating to decrease.

Chapter VI summarized the trends seen in the results by examining the stagnation

pressure coefficient, the stagnation heat flux coefficient and the drag coefficient for all cases presented in this work. These comparisons are performed to be able to easily discern the fundamental differences seen in CFD and DSMC over the whole range of Mach and Knudsen numbers presented in this thesis. It was seen in all three properties that the CFD method over predicted the upper limit as Knudsen number increased. The reason for this is due to the fact that heat flux and shear stress are directly dependent upon gradients at the wall, while pressure is calculated from primitive variables, temperature and density, that does not require additional gradients. These gradients are always over predicted in CFD, with no-slip boundary conditions, as compared to DSMC. However, slip boundary conditions allow velocity and temperature jump at the surface to be non-zero, decreasing the gradients at the wall. This has the effect of lowering the integrated drag and peak heating giving better comparisons to DSMC. The predictions by the DSMC method were always in between the upper and lower limits. In general, the CFD method with velocity slip and temperature jump boundary conditions provided improved agreement with the DSMC method. However, it was observed that at higher Knudsen numbers the slip boundary conditions can be erratic.

7.2   Contributions

Even though there have been prior studies comparing CFD and DSMC, this study made several unique contributions to the field of hypersonic aerothermodynamics. These contributions are listed below.

1. This study was started from basic simulations and the complexity was slowly increased. Many published studies compared with experimental or flight data and therefore contain complicated thermal and chemical nonequilibrium mod-

els. This study continued the work of Lofthouse et al., and as a result did not start with the most basic simulations and instead built on previously performed work. First, the complexity of a sphere was added to consider a geometry that was more representative of real flight. This was performed to quantify the effects of running a simulation as axisymmetric, as opposed to two dimensional, on continuum breakdown and the surface properties.

2. The current work was also conducted over a wide range of flow regimes and Mach numbers, where previous studies were conducted over a limited range of these parameters. This work considered a range of flow regimes from continuum to a rarefied gas to be able to understand the effects of the degree of rarefaction on continuum breakdown and the surface properties. Unlike previous work, this study considered three Mach numbers, including Mach 45 where vibrational nonequilibrium was more important than at the lower velocities. This was performed to be able to quantify the effects of Mach number on continuum breakdown and the surface properties. No other study had compared the DSMC and CFD methods at a Mach number of 45 over a range of flow regimes from continuum to a rarefied gas.

3. A separate rotational energy equation was included into the CFD method and evaluated. The addition of a rotational energy equation into the CFD method improved the simulation of thermal nonequilibrium, which is a common phenomenon in hypersonic flows. It also helped to make truer comparisons to the DSMC method, which already employs a variable rotational energy exchange probability and therefore simulates rotational relaxation. Rotational nonequilibirum can also be important for a hybrid code where thermal nonequilibrium

can be utilized in the determination of the location of boundaries between the CFD and DSMC techniques.

4. This study evaluated the physical models in both numerical techniques to be able to ensure they give consistent physical solutions. This included modifying the transport properties, thermal relaxation, preferential dissociation and including a three-temperature model in the CFD method. The vibrational relaxation model was modified and a chemical equilibrium model was included in the DSMC technique.

5. Finally, this study added the complexity of gas mixtures and reacting flow to be able to study the effects these processes had on continuum breakdown and the surface properties. This study was conducted over a wide range of flow regimes, which has never been done before for comparisons between the CFD and DSMC methods with reacting flow. This was performed for both reacting nitrogen and reacting air in a Mach 25 flow. The addition of gas mixtures and reacting flow makes these simulations more representative of real hypersonic flows.

7.3   Future Work

While this thesis represents a detailed study of the effects of continuum breakdown on hypersonic vehicles, there are additional areas where this work can be expanded.

7.3.1   Comparison to Flight/Experiential Data

The first additional area of research is to compare the CFD and DSMC methods to experimental or flight data. This thesis has been a purely numerical study, which was appropriate for deriving basic comparisons between the CFD and DSMC methods.

However, this research has progressed to the point where enough physical models have been included to simulate more complicated situations.

In order to make these comparisons, it is likely to require three dimensional simulations. While this allows for a greater range of experimental and flight data it will also allow the comparison of two dimensional, three dimensional and axisymmetric simulations. This will establish if the area based Knudsen number is more accurate in determining breakdown than the traditional Knudsen number.

This is not just an opportunity to verify the axisymmetric model, it is also an opportunity to verify the physical models in both numerical methods. Up until now, the current work has been a numerical study comparing the CFD and DSMC methods, and not comparing to experimental or flight data. So, there was no way to confirm the physical models implemented in both numerical techniques are physically correct. This study strived to make sure the physical models in both numerical methods compared well to each other, not if they compared well to real physical results.

7.3.2 Ionization

The current research included the effects of chemical reactions in a Mach 25 flow of nitrogen and air over a range of flow regimes. An additional area of research is to consider higher Mach numbers in reacting flow over regimes from continuum to a rarefied gas. At higher Mach numbers, the effects of chemical nonequilibrium are expected to be greater. In addition, at higher velocities the flow should also undergo ionization as well as dissociation. Additional work might consider Mach numbers similar to the Stardust reentry vehicle[9]. Extending to higher Mach numbers requires additional research into the forward and backward reaction rates for

ionization in both numerical techniques, to ensure they are as equivalent as possible. This extension would allow further analysis of the effects of chemical nonequilibrium on continuum breakdown and the surface properties.

7.3.3 Thermal Relaxation

The current research investigated the rotational and vibrational relaxation models in the DSMC and CFD techniques. It was found there was good agreement between the two methods except when the flow was chemically reacting. The current work found that the vibrational relaxation was slower than the chemical reaction rates leading to vibrational nonequilibrium in the DSMC method. This phenomenon did not occur in the CFD method, leading to a disparity in the reaction rates between the two methods. One possible solution for this issue is to have vibration-vibration relaxation between different molecules[84]. Including vibration-vibration energy exchange possibly allows for a quicker, more physical, vibrational relaxation, thus allowing the two numerical techniques to simulate similar reaction rates.

Since the DMSC method is a particle technique, where each particle is a given species with a different energy, implementing a vibration-vibration energy exchange is possible. In the CFD method, since there is only one vibrational energy equation, each species has the same vibrational energy. In order to implement vibration-vibration energy exchange, the CFD method would first have to be modified to use a vibrational energy equation for each species. This would allow for vibration-vibration energy exchange between molecules and make it easier to calculate the vibrational temperature, which currently requires an iterative method to calculate. It is also suggested that a separate rotational energy equation for every species be implemented in the CFD method as well. Separate rotational and vibrational temperatures in the

CFD method will make better comparisons to the DSMC technique, which already is separated by species.

7.3.4 Surface Characteristics

The current research focused on the effects of continuum breakdown on the surface properties of a hypersonic vehicle. The current work did not investigate the surface characteristics, such as the accommodation coefficients and catalytic wall conditions. The first area of research with regard to the surface that can be expanded upon is to extend the velocity slip and temperature jump to be utilized with three dimensional simulations; currently they only work for two dimensional and axisymmetric simulations. An investigation of the accommodation coefficients in the slip model is suggested. The current work employs accommodation coefficients of unity for a fully diffuse wall. There has been research conducted on the surface accommodation coefficient on flat plates by Lofthouse et al.[14]. Additional work on the flows about different bodies, such as a sphere, utilizing different accommodation coefficients is recommended.

Since the current work has included chemical reactions, a further area of research is to investigate the surface catalysis models. For this work, a non-catalytic wall is assumed. Further research in to both numerical methods is suggested if comparisons to experimental or flight data is desired.

APPENDIX

APPENDIX A

Data Sets

A.1 Rotational Nonequilibrium

Table A.1 gives Z_{rs}^∞ and T^*, which are constant, for a given species, that are utilized to calculate the rotational collision number, Z_{rs}, as derived by Parker[62].

Table A.1: Rotational nonequilibrium constants

Species	Z_{RS}^∞	T_S^* [K]
N_2	18.1	91.5
O_2	14.4	90.0
H_2	350.0	0.0
Cl_2	47.1	300.0
NO	5.0	117.0
CO	11.4	92.0
OH	15.7	80.0
N_2^+	18.1	91.5
O_2^+	14.4	90.0
NO^+	5.0	117.0
CO_2	15.0	195.0
NO_2	15.7	80.0
H_2O	15.7	80.0

A.2 Three Temperature Model for Chemistry in CFD

Table A.2 gives the exponents utilized in the three temperature model in the CFD method to calculate the reaction rates. The table gives the type of reaction along with the values for the exponents.

Table A.2: Temperature Powers

	a	b	c
Forward	0.3	0.2	0.5
Backward	1.0	0.0	0.0
Exchange	1.0	0.0	0.0
Ionization	0.0	0.0	1.0

A.3 Chemistry Rate Constants

Table A.3 gives the forward reaction rate coefficients utilized in the CFD and DSMC methods for this study.

Table A.3: Reaction rates employed in DSMC and CFD

Reaction	a $[m^3/molecule/s]$	η	ε/k_{BOLTZ} [K]
Dissociation			
$N_2 + M \rightleftharpoons N + N + M \ (M = N_2, O_2, NO)$	1.162×10^{-8}	-1.6	113,200
$N_2 + M \rightleftharpoons N + N + M \ (M = N, O)$	4.980×10^{-8}	-1.6	113,200
$O_2 + M \rightleftharpoons O + O + M \ (M = N_2, O_2, NO)$	3.321×10^{-9}	-1.5	59,400
$O_2 + M \rightleftharpoons O + O + M \ (M = N, O)$	1.660×10^{-8}	-1.5	59,400
$NO + M \rightleftharpoons N + O + M \ (M = N_2, O_2, NO)$	8.302×10^{-15}	0.0	75,500
$NO + M \rightleftharpoons N + O + M \ (M = N, O)$	1.826×10^{-13}	0.0	75,500
Exchange			
$NO + O \rightleftharpoons O_2 + N$	1.395×10^{-17}	0.0	19,450
$N_2 + O \rightleftharpoons NO + N$	1.063×10^{-12}	-1.0	38,400

A.4 Variable Hard Sphere Temperature Exponent

Table A.4 gives the VHS ω values calculated using the viscosity collision integral. A linear regression is performed on the log of the viscosity collision integral verses log of the temperature to calculate the VHS ω values.

Table A.4: Variable Hard Sphere Temperature Exponents

	N_2	O_2	NO	N	O
N_2	0.68	0.69	0.72	0.72	0.69
O_2	0.69	0.68	0.69	0.73	0.74
NO	0.72	0.69	0.70	0.76	0.73
N	0.72	0.73	0.76	0.74	0.74
O	0.69	0.74	0.73	0.74	0.77

BIBLIOGRAPHY

BIBLIOGRAPHY

[1] Wagner, W., "A Convergence Proof of Bird's Direct Simulation Monte Carlo Method for the Boltzmann Equation," *Journal of Statistical Physics*, Vol. 66, No. 3/4, 1992, pp. 1011–1044.

[2] Vincenti, W. G. and Kruger, C. H., *Introduction to Physical Gas Dynamics*, Krieger Publishing Company, 1965.

[3] Bird, G. A., *Molecular Gas Dynamics and the Direct Simulation of Gas Flows*, Oxford University Press, 1994.

[4] Schwartzentruber, T. E., *A Modular Particle-Continuum Numerical Algorithm for Hypersonic Non-Equilibrium Flows*, Ph.D. thesis, University of Michigan, Ann Arbor, Michigan, 2007.

[5] Moss, J. N. and Bird, G. A., "Direct Simulation of Transitional Flow for Hypersonic Reentry Conditions," *Journal of Spacecraft and Rockets*, Vol. 40, No. 5, 2003, pp. 830–843, Reprinted from AIAA Paper 85-0223.

[6] Lumpkin, F. E., Boyd, I. D., and Venkatapathy, E., "Comparison of Continuum and Particle Simulations of Expanding Rarefied Flows," *American Institute of Aeronautics and Astronautics*, 1993, AIAA-1993-0728, 31st AIAA ASM Conference, Reno, NV, January 11-14.

[7] Moss, J. N., Mitcheltree, R. A., Wilmoth, R. G., and Dogra, V. K., "Direct Simulations Monte Carlo Navier-Stokes of Blunt Body Wake Flows," *American Institute of Aeronautics and Astronautics*, Vol. 32, No. 7, 1994, pp. 1399–1406.

[8] Olynick, D. R., Taylor, J. C., and Hassan, H. A., "Comparisons between Monte Carlo Methods and Navier-Stokes Equations for Re-Entry Flows," *Journal of Thermophysics and Heat Transfer*, Vol. 8, No. 2, 1994, pp. 251–258.

[9] Boyd, I. D., Trumble, K., and Wright, M. J., "Nonequilibrium Particle and Continuum Analysis of Stardust Entry Near-Continuum Conditions," *American Institute of Aeronautics and Astronautics*, 2007, AIAA-2007-4543, 39th AIAA Thermophysics Conference, Miami, Florida, June 25-28.

[10] Lofthouse, A. J., Boyd, I. D., and Wright, M. J., "Effects of Continuum Breakdown on Hypersonic Aerothermodynamics," *Physics of Fluids*, Vol. 19, 2007, Article 027105.

[11] Lofthouse, A. J., Scalabrin, L. C., and Boyd, I. D., "Velocity Slip and Temperature Jump in Hypersonic Aerothermodynamics," *Journal of Thermophysics and Heat Transfer*, Vol. 22, No. 1, 2008, pp. 38–48.

[12] Lofthouse, A. J., Scalabrin, L. C., and Boyd, I. D., "Hypersonic Aerothermodynamics Analysis Across Nonequilibrium Regimes Using Continuum and Particle Methods," *American Institute of Aeronautics and Astronautics*, 2007, AIAA-2007-3903, 39th AIAA Thermophysics Conference, Miami, Florida, June 25-28.

[13] Lofthouse, A. J. and Boyd, I. D., "Nonequilibrium Aerothermodynamics of Sharp Leading Edges," *American Institute of Aeronautics and Astronautics*, 2009, AIAA-2009-1316, 47th AIAA ASM Conference, Orlando, FL, Jan. 5-8.

[14] Lofthouse, A. J. and Boyd, I. D., "Hypersonic Flow over a Flat Plate: CFD Comparison with Experiment," *American Institute of Aeronautics and Astronautics*, 2009, AIAA-2009-1315, 47th AIAA ASM Conference, Orlando, FL, Jan. 5-8.

[15] Lofthouse, A. J., *Nonequilibrium Hypersonic Aerothermodynamics using the Direct Simulation Monte Carlo and Navier-Stokes Models*, Ph.D. thesis, University of Michigan, Ann Arbor, Michigan, 2008.

[16] Agarwal, R. K., Chen, R., and Cheremisin, F. G., "Computation of Hypersonic Shock Wave Flows of Diatomic Gases Using the Generalized Boltzmann Equation," *American Institute of Aeronautics and Astronautics*, 2007, AIAA-2007-4541, 39th AIAA Thermophysics Conference, Miami, FL, June 25-28.

[17] Chen, R., Agarwal, R. K., and Cheremisin, F. G., "Computation of Hypersonic Flow of a Diatomic Gas in Rotational Nonequilibrium Past a Blunt Body Using the Generalized Boltzmann Equation," *American Institute of Aeronautics and Astronautics*, 2007, AIAA-2007-4550, 39th AIAA Thermophysics Conference, Miami, FL, June 25-28.

[18] Bhatnagar, P. L., Gross, E. P., and Krook, M., "A Model for Collision Processes in Gases," *Physical Review*, Vol. 94, No. 3, 1954, pp. 511–525.

[19] Holway, L. H., "Kinetic Theory of Shock Structure Using an Ellipsoidal Distribution Function," *Proceedings of the Fourth International Symposium on Rarefied Gas Dynamics*, 1966, pp. 193–215, AIP Conference Proceedings.

[20] Chou, S. Y. and Baganoff, D., "Kinetic Flux-Vector Splitting for the Navier-Stokes Equations," *Journal of Computational Physics*, Vol. 130, 1997, pp. 217–230.

[21] Burnett, D., "The Distribution of Molecular Velocities and the Mean Motion in a Non-Uniform Gas," *Proc. London Math Soc.*, 1934.

[22] Garcia, A. L. and Alder, B. J., "Generation of the Chapman-Enskog Distribution," *Journal of Computational Physics*, Vol. 140, 1998, pp. 66–70.

[23] Claycomb, A. E. and Greendyke, R. B., "Extending CFD Modeling to the Transition regime by Enhanced Thermophysics Modeling," *American Institute of Aeronautics and Astronautics*, 2008, AIAA-2008-3930, 40th AIAA Thermophysics Conference, Seatle, WA, June 23-26.

[24] Guo, K. L. and Liaw, G. S., "Numerical Predictions of the Transitional Flow over an Elliptical Cylinder by the Burnett Equations and the DSMC Method," *American Institute of Aeronautics and Astronautics*, 1999, AIAA-1999-3457, 33rd Thermophysics Conference, Norfolk, VA, June 28- July 1.

[25] Comeaux, K. A., Chapman, D. R., and MacCormack, R. W., "An Analysis of the Burnett Equations Based on the Second Law of Thermodynamics," *American Institute of Aeronautics and Astronautics*, 1995, AIAA-1995-0415, 33rd AIAA ASM Conference, Reno, NV, January 9-12.

[26] Gombosi, T. I., *Gaskinetic Theory*, Cambridge University Press, 1994.

[27] Larsen, P. S. and Borgnakke, C., "Statistical Collision Model for Monte Carlo Simulation of Polyatomic Gas MIxture," *Journal of Computational Physics*, Vol. 18, 1975, pp. 405–420.

[28] Burt, J. M., Deschenes, T. . R., Boyd, I. D., and Josyula, E., "Evaluation of a Hybrid Boltzmann Continuum Method for High Speed Nonequilibrium Flows," *American Institute of Aeronautics and Astronautics*, 2010, AIAA-2010-1569, 48th AIAA ASM Conference, Orlando, FL, January 4-7.

[29] Gallis, M. A. and Torczynski, J. R., "The Application of the BGK Model in Particle Simulations," *American Institute of Aeronautics and Astronautics*, 2000, AIAA-2000-2360, 34th AIAA Thermophysics Conference, Denver, CO, June 19-22.

[30] Macrossan, M. N., "A Particle Simulation Method for the BGK Equation," *American Institute of Physics*, 2001, Rarefied Gas Dynamics: 22nd International Symposium.

[31] Burt, J. M., *Monte Carlo Simulation of Solid Rocket Exhaust Plumes at High Altitude*, Ph.D. thesis, University of Michigan, Ann Arbor, Michigan, 2006.

[32] Hirsch, C., *Numerical Computation of Internal and External Flows*, John Wiley and Sons, 2007.

[33] Scalabrin, L. C., *Numerical Simulation of Weakly Ionized Hypersonic Flow over Reentry Capsules*, Ph.D. thesis, University of Michigan, Ann Arbor, Michigan, 2007.

[34] Kolobov, V. I., Bayyuk, S. A., Arslanbekov, R. R., Aristov, V. V., Frolova, A. A., and Zabelok, S. A., "Construction of a Unified Continuum/Kinetic Solver for Aerodynamic Problems," *Journal of Space Craft and Rockets*, Vol. 42, No. 2, 2005, pp. 598–606.

[35] Tallec, P. L. and Mallinger, F., "Coupling Boltzmann and Navier-Stokes Equations by Heat Fluxes," *Journal of Computational Physics*, Vol. 136, 1997, pp. 51–67.

[36] Bird, G. A., "Breakdown of Translational and Rotational Equilibrium in Gaseous Expansions," *AIAA Journal*, Vol. 8, No. 2, 1970, pp. 1998–2003.

[37] Boyd, I. D., Chen, G., and Candler, G., "Predicting Failure of the Continuum Fluid Equations in Transitional Hypersonic Flows," *Physics of Fluids*, Vol. 7, 1995, pp. 210–219.

[38] Camberos, J. A., Schrock, C. R., McMullan, R. J., and Branam, R. D., "Development of Continuum Onset Criteria with Direct Simulation Monte-Carlo using Boltzmann's H-Theorem: Review and Vision," *American Institute of Aeronautics and Astronautics*, 2006, AIAA-2006-2942, 9th AIAA/ASME Joint Thermophysics and Heat Transfer Conference, San Francisco, CA, June 5-8.

[39] Tiwari, S., "Coupling of the Boltzmann and Euler Equations with Automatic Domain Decomposition," *Journal of Computational Physics*, Vol. 144, 1998, pp. 710–726.

[40] Garcia, A. L., Bell, J. B., Crutchfield, W. Y., and Alder, B. J., "Adaptive Mesh and Algorithm Refinement using Direct Simulation Monte Carlo," *Journal of Computational Physics*, Vol. 154, 1999, pp. 134–155.

[41] Dietrich, S. and Boyd, I. D., "Scalar and Parallel Optimized Implementation of the Direct Simulation Monte Carlo Method," *Journal of Computational Physics*, Vol. 126, 1996, pp. 328–342.

[42] Vijayakumar, P., Sun, Q., and Boyd, I. D., "Vibrational-Translational Energy Exchange Models for the Direct Simulation Monte Carlo Method," *Physics of Fluids*, Vol. 11, No. 8, 1999, pp. 2117–2126.

[43] Boyd, I. D., "Rotational-Translational Energy Transfer in Rarefied Nonequilibrium Flows," *Physics of Fluids A*, Vol. 2, No. 3, 1991, pp. 447–452.

[44] Scalabrin, L. C. and Boyd, I. D., "Development of an Unstructured Navier-Stokes Solver for Hypersonic Nonequilibrium Aerothermodynamics," *American Institute of Aeronautics and Astronautics*, 2005, AIAA 2005-5203, 38th AIAA Thermophysics Conference, Toronto, Canada, June.

[45] Scalabrin, L. C. and Boyd, I. D., "Numerical Simulation of Weakly Ionized Hypersonic Flow for Reentry Configurations," *American Institute of Aeronautics and Astronautics*, 2006, AIAA 2006-3773, 9th AIAA/ASME Joint Thermophysics and Heat Transfer Conference, San Francisco, CA, June.

[46] Steger, J. L. and Warming, R. F., "Flux Vector Splitting of the Inviscid Gasdynamic Equations with Application to Finite-Difference Methods," *Journal of Computational Physics*, Vol. 40, 1981, pp. 263–293.

[47] Kannenberg, K. C. and Boyd, I. D., "Strategies for Efficient Particle Resolution in the Direct Simulation Monte Carlo Method," *Journal of Computational Physics*, Vol. 157, 2000, pp. 727–745.

[48] Wilke, C. R., "A Viscosity Equation for Gas Mixtures," *Journal of Chemical Physics*, Vol. 18, No. 4, 1950, pp. 517–519.

[49] Gupta, R. N., Yos, J. M., Thompson, R. A., and Lee, K., "A Review of Reaction Rates and Thermodynamic and Transport Properties for an 11-species Air Model for Chemical and Thermal Nonequilibrium Calculations to 30,000 K," Technical Report 1232, NASA, 1990.

[50] Palmer, G. E. and Wright, M. J., "Comparison of Methods to Compute High-Temperature Gas Thermal Conductivity," *American Institute of Aeronautics and Astronautics*, 2003, AIAA-2003-3913, 36th AIAA Thermophysics Conference, Orlando, FL, June 23-26.

[51] Schwartzentruber, T. E., Scalabrin, L. C., and Boyd, I. D., "Hybrid Particle-Continuum Simulations of Non-Equilibrium Hypersonic Blunt Body Flow Fields," *American Institute of Aeronautics and Astronautics*, 2006, AIAA 2006-3602, 9th AIAA/ASME Joint Thermophysics and Heat Transfer Conference, San Francisco, CA, June.

[52] Gosse, R. and Candler, G., "Diffusion Flux Modeling: Applications to Direct Entry Problems," *American Institute of Aeronautics and Astronautics*, 2005, AIAA-2005-389, 43rd AIAA Aerospace Sciences Meeting and Exhibit, Reno, Nevada, Jan. 10-13.

[53] Palmer, G. E. and Wright, M. J., "Comparison of Methods to Compute High-Temperature Gas Viscosity," *Journal of Thermophysics and Heat Transfer*, Vol. 17, No. 2, 2003, pp. 232–239.

[54] Wright, M. J., Bose, D., Palmer, G. E., and Levin, E., "Recommended Collision Integrals for Transport Property Computations, Part 1: Air Species," *AIAA Journal*, Vol. 43, No. 12, 2005, pp. 2258–2564.

[55] Lockerby, D. A. and Reese, J. M., "Velocity Boundary Condition at Solid Walls in Rarefied Gas Calculations," *Physical Review E*, Vol. 70, 2004.

[56] Gökçen, T., MacCormack, R. W., and Chapman, D. R., "Computational Fluid Dynamics Near the Continuum Limit," *American Institute of Aeronautics and Astronautics*, 1987, AIAA 1987-1115.

[57] Gökçen, T. and MacCormack, R. W., "Nonequilibrium effects for hypersonic transitional flows using continuum approach," *American Institute of Aeronautics and Astronautics*, 1989, AIAA 1989-0461, 27th AIAA ASM Conference, Reno, NV, January.

[58] O'Hare, L., Lockerby, D. A., Reese, J. M., and Emerson, D. R., "Near-Wall Effects in Rarefied Gas Micro-Flows: some Modern Hydrodynamic Approaches," *International Journal of Heat and Fluid Flow*, Vol. 28, 2007, pp. 37–43.

[59] Lockerby, D. A., Reese, J. M., and Gallis, M. A., "Capturing the Knudsen Layer in Continuum-Fluid Models of Nonequilibrium Gas Flows," *AIAA Journal*, Vol. 43, No. 6, 2005.

[60] Gupta, R. N., Scott, C. D., and Moss, J. N., "Slip-Boundary Equations for Multicomponent Nonequilibrium Airflow," Technical Report 2452, NASA, 1985.

[61] Boyd, I. D., "Analysis of Rotational Nonequilibrium in Standing Shock Waves of Nitrogen," *AIAA Journal*, Vol. 28, 1990, pp. 1997–1999.

[62] Parker, J. G., "Rotational and Vibrational Relaxation in Diatomic Gases," *Physics of Fluids*, Vol. 2, 1959, pp. 449–462.

[63] Boyd, I. D., "Analysis of Vibrational-Translational Energy Transfer using the Direct Simulation Monte Carlo Method," *Physics of Fluids A*, Vol. 3, No. 7, 1991, pp. 1785–1791.

[64] Millikan, R. C. and White, D. R., "Systematics of Vibrational Relaxation," *Journal of Chemistry Physics*, Vol. 39, 1963, pp. 3209–3213.

[65] Park, C., "Review of Chemical-Kinetic Problems of Future NASA Missions, I: Earth Entries," *Journal of Thermophysics and Heat Transfer*, Vol. 7, No. 3, 1993.

[66] Park, C., *Nonequilibrium Hypersonic Aerothermodynamics*, John Wiley and Sons, 1990.

[67] Lumpkin, F. E., Haas, B. L., and Boyd, I. D., "Resolutions of Differences Between Collision Number Definitions in Particle and Continuum Simulations," *Physics of Fluids A*, Vol. 3, No. 9, 1991.

[68] Farbar, E., "Testing the vibrational relaxation model in MONACO," *Unpublished Report, Department of Aerospace Engineering, University of Michigan*, March 2007.

[69] Holman, T. D. and Boyd, I. D., "Numerical Investigation of the Effects of Continuum Breakdown on Hypersonic Vehicle Surface Properties," *American Institute of Aeronautics and Astronautics*, 2008, AIAA-2008-3928, 40th AIAA Thermophysics Conference, Seattle, Washington, June 23-26.

[70] Deschenes, T. R., Holman, T. D., Boyd, I. D., and Schwartzentruber, T. E., "Analysis of Internal Energy Transfer within a Modular Particle-Continuum Method," *American Institute of Aeronautics and Astronautics*, 2009, AIAA-2009-1213, 47th AIAA ASM Conference, Orlando, Florida, January 5-8.

[71] Gimelshein, N. E., Gimelshein, S. F., and Levin, D. A., "Vibrational Relaxation Rates in the Direct Simulation Monte Carlo Method," *Physics of Fluids*, Vol. 14, No. 12, 2002.

[72] Boyd, I. D., "Modeling Backward Chemical Rate Processes in the Direct Simulation Monte Carlo Method," *Physics of Fluids*, Vol. 19, 2007.

[73] Haas, B. L. and Boyd, I. D., "Models for Direct Monte Carlo Simulation of Coupled Vibration-Dissociation," *Physics of Fluids A*, Vol. 5, No. 2, 1993.

[74] Boyd, I. D. and Gokcen, T., "Computation of Axisymmetric and Ionized Flows using Particle and Continuum Methods," *AIAA Journal*, Vol. 32, 1994, pp. 1828.

[75] Park, C., "The Limits of Two-Temperature Model," *American Institute of Aeronautics and Astronautics*, 2010, AIAA-2010-911, 48th AIAA ASM, Orlando, FL, January 4-7.

[76] Park, C., "A review of Reaction Rates in High Temperature Air," *American Institute of Aeronautics and Astronautics*, 1989, AIAA-1989-1740, 24th AIAA Thermophysics Conference, Buffalo, NY, June 12-14.

[77] Park, C., "Review of Chemical-Kinetic Problems of Future NASA Missions, II: Mars Entries," *Journal of Thermophysics and Heat Transfer*, Vol. 8, No. 1, 1994.

[78] Hash, D., Olejniczak, J., Wright, M., Prabhu, D., Pulsonetti, M., Hollis, B., Gnoffo, P., Barnhardt, M., Nompelis, I., and Candler, G., "FIRE II Calculations for Hypersonic Nonequilibrium Aerothermodynamics Code Verification: DPLR, LAURA, and US3D," *American Institute of Aeronautics and Astronautics*, 2007, AIAA-2007-605, 45th AIAA ASM Conference, Reno, Nevada, January 8-11.

[79] Farbar, E. D. and Boyd, I. D., "Simulation of FIRE II Reentry Flow Using the Direct Simulation Monte Carlo Method," *American Institute of Aeronautics and Astronautics*, 2008, AIAA-2008-4103, 40th AIAA Thermophysics Conference, Seattle, Washington, June 23-26.

[80] Silverman, B. W., *Density Estimation for Statistics and Data Analysis*, Chapman and Hall, 1986, pg 10.

[81] Bertin, J. J., *Hypersonic Aerothermodynamics*, American Institute of Aeronautics and Astronautics, 1994.

[82] Anderson, J. D., *Modern Compressible Flow with historical perspectives*, McGraw-Hill, thirid ed., 2003.

[83] Bailey, A. B. and Hiatt, J., "Free-Flight Measurements of Sphere Drag at Subsonic, Transonic, Supersonic, and Hypersonic Speeds for Continuum, Transition, and Near-Free-Molecular Flow Conditions," Technical Report 291, AEDC, 1970.

[84] Bonder, Y. A., Gimelshein, S. F., and Ivanov, M. S., "DSMC Modeling of Vibration-Vibration Energy Transfer Between Diatomic Molecules," *American Institute of Physics*, 2009, Rarefied Gas Dynamics: 26th International Symposium.

ABSTRACT

NUMERICAL INVESTIGATION OF THE EFFECTS OF CONTINUUM

BREAKDOWN ON HYPERSONIC VEHICLE SURFACE PROPERTIES

by

Timothy Dean Holman

Chairperson: Iain D. Boyd

A hypersonic vehicle crosses many regimes, from rarefied to continuum, as the vehicle descends through the atmosphere. This variation makes it difficult to simulate the flow since the physical accuracy of computational fluid dynamics (CFD) can breakdown in rarefied flows and the direct simulation Monte Carlo (DSMC) method is computationally expensive in continuum flows.

This dissertation investigates the effects of continuum breakdown on the surface aerothermodynamic properties of a hypersonic vehicle. The study begins by investigating a sphere in Mach 10, 25, and 45 flow of non-reacting nitrogen gas. The consideration of nitrogen gas allows the study of the effects of thermal nonequilibrium. The next portion of the study investigates a sphere in Mach 25 reacting flows of both nitrogen and air. This adds multi-species flow to the simulation and per-

mits for reacting flow, which allows the study of the effects of thermal and chemical nonequilibrium.

A separate rotational energy equation is employed in the CFD method to be able to simulate rotational nonequilibrium. Since CFD is numerically more efficient than DSMC, slip boundary conditions are included into the CFD method to extend the range where CFD can be accurately utilized. An investigation of other physical models in both numerical methods is conducted to ensure they are equivalent.

In a flow of nitrogen, as the global Knudsen number is increased from continuum flow to a rarefied gas, the amount of continuum breakdown seen in the flow and on the surface increases. This causes an increase in the differences between CFD and DSMC. As the Mach number increases, the amount of continuum breakdown observed increases. However, the difference between CFD and DSMC remains relatively constant. The differences in the surface properties between CFD and DSMC increase when the simulation is run axisymmetrically in comparison to two-dimensional. It is also seen that chemically reacting flow causes the integrated drag to increase, while it decreases the peak heating. Reacting flow is also seen to decrease the amount of continuum breakdown in the flow field.